11-2020

APPLICATIONS OF LAND SURFACE TEMPERATURE FROM SATELLITE REMOTE SENSING OVER THE UNITED ARAB EMIRATES (UAE)

Abduldaem Saeed Farea Qasem Alqasemi

United Arab Emirates University

College of Humanities and Social Sciences

APPLICATIONS OF LAND SURFACE TEMPERATURE FROM
SATELLITE REMOTE SENSING OVER THE UNITED ARAB
EMIRATES (UAE)

Abduldaem Saeed Farea Qasem Alqasemi

This dissertation is submitted in partial fulfilment of the requirements for the degree
of Doctor of Philosophy

Under the Supervision of Dr. Abdelgadir Abuelgasim

November 2020

Declaration of Original Work

I, Abduldaem Saeed Farea Qasem Alqasemi , the undersigned, a graduate student at the United Arab Emirates University (UAEU), and the author of this dissertation entitled "*Applications of Land Surface Temperature from Satellite Remote Sensing Over the United Arab Emirates (UAE)*", hereby, solemnly declare that this dissertation is my own original research work that has been done and prepared by me under the supervision of Dr. Abdelgadir Abuelgasim in the College of Humanities and Social Sciences at UAEU. This work has not previously formed the basis for the award of any academic degree, diploma or a similar title at this or any other university. Any materials borrowed from other sources (whether published or unpublished) and relied upon or included in my dissertation have been properly cited and acknowledged in accordance with appropriate academic conventions. I further declare that there is no potential conflict of interest with respect to the research, data collection, authorship, presentation and/or publication of this dissertation.

Student's Signature: _____   Date: 15-10-2020

Advisory Committee

1) Advisor: Abdelgadir Abuelgasim

Title: Associate Professor

Department of Geography and Urban Sustainability

College of Humanities and Social Science

2) Co-advisor: Hakim Saibi

Title: Associate Professor

Department of Geology

College of Science

3) Member: Ala Adin Aldahan

Title: Professor

Department of Geology

College of Science

4) Member (External): Ayad Mohammed Fadhil Al-Quraishi

Title: Professor

Department of Surveying and Geomatics Engineering

Tishk International University, Iraq

5) Member (External): Mohamed El-Desoky Hereher

Title: Professor

Department of Geography

Sultan Qaboos University, Oman

Approval of the Doctorate Dissertation

This Doctorate Dissertation is approved by the following Examining Committee Members:

1) Advisor (Committee Chair): Abdelgadir Abuelgasim

   Title: Associate Professor

   Department of Geography and Urban Sustainability

   College of Humanities and Social Science

   Signature _____ Date __11/11/2020__

2) Member: Khaula Alkaabi

   Title: Assistant Professor

   Department of Geography and Urban Sustainability

   College of Humanities and Social Science

   Signature _____ Date __11/11/2020__

3) Member: Hasan Arman

   Title: Professor

   Department of Geology

   College of Science
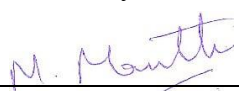
   Signature _____ Date __11/11/2020__

4) Member (External Examiner): Prashanth Reddy Marpu

   Title: Associate Professor

   Department of Electrical and Computer Engineering

   Institution: Khalifa University of Science and Technology, UAE

   Signature _____ Date __11/11/2020__

This Doctorate Dissertation is accepted by:

Dean of the College of Humanities and Social Science: Professor Hassan Alnaboodah

Signature _____   Date ___25/01/2021_____

Dean of the College of Graduate Studies: Professor Ali Al-Marzouqi

Signature ____Ali Hassan_____   Date ___25/01/2021_____

Copy ____ of ____

Abstract

In cities worldwide, increasing urbanization causes major land use and land cover changes on the surface of the Earth. It has been identified as being one of the most important anthropogenic effects on the climate. As a result, rapid population growth and the rise in industrialization in the United Arab Emirates (UAE) may have created substantial environmental stress and consequence for life quality. Remote sensing-based Land Surface Temperature (LST) is significantly essential for different studies. Satellite images obtained by the Moderate Resolution Imaging Spectroradiometer (MODIS) are used to retrieve LST. This research consists of introduction and five components of some MODIS LST application over the UAE: (1) detect the thermal anomaly for groundwater flow after rainy day; (2) investigate the relationship between soil salinity and LST; (3) estimate the air temperature; (4) study the night Surface Urban Heat Island (SUHI); (5) detect the effect of the lockdown of COVID-19 on air pollutants and SUHI. The results demonstrate that the thermal anomaly was identified following a rainy day, which can be utilized to predict the optimal groundwater resources. The salinity of the soil showed a high correlation with MODIS LST at night. In addition, the air temperature estimation study indicated the significance of the MODIS LST as a credible proxy for air temperature. As regards the SUHI over the city of Dubai, it has risen gradually with the growth of the city. Furthermore, the increased amount of SUHII is mostly concentrated in high and dense buildings. Further, the maximum SUHI intensity was registered by Dubai International Airport. In comparison, due to the COVID-19 pandemic lockdown in the UAE, SUHI and air pollutants have declined.

Keywords: Remote Sensing, MODIS, LST, Thermal Anomaly, Soil Salinity, Air Temperature, SUHI, COVID-19.

Title and Abstract (in Arabic)

تطبيقات درجة حرارة السطح من الاقمار الصناعية على دولة الامارات العربية المتحدة

الملخص

يتسبب التوسع الحضري السريع في المدن في جميع أنحاء العالم في حدوث تغيرات كبيرة في استخدامات وغطاء الاراضي لؤى لأطلأ الألأض، حيث صنف كاحد لألأ التاثيراتلألألأيلأ على المناخ. ونظراً للنمو السكاني السريع في دول الامارات العربية المتحدة، قد يتسبب في ..د كبير على البيئة والتي تؤدي الى عواقب على جودة الحياة. درجة حرارة السطح المستمدة من الاستشعار عن بعد لها اهمية متزايدة في دراسات مختلفة. في هذا البحث تم الحصول على درجة حرارة السطح من الحساس موديس. ويضم فصل المقدمة و خمسة اجزاء عن بعض تطبيقات درجة حرارة السطح المستمدة من موديس على دولة الامارات العربية المتحدة. وهي كالتالي: (1) كشف الشذوذ الحراري لكشف المياه الجوفية بعد يوم ممطر (2) دراسة العلاقة بين الملوحة ودرجة حرارة السطح (3) تقدير درجة حرارة الهواء (4) دراسة جزيرة الحرارة الحضرية الليلية و (5) كشف تاثير الحظر بسبب فايروس كوفيد-19 على ملوثات الهواء و جزيرة الحرارة الحضرية الليلية. تشير النتائج انه بعد يوم ممطر تم الكشف عى الشذوذ الحراري بسبب المياه الجوفية ومنه يمكن التنبؤ بالمواقع المثلى للمياه الجوفية. اظهرت ملوحة التربة ارتباطاً وثيقاً مع درجة حرارة السطح الليلية. بالاضافة، اشارت دراسة تقدير درجة حرارة الهواء الى اهمية موديس كبيديل موثوق لدرجة حرارة الهواء. فيما يتعلق بالجزيرة الحراريةلحضرية في امارة دبي، فقد زادت بشكل تدر يجيم مع تطور المدينة. بالاضافة انها تتركز في الغالب على المباني ذات الكثافة العالية والمرتفعة، كما سجل مطار دبي الدولي اعلى كثافة لجزيرة الحرارة الحضرية. بينما انخفضت مع ملوثات الهولا لالال فترة حظر كوفيد-19 في دولة الامارات العربية المتحدة.

مفاهيم البحث الرئيسية: الاستشعار عن بعد، موديس، درجة حرارة السطح، الشذوذ الحراري، ملوحة التربة، الجزيرة الحرارية الحضرية، كوفيد-19.

Acknowledgements

There are a number of thanks due as I finish this dissertation. I am greatly indebted to United Arab Emirates University, for giving the opportunity to pursue higher studies and financial support provided by college of graduate studies for which I am very grateful.

I would like to whole-heartedly acknowledge my wonderful advisory panel Dr. Abdelgadir Abuelgasim, Prof. Ala Aldahan, Dr. Hakim Saibi, Prof. Mohamed Hereher and Prof. Ayad Al-Quraishi. There are so many horror stories about unsupportive, non-communicative PhD supervisors which makes me feel so very lucky to have had you all as part of my team. You have all been so amazingly supportive and helpful, always making time when I needed it, and providing invaluable advice and guidance. I have learnt so much over the last few years and grown as a researcher, for which I will be forever grateful.

I would also like to thank the chair and all members of the Department of Geography and Urban Sustainability at the United Arab Emirates University for assisting me all over my studies and research. My special thanks are extended to the Library Research Desk for providing me with the relevant reference material.

My family has played an incredible role in making me what I am today. Special thank goes to my parents, wife, son and daughters for all the support, time and patience they have given me to accomplish my thesis. They are the unfailing resources of life sustaining enthusiasm and vitality. I thank my family for such rare and tremendous support.

Finally, I thank everyone who helped me directly or indirectly in carrying out this important research work.

Dedication

To:

my parents;

my wife, Ibtihal;

my son and daughters;

my brothers and sisters;

and the remote sensing community

Table of Contents

List of Tables

List of Figures

List of Abbreviations

ADH	Abu Dhabi
AJM	Ajman
AMJ	April, May and June
AOD	Aerosol Optical Depth
ASTER	Advanced Spaceborne Thermal Emission and Reflection Radiometer
AVHRR	Advanced Very High-Resolution Radiometer
BKH	Burj Khalifa
BSI	Bare Soil Index
COVID-19	Coronavirus Disease 2019
DEM	Digital Elevation Model
DER	Deira
DM	Municipality of Dubai
DTR	Diurnal Temperature Range
DUB	Dubai
DXB	Dubai International Airport
EAD	Environment Agency Abu Dhabi
EC	Electrical Conductivity
FAO	Food and Agriculture Organization
FUJ	Fujayrah
GEE	Google Earth Engine
GEP	Google Earth Pro
GIS	Geographical Information System
HSS	Hot Spot Sites
JAI	Jabal Ali Industrial

K	Degree Kelvin
LSE	Land Surface Emissivity
LST	Land Surface Temperature
LSTd	Daytime Land Surface Temperature
LSTn	Nighttime Land Surface Temperature
LULC	Land Use Land Cover
MAIAC	Multi-Angle Implementation Atmospheric Correction
MODIS	Moderate Resolution Imaging Spectroradiometer
NCM	National Center of Meteorology
NDII	Normalized Difference Infrared Index
NDVI	Normalized Difference Vegetation Index
NEUAE	Northern Emirates of the UAE
NO_2	Nitrogen Dioxide
ºC	Degree Celsius
RAK	Ras Al Khaymah
RMSE	Root Mean Square Error
RS	Remote Sensing
SCAD	Statistics Centre Abu Dhabi
Sentinel-5p	Sentinel-5 Precursor Satellite
SHJ	Sharjah
SRTM	Shuttle Radar Topography Mission
SUHI	Surface Urban Heat Island
SUHII	Surface Urban Heat Island Intensity
SZR	Shaikh Zayed Road
Ta	Air Surface Temperature
Ted	Mean Maximum Air Temperature Estimated

Ten	Mean Minimum Air Temperature Estimated
TIR	Thermal Infrared
T_{max}	Mean Maximum Air Temperature Observed
T_{min}	Mean Minimum Air Temperature
TOA	Top of Atmosphere
TRMM	Tropical Rainfall Measuring Mission
TROPOMI	Tropospheric Monitoring Instrument
TVX	Temperature Vegetation Index (TVX)
UAE	United Arab Emirates
UCI	Urban Cool Island
UHI	Urban Heat Island
UMQ	Umm Al Qaywayn
UMS	Um Suqaim
UN	United Nations
USGS	United States Geological Survey
WHO	World Health Organization

Chapter 1: Introduction

1.1 Overview

Rapid urbanization in cities causes major land use and land cover changes on the surface of the Earth. It has been classified as one of the climate's most significant anthropogenic influences (Zhou et al., 2011). United Nations show that by 2025, 60 to 70% of all population will reside in cities, and most of the fastest-growing regions for urban development will happen in arid regions. Interestingly, by 2019, in the United Arab Emirates (UAE), approximately 87% of people reside in urban areas (United Nations, 2019). In addition, in the UAE, Dubai City is rated as one of the ten growing cities globally, having growth rates ranging 6.3% to 9.3% each year as per United Nations (UN DESA, 2019). Economic growth, other than everything else, contributes to the growth of the population and is related to urban growth. As a result of the massive population expansion and industrialization growth in the UAE, the environment and consequences for quality of life, including public health and wellbeing, quality of air, energy and water use, and far more, could have caused tremendous stress. Therefore, physical consequences should be considered.

In addition, severe water deficits are affecting the UAE, along with the lack of perpetual streams or rivers and lakes. Additionally, in keeping with capita water consumption, the UAE has the highest in the world (Alam et al., 2017). It is, therefore, crucial for groundwater exploration to be acknowledged in order to meet the growing requirement for freshwater in such a region. Moreover, the scarcity of perennial water supplies makes groundwater in the UAE surely the only source of water. So, it is essential to recognize groundwater exploration.

Also, either human or natural induced, soil salinity is deemed an environmental hazard that is a major issue of land degradation, low economic yields, low agricultural productivity, as well as soil erosions are some of the effects of salinity. Furthermore, it influences urban infrastructure due to of corrosion, subsidence, and the quality of groundwater. Soil salinity must, however, also be taken into account.

One of the most crucial climatological variable and the global change is Air Surface Temperature (Ta). Within the hydrosphere, atmosphere, and biosphere, it controls multiple physical and biological processes. Accurate mapping its spatial-temporal distribution is therefore beneficial in a broad variety of applications in the field of hydrology, agriculture, climate change, environment, ecology, and social applications (El Kenawy et al., 2019b; Hooker et al., 2018; Huang et al., 2015; Janatian et al., 2017; Meyer et al., 2016; Noi et al., 2016; Shah et al., 2012; Sun et al., 2014; Zhu et al., 2013).

Additionally, the change of land surface from natural to impervious changes surface properties because of urban growth, leading in reduced albedo, a larger proportion of latent and sensible heat flux, and more massive surface energy storage in urban areas. As a result, urban areas generate hotter temperatures than the surrounding rural areas, which called Urban Heat Island (UHI) phenomena (Hu & Brunsell, 2013; Miles & Esau, 2017). On the basis of air temperature, UHI is calculated. While the Surface UHI (SUHI) is performed utilizing satellite-derived Land Surface Temperature (LST) data. Besides, the air pollutants emissions are the most critical component of human activities. It is one of the features of the new era, with both the growing use of natural gas and oil fuels in different sides of life. Many air pollutants such as Nitrogen Dioxide (NO_2) and aerosols originating from industrial operations or various transport systems are dispersed in the environment. The air

pollutants correlated to respiratory health problems and has adverse environmental effects like water and soil acidification (Griffin et al., 2019; Mulenga & Siziya, 2019; Xu et al., 2020). The effect of the lockdown of COVID-19 on SUHI and air pollutants has therefore been studied.

1.2 Thermal Remote Sensing

Remote sensing is known as the art and science of extracting information about areas, objects, or phenomenon under investigation by a device from distance (Lillesand et al., 2004). The advantage of utilizing remote sensing are that wide areas can be covered with less time, which is comparatively inexpensive than field measurements.

Remote sensing utilizes multiple parts of the electromagnetic spectrum for different applications in which Thermal Infrared (TIR) remote sensing deals with the processing and interpretation of data obtained mainly in the thermal infrared part of the electromagnetic spectrum. All objects consist of particles composed of random motion over absolute zero Kelvin. As they collide, based on an object's kinetic temperature, they alter their energy state and release electromagnetic radiation. The electromagnetic radiation emitted by an object is termed as radiant flux and calculated in Watts (Cohen, 2009). The measurement of the amount of radiant flux energy released from an object is its radiant temperature. A high positive association typically occurs between an object's kinetic temperature and the amount of radiant flux emitted from the object. Hence, to calculate its radiant temperature, radiometers are positioned at any distance from the object, which corresponds well with the kinetic temperature of the object. This is the starting point of TIR remote sensing (Dash et al., 2002). TIR remote sensing calculates the emitted radiation from the surface of the earth, in comparison to optical remote sensing, where it generally measures the reflected

radiation from the surface of the earth. The radiation released by the earth's surface is much larger than the solar reflected radiations in the TIR field of the electromagnetic spectrum. Sensors working in the TIR wavelength region thus detect mainly the thermal radiative properties of the Earth surface (Chuvieco, 2009). The Earth has a mean temperature of approximately 300 K, as well as its electromagnetic emitted radiance peak is situated in the electromagnetic spectrum region of around 9.7 μm (Figure 1.1).

The region of 3 μm to 35 μm is commonly termed as the TIR area in terrestrial remote sensing. Nevertheless, the TIR region is somewhat separately described by various authors. Data acquisitions are only performed in regions with minimum spectral absorption defined as the atmospheric window for remote sensing of the surface of the earth throughout all mission planned of remote sensing for land applications. Although, there is no negligible emission and atmospheric absorption within these atmospheric windows. As shown in Figure 1.2, the electromagnetic spectrum region of the atmospheric window locates between 3-5 μm and 8-14 μm. The attenuation caused by the atmospheric constituents is the lowest in the 3 to 5 μm atmospheric window area. However, The at Sensor/ Top of Atmosphere (TOA) radiance in the 3-5 μm region is influenced by reflecting solar radiation demonstrated in Figure 1.2 during the daytime. In this region, the solar radiance is around 8 to 10 times the emitted radiance at 300 K from the surface of the Earth. On the other side, the surface of the earth releases roughly 80% of the energy obtained by the satellite-based TIR sensor in the region of 10.5 to 12.5 μm (Figure 1.1). Within this region, there is a small contribution from the solar scattering and solar reflected radiation, allowing the Land Surface Temperature (LST) retrieved most suitable in this region (Jensen, 2009; Waring & Running, 2007).
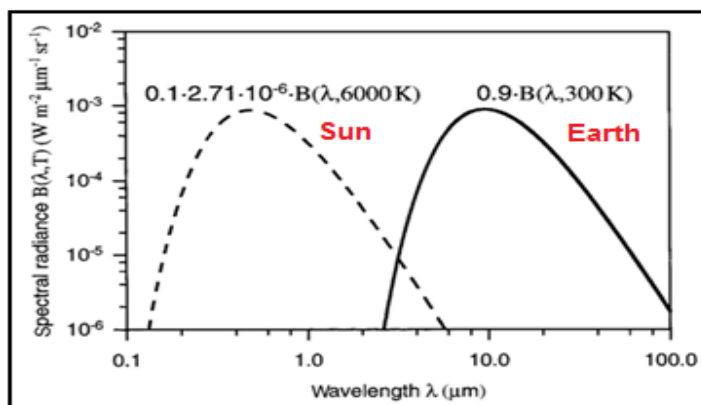
Figure 1.1: The Solar irradiance and Earth-emitted radiance. Adapted from (Dash et al., 2002)
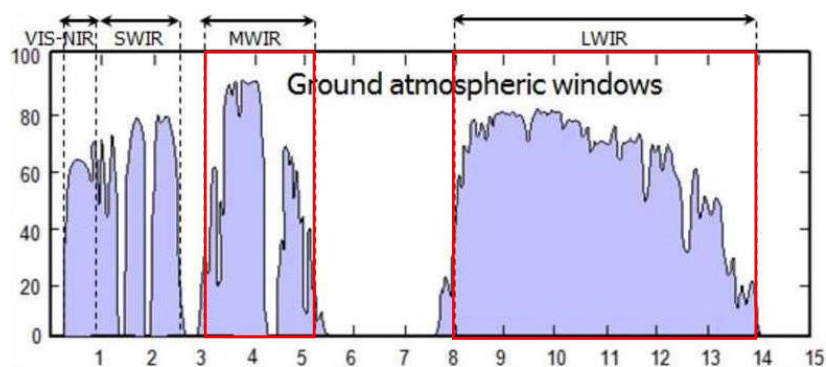
Figure 1.2: Range of the transmission of the IR spectra ground atmospheric windows. Adapted from (Olaguer, 2017)

1.3 Methods for LST Retrieval

Many attempts have been made to build methods for retrieve the LST from the remote sensing data. According to Li et al. (2013) and Du et al. (2015), these algorithms have been broadly classified into three classifications: (1) single-channel, (2) multichannel (e.g., the temperature and emissivity separation method and the split-window algorithm); and (3) multi-time methods (e.g., two-temperature method, the temperature-independent spectral indices method and the physical day and night algorithm).

The single-channel method will approximate LST from sensors for a single TIR channel. While multi-channel and multi-time methods can estimate LST and Land Surface Emissivity (LSE) from sensors with multi-TIR channels like Advanced Spaceborne Thermal Emission and Reflection Radiometer (ASTER), Advanced Very High-Resolution Radiometer (AVHRR), Moderate Resolution Imaging Spectroradiometer (MODIS), etc. In this study, the concentration was on methods such as split-window and physical day and night algorithms being used to approximate LST from MODIS.

The split-window methods use two TIR bands are usually situated in the atmospheric window within 10 and 12 μm. The most common method for LST retrieval from the satellite data is the split-window algorithm (Wang et al., 2019b). For the MODIS data, LST retrieval is carried out primarily through the implementation of split-window methods (Zhao et al., 2009). Researchers have developed numerous split-window algorithms focused on variation and impact of the atmosphere and emitting surface (Mao et al., 2005; Sobrino et al., 2003; Wan, 2014; Wan & Dozier, 1996; Wang et al., 2019b).

LSE and LST are obtained simultaneously by the MODIS Day / Night Algorithm (A physical algorithm). To retrieve LST and LSE from MODIS day and night data, Wan and Li (1997) proposed the MODIS Day / Night Algorithm. For the solution of land-surface and atmospheric parameters, fourteen equations are developed based on day/night measurements of the seven infrared MODIS channels, from which LST and LSE can be obtained. In the day and night observation, geometrical corrections are required to reference the two scenes (Liang et al., 2012).

Latest retrieval approaches are constantly being established in the ongoing quest to enhance the accuracy of LST estimation via remote sensing, allowing

utilization of the latest satellite sensors and leveraging growing computing power for data processing and analysis. There are numerous different satellite remote sensing platforms with many sensors in the TIR spectrum, offering the current meteorologist a variety of potentially valuable datasets for LST measuring. Datasets are available for various time periods, at various resolutions, with differing accuracy. The different datasets available are thus summarized in Table 1.1. Notice that this table does not include private or commercial satellites, as they are typically not as accessible to researchers.

Table 1.1: Summary of current Typical Thermal Infrared (TIR) sensors aboard satellite platforms for land surface temperature

Sensor/Satellite	Channel(s)	TIR spectral range (μm)	Spatial resolution (m)
OLI/Landsat 8	10	10.6-11.2	100
	11	11.5-12.5	
ETM+/Landsat 7	6	10.4-12.5	60
TM/Landsat 5	6	10.4-12.5	120
AVHRR/NOAA	4	10.30-11.30	1100
	5	11.50-12.50	
MODIS/Aqua; Terra	31	10.78-11.28	1000
	32	11.77-12.27	
ASTER/Terra	10	8.125-8.475	90
	11	8.475-8.825	
	12	8.925-9.275	
	13	10.25-10.95	
	14	10.95-11.65	

Table 1.1: Summary of current Typical Thermal Infrared (TIR) sensors aboard satellite platforms for land surface temperature (Continued)

Sensor/Satellite	Channel(s)	TIR spectral range (μm)	Spatial resolution (m)
AATSR/ENVISAT	11 \ 12	Central wavelength: 10.85 & 12.0	1000
SLSTR/Sentinel-3	S7 \ S8 \ S9	Central wavelength: 3.74, 10.85 & 12.0 \ \ Channel width: 0.38, 0.9 & 1.0	1000
SEVIRI/MSG	9 \ 10	Central wavelength: 10.8 & 12.0	3000
IRMSS/CBRES-1	9	10.4-12.5	300
MERSI/FY-3	5	Central wavelength: 11.25	1000
IRMSS/HJ-1B	4	10.5-12.5	300
S-VISSR/FY-2	IR1 \ IR2	10.3-11.3 \ 11.5-12.5	5000
GOES	4 \ 5	10.2-11.2 \ 11.5-12.5	4000
VIRR/FY-3	4 \ 5	10.3-11.3 \ 11.5-12.5	1100

Source: (Hulley et al., 2019; Sattari & Hashim, 2014; Tomlinson et al., 2011)

1.4 LST Definition and Terminology

Land Surface Temperature (LST) is the temperature of the skin of the Earth. It reflects the amount of radiation emitted from the surface and sub-surface of the Earth (Weng et al., 2019). LST is a vital variable in the inland surface processes,

environmental and climatological studies as it has a crucial role in the energy exchange in between both the atmosphere and the surface of the Earth in different forms (Song et al., 2018b). Turbulent sensible and latent heat fluxes, long-wave radiation flux, and ground heat storage are included in these forms (Benas et al., 2017). LST knowledge is a core component of the science of other Earth systems (Li et al., 2013). it has been utilized in evapotranspiration, soil moisture, evapotranspiration, urban heat island as well as other studies (Peng et al., 2018; Song et al., 2018a; Zhao et al., 2016). LST obtained from satellites is extensively utilized in numerous scientific areas related to the assessment of land surface conditions, from local to global scales including climate change, the energy budget, the monitoring of vegetation, the hydrological cycle, and the climatology of urban (Ermida et al., 2020; Khandelwal et al., 2011; Voogt & Oke, 2003).

1.5 Statement of the Problem

The UAE has been established in 1971. It is approaching its fifty years of establishment with great fanfare and celebrations. During the past fifty years the UAE has undergone massive transformations and change and has become an attractive tourist place in the region. During these last fifty years the country has set it economic and social programs in transforming the desert place into a highly advanced urbanized country. Large residential cities were created, impressive and modern infrastructure, and a vibrant and growing economy. Such rapid changes have been mostly achieved only in the last fifty years.

Urbanization, tourism, and socio-economic development comes at a price. There has been an associated changes in the local environment and major disturbances to both the terrestrial and marine ecosystems in the country. One major impact is the

expansion in agricultural practices leading to significant depletion of the limited ground water resources. In a desert and semi-arid regions this is a major challenge that impacts any future agricultural expansion.

The massive residential and infrastructure development has impacted the desert surface and to a limited extent, so far, has disturbed the ancient salt flats ecology with its diverse wildlife habitats. The construction of large residential centers and towns has an adverse effect of creating urban heat islands within the desert landscape that has not been present before and also lead to low urban air quality.

Studying the impacts of urbanization, ground water depletion, and soil degradation are important environment issues to address. Without proper assessment of the impacts of these environmental issues the consequences might derail and impact any future developments within the country.

Remotely sensed data provides an ideal source of data for studying environmental problems at global, regional and local scales. Such data usually covers large geographic regions, comes with high quality at different spectral ranges, and provides continuous repetitive coverage. Of the different types of earth observation data is thermal data collected over terrestrial surfaces. Thermal remotely sensed data is particularly concerned with measured the thermal radiance emitted from terrestrial surfaces due to their thermal energy. For tacking some of environmental issues facing the UAE thermal remote sensing offers a wide suit of applications, in particular to the issues raised earlier of ground water assessment, urban heat islands phenomenon, retravel of air temperature in remote and vast areas, salinization, and urban air quality. This research is predominantly focused on the applications of thermal remote sensing for addressing some of the environmental problems facing the UAE. In particular this research will focus on:

i. Detect groundwater flow by thermal anomalies.

ii. Detect and model the soil salinity using several spectral indices and evaluate the relationship between soil salinity and the estimated LST.

iii. Estimate air temperature across UAE country.

iv. Assess Surface Urban Heat Island Intensity (SUHII).

v. Investigate the impact of COVID-19 on the concentration of Nitrogen Dioxide (NO_2), Aerosol Optical Depth (AOD) and SUHI.

1.6 Structure of the Dissertation

Six chapters are contained in this dissertation and the content of the chapters is as follows:

Chapter 1 starts with a brief overview, background of remote sensing Land Surface Temperature (LST), it also includes related literature, a statement of the problem, as well as the structure of the dissertation as an introduction to the research. Chapter 2 includes the thermal anomalies detection in Eastern Abu Dhabi from Remote Sensing and Geophysics. Chapter 3 provides modeling soil salinity and investigation the relationship between soil salinity and Land Surface Temperature (LST) over arid area, UAE. Chapter 4 covers estimation of air temperature using MODIS LST over UAE. Chapter 5 gives the analysis of night Surface Urban Heat Island (SUHI) using nighttime MODIS Land Surface Temperature data in Dubai city. Chapter 6 contains the impact of COVID-19 lockdown upon air pollutants and SUHI over Northern UAE. Finally, it summarizes significant findings of the dissertation.

1.7 Review of Literature

A summary of MODIS characteristics will be presented in this subsection. In addition, this subsection concentrates on prior studies linked to some LST applications with a concentrate on air temperature estimation, SUHI, the relationship between LST and salinity of the soil, thermal anomaly, lockdown effect of COVID-19 on air pollutants.

1.7.1 MODIS Characteristics

The most typical satellites being used in LST applications are Landsat, ASTER, AVHRR and MODIS, among the significant operational remote sensing satellite systems listed in Table 1.1 in Section 1.3. In terms of spatial resolution, Landsat has tremendous strength, but it has a revisit time of 16 days and lack of night-time image acquisition is constrained on a temporal scale. In addition, the small size of Landsat images, as extended to regional and national regions, numerous images must be mosaicked. Furthermore, notwithstanding the fact that ASTER LST standard items have been accessible since 2001. In 2016, the entire ASTER data archive was made accessible free of cost, so the historical data is restricted. Additionally, like Landsat, ASTER has a coarse temporal resolution of 16 days. In addition, due to the AVHRR involves complex procedures for pre-processing and AVHRR efficiency, LST is not quite as good as MODIS LST (Noi et al., 2017). Furthermore, in calculating LST over continental regions, there is high uncertainty (Khorchani et al., 2018). Therefore, the MODIS has been selected in this research.

The strengths of the MODIS instrument comprise its worldwide coverage, high temporal resolution (four daily overpasses at about 1:30 AM and 1:30 PM, and at 10:30 AM and 10:30 PM, local time). It is characterized by high radiometric resolution and

dynamic ranges, free and easy to access, and accurate calibration in visible, near-infrared, and thermal infrared bands. It has been widely utilized in various studies and applications, especially on a diverse scale (e.g., local, regional, and worldwide). Thus, a considerable amount of attention is paid by scholars to MODIS LST data (Phan & Kappas, 2018). In addition, relative to all other sensors that provide higher spatial resolution but poorer temporal resolution, or higher temporal resolution but poorer spatial resolution, the MODIS sensor is a balance among both normal image acquisition and reasonable spatial resolution. Overall, of all the other remotely sensed data, MODIS is by far the most prevailing data source. MODIS LST is the most known and highly used source for LST applications such as soil moisture estimation, air temperature estimation studies, thermal anomaly, UHI phenomena, evapotranspiration, as well as drought (Phan & Kappas, 2018). Consequently, the publications with the MODIS was highest when compared with Landsat, ASTER and AVHRR (Tomlinson et al., 2011; Zhou et al., 2019).

The MODIS instrument has been onboard NASA's Terra and Aqua Earth Observation System satellites. Terra was launched on December 18, 1999, while Aqua was launched on May 4, 2002. The MODIS sensors onboard the Terra and Aqua satellites have 36 spectral channels with a viewing swath range of 2330 km, spanning the electromagnetic spectrum from 0.4 μm to 14 μm. MODIS is in orbit at a low altitude (705 km). Furthermore, their orbital parameters are 1-2 days of worldwide coverage and include LST four times every day, including daytime and nighttime. Terra ascends past the equator at about 10:30 AM, and at about 10:30 PM, it descends past the equator. In contrast, Aqua crosses the equator in opposing directions at around 1:30 AM and 1:30 PM. Around the same time, satellites pass over the same location on Earth every 24 hours. To derive the MODIS LST, two thermal infrared band

channels have been used, 31 (10.78 μm–11.28 μm) and 32 (11.77 μm–12.27 μm) utilizing the split-window algorithm, (Wan et al., 2002). These MODIS products have been submitted for consistent validation. According to the outcomes of ground validation of these LST products, the accuracy is 1 Kelvin in most of the cases underneath the clear the sky, and therefore can meet criteria for the accuracy of most LST modelling applications (Wang et al., 2008). The generalized method of split-window algorithm rectifies the atmospheric effects, based on dissimilar absorption in adjoining infrared bands. Spatial resolution for bands 1 to 2 is 250 m, for bands 3 to7 is 500 m, and for band 8 to 36 it is 1000 m. All comprehensive explanations of the MODIS features are given in Table 1.2, acquired from (https://modis.gsfc.nasa.gov/).

Table 1.2: MODIS spectral bands, associated spatial resolution and its primary use

Primary use	Band no.	Bandwidth	Spatial resolution
Land/Cloud/Aerosols Boundaries	1	620 - 670 nm	250 m
	2	841 - 876 nm	
Land/Cloud/Aerosols Properties	3	459 - 479 nm	500 m
	4	545 - 565 nm	
	5	1230 - 1250 nm	
	6	1628 - 1652 nm	
	7	2105 - 2155 nm	
Ocean Color/ Phytoplankton/ Biogeochemistry	8	405 - 420 nm	1000 m
	9	438 - 448 nm	
	10	483 - 493 nm	
	11	526 - 536 nm	
	12	546 - 556 nm	
	13	662 - 672 nm	
	14	673 - 683 nm	
	15	743 - 753 nm	
	16	862 - 877 nm	
Atmospheric Water Vapor	17	890 - 920 nm	1000 m
	18	931 - 941 nm	
	19	915 - 965 nm	

Table 1.2: MODIS spectral bands, associated spatial resolution and its primary use (Continued)

Primary use	Band no.	Bandwidth	Spatial resolution
Surface/Cloud Temperature	20	3.660 - 3.840 µm	1000 m
	21	3.929 - 3.989 µm	
	22	3.929 - 3.989 µm	
	23	4.020 - 4.080 µm	
Atmospheric Temperature	24	4.433 - 4.498 µm	1000 m
	25	4.482 - 4.549 µm	
Cirrus Clouds Water Vapor	26	1.360 - 1.390 µm	1000 m
	27	6.535 - 6.895 µm	
	28	7.175 - 7.475 µm	
Cloud Properties	29	8.400 - 8.700 µm	1000 m
Ozone	30	9.580 - 9.880 µm	1000 m
Surface/ Cloud Temperature	31	10.780 - 11.280 µm	1000 m
	32	11.770 - 12.270 µm	
Cloud Top Altitude	33	13.185 - 13.485 µm	1000 m
	34	13.485 - 13.785 µm	
	35	13.785 - 14.085 µm	
	36	14.085 - 14.385 µm	

Source: https://modis.gsfc.nasa.gov/about/specifications.php

1.7.2 Previous Studies

In the physics of land surface processes, the knowledge of LST from local to global scales is important. In a number of fields, the LST is extensively used. Numerous LST applications are briefly presented below. It is noteworthy to mention that in this research, targeted applications are linked to all given applications.

Regarding the thermal anomaly's studies, thermal anomalies associated with faults in the Jinhua Quzhou basin of Zhejiang Province, China observed by Wu et al. (2012) using Landsat 5 and they found the LST near a fault are higher than in other areas and can indicate the strike trend of an underground fault. By using MODIS LST data, in China, the thermal anomalies were detected before 2013 Songyuan earthquake according to (Zhang et al., 2014b). The western province of Al Najaf in Iraq, a phenomenal underground fire was detected by using MODIS LST data (Abbas et al., 2015). Over northern UAE, the study by Ghoneim (2008) revealed that a large volume of groundwater is dissipated into the sea along the eastern coast. A detailed examination of MODIS thermal data supports this by revealing cool surface anomalies issuing from the mountain range toward both the western desert plain and the Gulf of Oman following major rainfall events.

Also, in Dujaila, Iraq Wu et al. (2014a) using Landsat TM and ETM+ for mapping soil salinity and they found that LST and soil salinity are relevant. Also, Hereher (2017a) addressed the change in LST resulted from the emergence and disappearance of Toshka lakes, in the western desert of Egypt as the main Land Use and Land Cover (LULC) change in the region to salinized soils.

Since early 2000 (Terra) and mid-2002 (Aqua) MODIS LST data has received much attention and has been used for air temperature estimation also has shown its suitability as a proxy for Ta in various regions of the world such as: in the Canada

(Xu et al., 2014), USA (Zeng et al., 2015), Africa (Vancutsem et al., 2010), Antarctica (Meyer et al., 2019), Brazil (Neves et al., 2016), Vietnam (Phan et al., 2019), Cyprus (Georgiou & Varnava, 2019), UK (Tomlinson et al., 2012), Spain (Serra et al., 2020), Croatian (Pepin et al., 2019), Portugal (Benali et al., 2012), China (Rao et al., 2019; Zhao et al., 2019), India (Shah et al., 2012, 2013), Tibetan Plateau (Pepin et al., 2019), Nepal (Zhou et al., 2017b), Thailand (Misslin et al., 2018), Mongolia (Otgonbayar et al., 2019), as well as in Middle East such as, Egypt (El Kenawy et al., 2019a, 2019b; Hereher & El Kenawy, 2020), Iran (Janatian et al., 2017) and Oman (Hereher, 2019). Additionally, AVHRR images have been used to estimate air temperature over Morocco (Hadria et al., 2019). Their results serve as a verification of MODIS products' precision that meet the requirements for estimating air temperatures.

Weng (2003) used three Landsat TM images (from 1989, 1996 and 1997) to study the SUHI in Guangzhou, China alongside fractal analysis with the result that two significant heat islands existed in the city. Keeratikasikorn and Bonafoni (2018b) utilized Landsat 8 to examine the daytime SUHI pattern identification within the different land use in Bangkok, Thailand. Their result exhibited that the highest mean SUHI intensities were placed in the city core. Using multi-temporal NOAA AVHRR, Streutker (2003) quantified the UHI of Houston city, Texas with a 2-D Gaussian surface, monitored its growth over 12 years. He found that the magnitude and spatial extent of the UHI had closely followed the urban expansion of Houston city in terms of population distribution. In Middle East, Rasul et al. (2015) , used Landsat 8 data to investigate the spatial variation of LST and the daytime SUHI intensity in 2013 in Erbil, Kurdistan Iraq. They concluded that urban areas are cooler than surrounding areas, which called Urban Cool Island (UCI). More recently, AVHRR images have been used to the assessment of SUHI in three cities (Paris, Riyadh and Manama)

Surrounded by different types of land cover. The temperature variation analysis showed that the behavior of SUHI is not the same in different cities and dependent on the land covers surrounding the city (Sherafati et al., 2018). In the UAE, the UCI phenomenon at daytime has been investigated by using ASTER data. The investigations showed in the daytime a distinct surface cool island for Dubai and surface cool areas at Abu Dhabi city and its surrounding mangrove areas (Frey et al., 2007). By used MODIS LST data, there are a number of UHI studies. For example, within Middle East, (Alahmad et al., 2020; Alali, 2015; Haashemi et al., 2016; Hereher, 2017b; Lazzarini et al., 2013; Schwarz et al., 2011). Globally, (Cheval et al., 2014; Clinton & Gong, 2013; Imhoff et al., 2010; Peng et al., 2012; Tan & Li, 2015; Tran et al., 2006; Yang et al., 2010; Yao et al., 2018a, 2019; Zhang et al., 2014a; Zhou et al., 2014, 2016b).

Atmospheric studies estimate aerosol optical depth (AOD: an important influence on the radiation budget) in America, Canada, China and Africa (Liang et al., 2006), and help detect clear sky, low-level temperature inversions in the polar regions (Liu & Key, 2003). Many recent studies have demonstrated a significant reduction in the level of air pollutants (e.g. $PM_{2.5}$, PM_{10}, CO, SO_2, NO_2, etc.) across the world during the COVID-19 pandemic (Archer et al., 2020; Collivignarelli et al., 2020; Dantas et al., 2020; Isaifan, 2020; Islam et al., 2020; Kaplan & Avdan, 2020; Karuppasamy et al., 2020; Kerimray et al., 2020; Nakada & Urban, 2020; Ranjan et al., 2020a; Tobías et al., 2020; Wang & Su, 2020). For the Middle East, a limited number of studies can be found in the literature. Otmani et al. (2020) studied the level of air pollutants over Morocco, while Nemati et al. (2020) studied the same changes in Iran. Similarly, they reported noticeable improvements in air pollution during the pandemic.

During the review in the relevant literature, the following gaps and areas were discovered that require more concentration: (i) no research has used thermal anomaly using LST data to detect groundwater flow in Abu Dhabi emirate, (ii) or assessed the relationship between LST and soil salinity over UAE, (iii) several studies estimated air temperature by using satellite data, but no research has been undertaken to estimate air temperature over the UAE. (iv) a literature search revealed few studies that investigated the spatiotemporal variation of UCI in arid climates. UHI has not been studied in UAE, (v) all previous studies have explored the impact of COVID-19 lockdown on air pollutants. Still UHI was not investigated during the pandemic lockdown.

Chapter 2: Thermal Structure Anomalies in Eastern Abu Dhabi from Remote Sensing and Geophysics

Abstract

In mid-August 2018, thermal anomalies were identified in the eastern Abu Dhabi Emirate (UAE). The thermal anomalies were obtained through satellite data from MODIS Aqua and were found to coincide with low Bouguer anomalies. The MODIS Aqua satellite data showed a drop in the land surface temperature (10.5ºC on 17th August and 2.5ºC on 24th August 2018) in some areas of eastern Abu Dhabi compared to surrounding areas. UAE's Bouguer gravity map shows a low tendency of Bouguer anomalies (-90 mGal to -40 mGal) in NW-SE over the same anomalies of thermal remote sensing. The low Bouguer anomalies are described as a graben structure which facilitates groundwater channeling from the recharge zones in Oman Mountains to the Arabian Gulf, thus producing the low thermal anomaly observed by the area's remote sensing data. The technique used facilitates the prediction of optimum groundwater resources in the eastern Abu Dhabi, which also may use in elsewhere in arid areas.

Keywords: Land Surface Temperature, Abu Dhabi, MODIS, Thermal Anomaly, Bouguer.

2.1 Introduction

Water is an integral component of mankind's life on Earth, covers about two thirds of the surface of the world. However, the fact is that less than 2.5% of the overall amount of water is freshwater, much of which is frozen in ice caps and glaciers (Gleick, 1993). These freshwater resources have an unequal geographical distribution on the

surface of the earth. Although some areas of the world suffer from excess water, others face extreme water shortages including the absence of permanent streams or lakes; the second category is the United Arab Emirates (UAE) (Alam et al., 2017). Rapid population growth, Climate change, urbanization, industrial development and agricultural irrigation demand will all affect future UAE water resources. According to Alam et al. (2017) report, the UAE has the world's maximum in keeping with capita water consumption, with the domestic consumption of only 13%, while 80% of water is utilized for different greening projects. Therefore, it is important to recognize groundwater exploration to meet the increasing demand for freshwater in such a region. The shortage of perennial water resources renders groundwater the only source of water in the UAE. So, the identification of groundwater exploration is important. Rainwater is the main groundwater recharge water source within the study region. During the winter months (December to February) approximately 80% of the annual rainfall occurs as a result of depressions and sometimes eastward-moving cold fronts from the Mediterranean. Moreover, the UAE area sits under the influence of monsoon rainfall during the summer (June through August). Hot surface temperatures and an uncertain layer in the lower atmosphere are sometimes responsible for the development of short-lived thunderstorms over the Oman Mountains and into the eastern UAE that may generate intense precipitation over small regions and short periods of time (Sherif et al., 2014).

Land Surface Temperature (LST) is an essential factor in the field of atmospheric sciences as it integrates the effects of all earth-atmosphere interactions and energy fluxes seen between the ground and the atmosphere (Song et al., 2018b). As a result, LST shows a positive indicator of the Earth's surface energy balance at local, regional, and global scales.

Due to the availability of groundwater in the shallow aquifer, the sand dune corridors served as an advantageous area for farming activity. The study area is characterized by three different types of flow systems: local, intermediate, and regional flow system (Alsharhan et al., 2001). As can be seen in Figure 2.8, the overall groundwater movement is generally from the east (Oman Mountain) to the west (Arabian Gulf).

The objectives of this research are to provide an approach that will help in identifying potential groundwater accumulation sites in the eastern part of Abu Dhabi by detecting groundwater flows in the period from 17 to 24 August 2018. For this, the thermal infrared imagery from MODIS Aqua and TRMM data to detect the thermal anomaly after a rainy day. Utilizing surface property details like land caver and the Digital Elevation Model (DEM) obtained from satellite remote sensing. In addition, the available gravity data helped us to understand the subsurface structure that consists and regulates the water flow in the region.

2.2 Study Area and Data

2.2.1 Study Area

The United Arab Emirates (UAE) is a federation of seven emirates primarily based on the Arabian Gulf's south-eastern coast, and Abu Dhabi's Emirate is the largest of the seven emirates (Figure 2.1). The field of study in Abu Dhabi emirate, which is situated between 22°30' and 24°55' north latitude and 51°35' to 56°25' east longitude. Over the last few decades, Abu Dhabi has experienced massive and continuous urban growth. The population reached 283,000 in 1985, while in 2016, according to the Statistics Centre Abu Dhabi (www.scad.gov.ae), the total population reached 2,908,000.
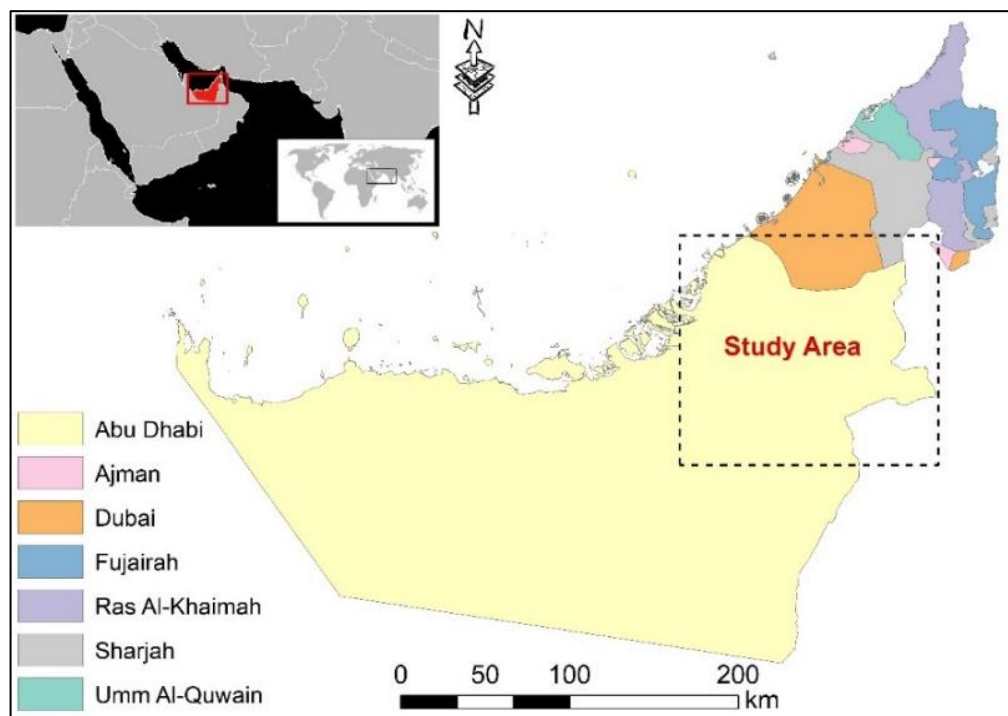
Figure 2.1: Location of study area (Abu Dhabi in UAE)

2.2.2 Data

Moderate Resolution Imaging Spectroradiometer (MODIS) is a sensor that works on the satellites Terra and Aqua. It is a high frequency revisit satellite mission over the UAE. Aqua travels through the country 13:00 and 01:00 local time, while the pass times for the Terra are 22:00 and 10:00. The data were collected with free accessibility from https:/earthexplorer.usgs.gov via the USGS Earth Resource Observation Systems Data Center. The data is of excellent quality with no cloud cover, from August 17th to 24th, 2018. The MODIS MYD11A1 Aqua: Land-surface temperature / Emissivity Daily version6 Global product with a spatial resolution of one km is used here. Day LST values are recorded in a Sinusoidal projection adjusted to the UTM zone of 39. The Tropical Rainfall Measuring Mission (TRMM) precipitation data was also utilized to comprehend which days of August 2018 had rain

to identify thermal anomaly, TRMM data was downloaded from (https://giovanni.gsfc.nasa.gov/giovanni). In addition, the 90 m resolution Digital Elevation Model (DEM) was derived from the NASA Shuttle Radar Topography Mission (SRTM) from (http://www.diva-gis.org/gdata). Figure 2.2 illustrates the UAE elevation map, from 0 m to 1875 m. Likewise, the Abu Dhabi Emirate land cover was retrieved from the Environment Agency Abu Dhabi (EAD) after it was reclassified into four classes (Desert/Barren land, visitation, Built-up and urban, and mountains) as illustrated in Figure 2.3. All maps were sent inside the same projection and clipped to GIS software for processing. Geosoft Seek Data (v 9.5.2) (2019) was used to obtain gravity data of the study area. ESRI ArcGIS™ 10.4 software was used for the processing, interpretation and visualization of the data and statistical factors were implemented using MS Excel.
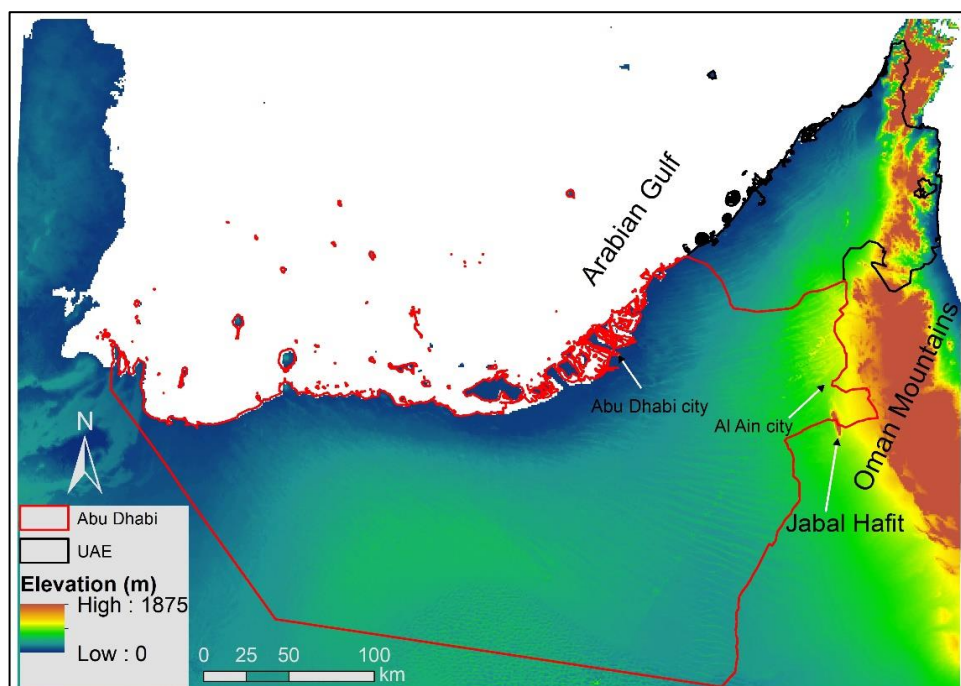
Figure 2.2: Elevation map of UAE
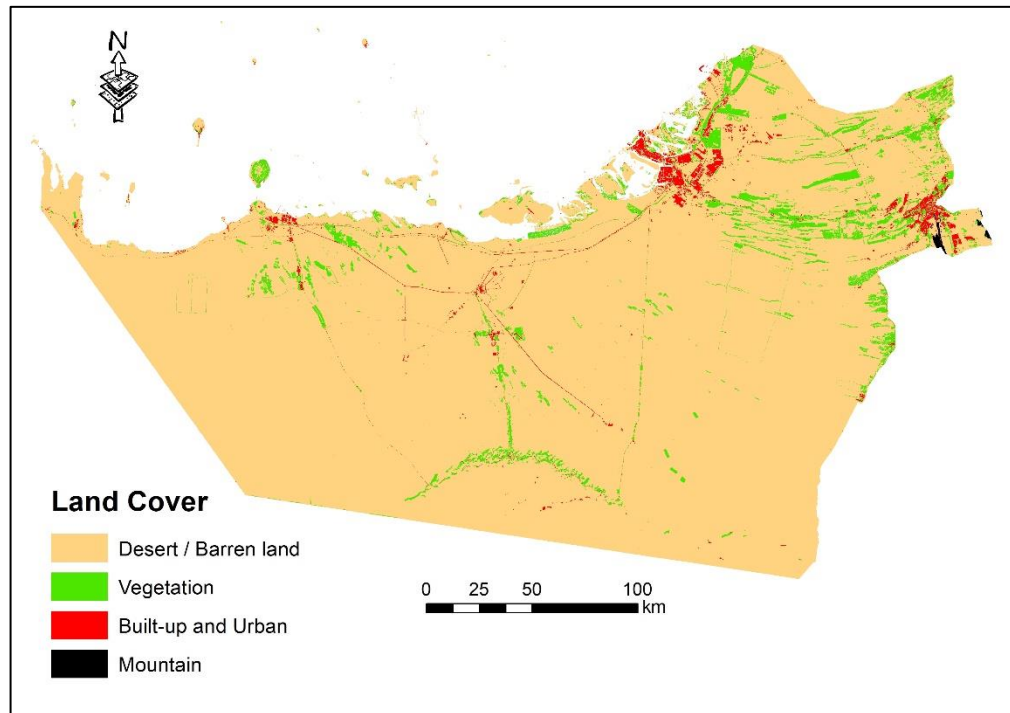
Figure 2.3: Land cover map of Abu Dhabi

2.3 Results and Discussions

In desert areas, all the absorbed sunlight goes into increasing the temperature of the dry soil's top layers. If the soil is moist, most of the energy from the incident sunlight is used to evaporate the water, which in turn cools the surface of the soil. This cooling process is an essential way of cooling the desert surfaces, as water absorbs a vast amount of heat as it becomes vapor. The desiccated soil becomes wet in the arid environment following straightforward rainfalls, but the wetting generally does not last that long due to the rapid frequency of infiltration or evaporation. At surface/subsurface water accumulation sites, furthermore, surface wetting is likely to remain longer than it would be elsewhere, possibly due to the constant flow of water from a distant recharge region. Because of the evaporative cooling at these areas the temperature will be slightly lower than that of the dry soil in the area. This temperature

difference wherever surface wetting overcomes gives rise to visible tonal variations in the thermal images, particularly during the summer daytime (El-Baz, 2010), where evaporation is most effective. Bright indicators in thermal images would signify warm soil surfaces (dry sand) while dark indicators would signify cold soil surfaces (wet sand). Based on this assumption that sustained surface wetting may be taken as an indirect indicator of groundwater accumulation, in the current analysis, satellite thermal data were used to locate surfaces with apparent moisture in the catchment areas of the eastern part of Abu Dhabi, were previously classified as sand dunes aquiver of very high groundwater potentiality (Alsharhan et al., 2001).

The systematic evaluation of MODIS LST's cloud-free daytime images correlated with those of the TRMM rainfall showed a large cooler anomaly in the study region. The anomaly, which is suggestive of moisture content on the subsurface, remained observed in the LST images for several days. It arises in the desert between Abu Dhabi and Alain city and progresses into the southern frontier of Dubai (Figure 2.4). The compounds and structure of the beds in the subsurface seem to make it easier for the rainwater to move from east (recharge) to west (aquifer) over vast underground distances (Figure 2.8).

LST maps were produced by mid-August 2018. These can be seen in Figure 2.4, which illustrates the anomaly found after a rainy day on August 16th 2018. Figure 2.5 represents the time span in which this thermal anomaly occurs. The LST data crossing the thermal anomaly at three positions A, B, and C (Figure 2.6) indicates lower temperatures than neighboring regions. It was also found that these areas have the same height as well as the same land cover (Figure 2.2 & 2.3). After a week, the cooler anomaly nearly vanished. On 17th August the variation in the observed temperature was around 10.5ºC and then on 24th August 2018, it decreased to 2.5ºC.

The UAE map of the Bouguer gravity anomaly can be seen in Figure 2.7. The Bouguer values range from -93.4 mGal to 29 mGal. East Abu Dhabi's thermal anomaly lies in the low Bouguer area (Figure 2.7). This low area of Bouguer is clarified in terms of a graben structure. This structure may play a role in channeling groundwater that flows from the eastern part (Oman region) to the western part (Arabian Gulf) and influences changes in LST (Figure 2.8). Overall, the technique used facilitates the prediction of optimum groundwater resources in the eastern Abu Dhabi, which also may use in elsewhere in arid areas.
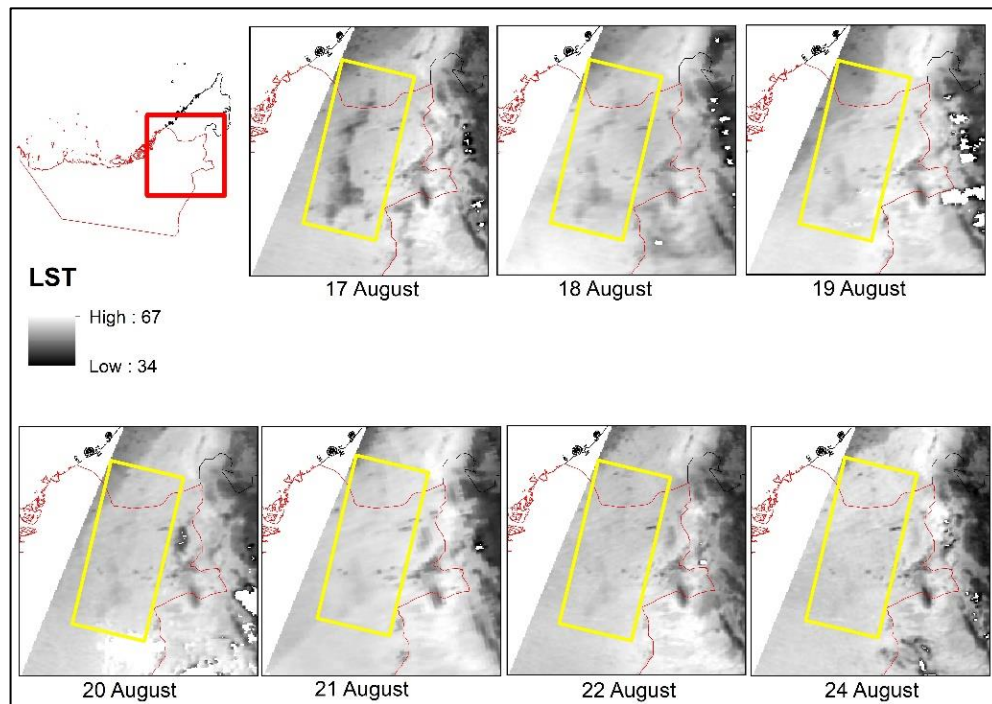
Figure 2.4: Thermal anomaly appearing in east Abu Dhabi from 17th of August 2018 to 24th of August 2018
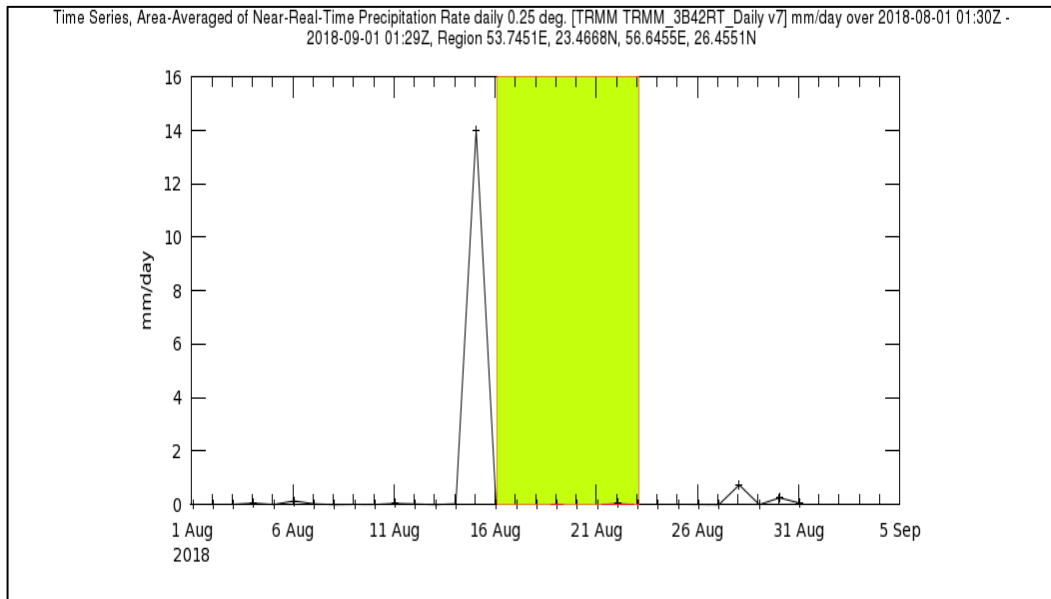
Figure 2.5: TRMM August data. Green zone indicates the time of thermal anomaly (after the day of rain, on 16 August 2018)
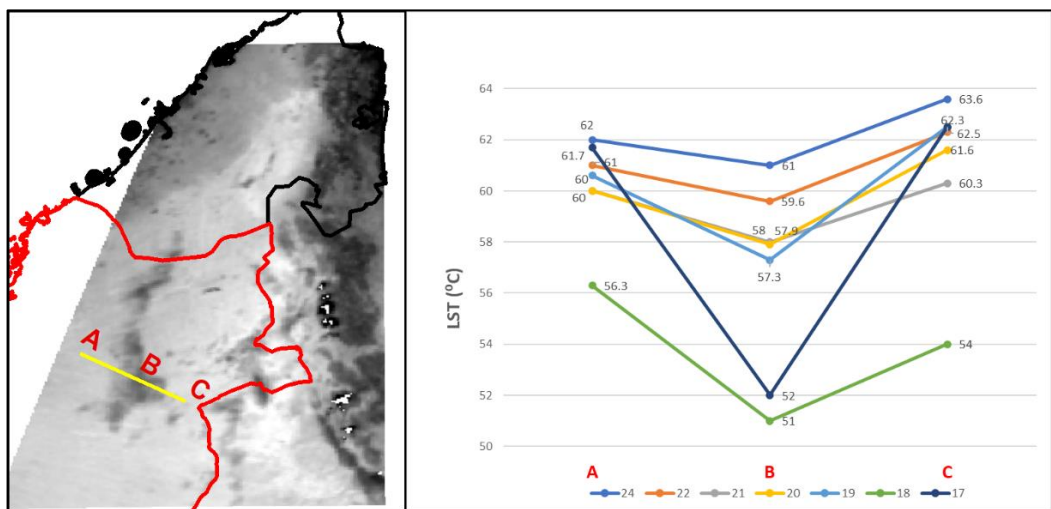
Figure 2.6: Land surface temperature (ºC) over the thermal anomaly
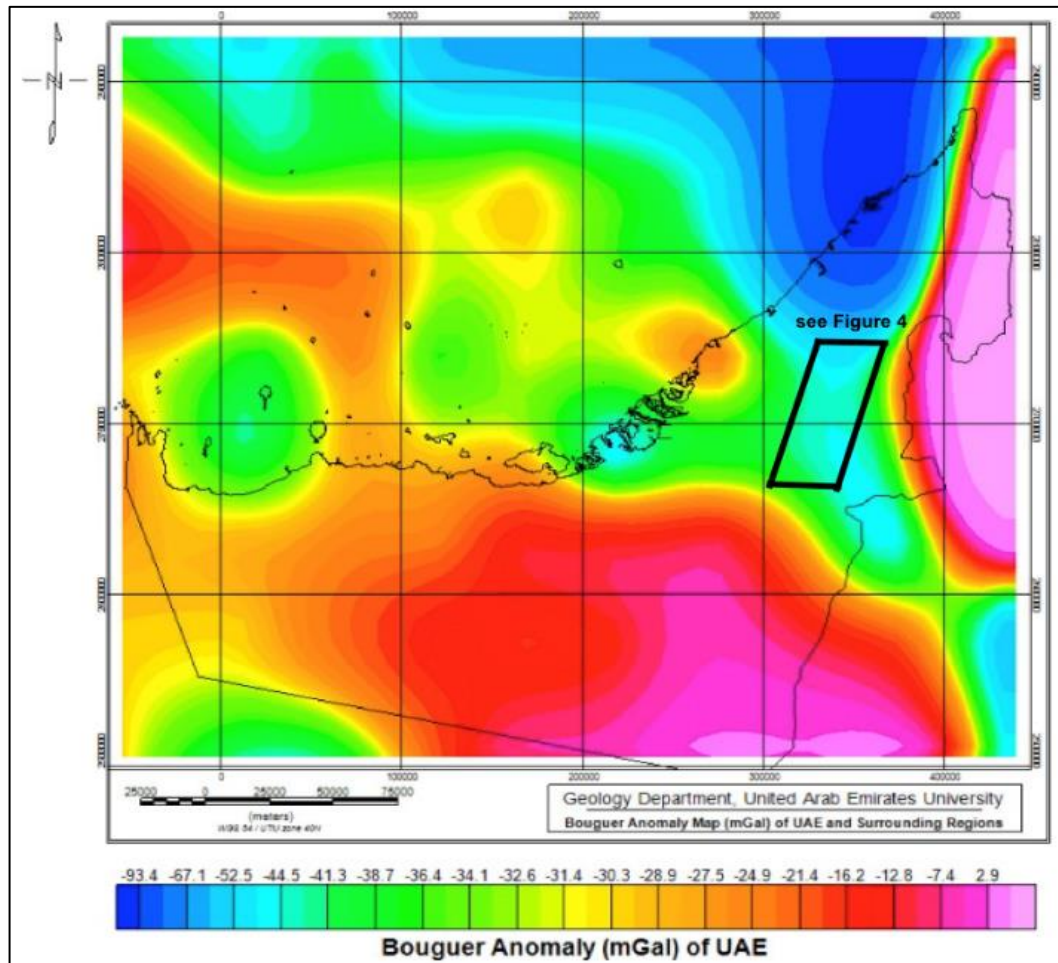
Figure 2.7: Bouguer gravity anomaly of UAE
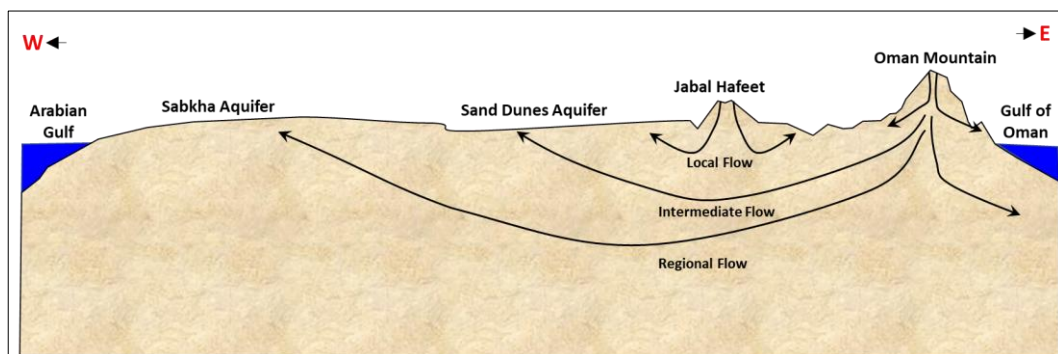
Figure 2.8: Modified groundwater flow mechanism. Adopted from Alsharhan et al., (2001)

2.4 Conclusions

Land surface temperature data from MODIS of eastern Abu Dhabi (UAE) suggests a short period (one week) low temperature anomaly after precipitation. The low Bouguer anomaly values clarified this anomaly, which symbolizes a graben structure that helps the flow of water from east to west and then boosts the moisture of the region's top-soils. While neither strategy alone can precisely map groundwater flow, collectively they form an incredibly low cost and synergistic approach for identifying regions beneficial to groundwater exploration. Additional geophysical instruments can be used in future studies to discover additional information about the subsurface structures. Besides high resolution remote sensing data.

Chapter 3: Detection and Modeling of Soil Salinity Variations in Arid Lands Using Remote Sensing Data

Abstract

Soil salinization is a ubiquitous global problem. The literature supports the integration of remote sensing (RS) techniques and field measurements as an effective method for developing soil salinity prediction models. The objectives of this study were to (i) estimate the level of soil salinity in Abu Dhabi using spectral indices and field measurements and (ii) develop a model for detecting and mapping soil salinity variations in the study area using RS data. Landsat 8 data was integrated with the electrical conductivity (EC) measurements of soil samples taken from the study area. Statistical analysis of the integrated data showed that the normalized difference vegetation index and Bare Soil Index (BSI) showed moderate correlations among the examined indices. The relation between these two indices can contribute to the development of successful soil salinity prediction models. Results show that 31% of the soil in the study area is moderately saline and 46% of the soil is highly saline. The results support that geoinformatic techniques using RS data and technologies constitute an effective tool for detecting soil salinity by modeling and mapping the spatial distribution of saline soils. Furthermore, it was observed a low correlation between soil salinity and the nighttime land surface temperature.

3.1 Introduction

Soil salinization, which is a common form of soil degradation, is one of the world's most widespread environmental problems (Farifteh et al., 2006; Fernandez-Buces et al., 2006; Ibrahim, 2016; Mougenot et al., 1993; Wu et al., 2014b). This global problem results in land degradation, especially in irrigated areas in arid and semiarid environments as well as in some sub-humid regions (Dehni & Lounis, 2012; Ibrahim, 2016). Soil salinization has become increasingly serious in recent decades, with salinization exceeding the average level of soil salinity in the past few years because of unsustainable agricultural practices that lead to the accumulation of soluble salts in soil (Ibrahim, 2016; Wu et al., 2014b; Omer, 2011). Soil salinization reduces the land value and productivity (Abuelgasim & Ammad, 2019; Elhag, 2016). By reducing the soil quality, soil salinization limits the suitability of the land for agriculture or reclamation and can increase soil dispersion and erosion.

Soil salinization is a severe environmental hazard that influences almost half of the existing irrigation plans of worldwide soils facing the threat of secondary salinization (Al-Khaier, 2003; Ibrahim, 2016; Zewdu et al., 2017). General estimates indicate that approximately one billion hectares of land are affected by salinization worldwide, constituting 7% of the continental area of the Earth and 58% of irrigated land (Ghassemi et al., 1995; Ibrahim, 2016; Shrestha & Farshad, 2009). The main causes of soil salinization in dry regions include irrigation (i.e., over-pumping), poor water drainage, and climate change (Shrivastava & Kumar, 2015). Therefore, areas of agricultural or arable lands will dwindle because of salinization (Wu et al., 2014b). Additionally, many countries are confronted with varying degrees of soil salinization. The Food and Agriculture Organization (FOA) has estimated that 397 million hectares

of the world's agricultural or non-agricultural lands have been affected by soil salinization (Al-Khaier, 2003; Dehni & Lounis, 2012; Elhag, 2016; Hu et al., 2019a; Ibrahim, 2016; Ibrahim & Koch, 2015). Thus, it is crucial to determine which lands are affected by soil salinization, evaluate soil salinity, and determine the root causes of salinization to help decision makers develop management plans for ensuring the sustainability of agricultural land. This must be prioritized globally because soil salinization has deleterious impacts on the soil quality and productivity and is ubiquitous in the arid and semiarid parts of the world (Farifteh et al., 2006; Ibrahim, 2016; Mehrjardi et al., 2008; Sanaeinejad et al., 2009).

Researchers have recently shown significant interest in evaluating and mapping soil salinity in many regions around the world, especially in arid and semiarid areas that are heavily affected by salinization. For soil salinity evaluation and mapping, data must be collected using traditional soil sampling and laboratory analysis methods. However, these methods are time-consuming and costly, which limits surveys to small areas (Farifteh et al., 2006; Ibrahim, 2016; Lhissou et al., 2014; Wu et al., 2014b). To overcome this limitation, several techniques have been developed for evaluating soil salinity. One such technique is based on Remote Sensing (RS), which has demonstrated considerable success in mapping and assessing soil salinity (Asfaw et al., 2018; Garcia et al., 2005; Wu et al., 2014b). Metternicht (1998), Metternicht and Zinck (2003), Eldeiry and Garcia (2010), and Furby et al. (2010) observed that meaningful results could be obtained by studying the spectral properties and radar backscatter of saline soils. Some researchers (e.g., Hardisky et al., 1983) have studied soil salinity based on moisture content using the normalized difference infrared index. Other researchers have assessed the relations between soil salinity and vegetation indices (Brunner et al., 2007; Garcia et al., 2005; Huete et al., 1997; Iqbal, 2011;

Steven et al., 1992; Wu et al., 2014b; Zhang et al., 2011a). Other studies have analyzed soil salinity using the thermal and short infrared wavelength bands (Goossens & Van Ranst, 1998; Ibrahim, 2016; Iqbal, 2011; Metternicht & Zinck, 2003; Wu et al., 2014b) to examine the relation between soil salinity and the Land Surface Temperature (LST). These studies used satellite imagery containing thermal bands such as a Moderate Resolution Imaging Spectroradiometer (MODIS), which provides useful information about the soil properties (Fallah Shamsi et al., 2013; Ibrahim & Abu-Mallouh, 2018; Majed et al., 2020). Recently, the multispectral data derived from sources, such as the System Pour I, Observation de la Terre (SPOT), IKONOS, Quick Bird, Indian Remote Sensing, and Landsat satellites, have been used to explore and map soil salinity. Several other indices, such as the salinity index (Khan et al., 2005) and the soil adjusted vegetation index (Huete, 1988), are also commonly employed to monitor soil salinity. However, Eldeiry and Garcia (2010) and Hu et al. (2014) recommended the combined use of the combination spectral response index and best band.

RS tools and data must be integrated with the field measurements of salinity to achieve soil salinity evaluation and monitoring. RS is an efficient tool for spatial analysis of soil salinity in arid and semiarid areas; therefore, it was aimed to estimate the soil salinity in Abu Dhabi using specific spectral indices combined with field measurements. The soil salinity mapping model developed in this study is based on the electrical conductivity of soil and shows a promising correlation, which can be further improved by considering the soil salinity–LST relation. This model is helpful to develop effective soil salinity forecasting strategies for sustainable development and land management.

3.2 Materials and Methods

3.2.1 Study Area

The study area is located in the western part of the United Arab Emirates (UAE) near the coast of Abu Dhabi (see Figure 1). The study area covers parts of the central and south-western areas of Abu Dhabi and lies between 24.44° and 23.46°N latitude and 52.59° and 54.49°E longitude.
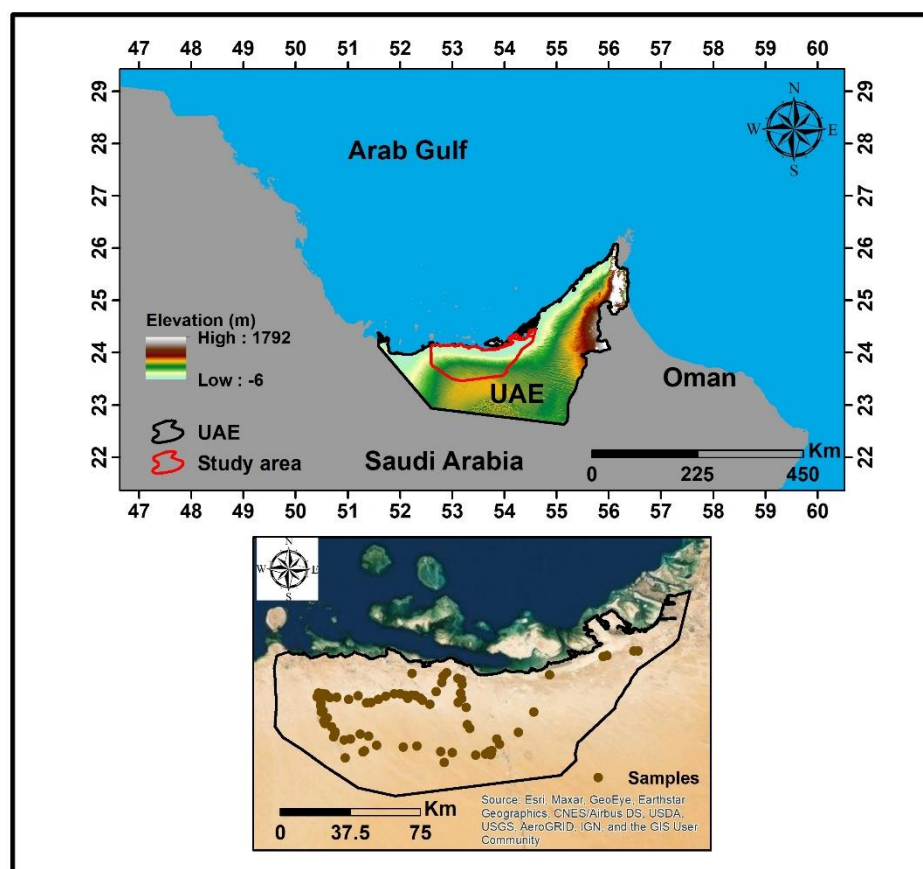
Figure 3.1: Locations of the study area and the sampling sites

The study area exhibits a hot arid climate with high temperatures through the night during summer. The mean minimum and maximum summer temperatures are 21.7ºC and 33ºC, respectively (Abuelgasim & Ammad, 2019; Farahat, 2016). In the zones away from the Sabkha area, mean temperatures can reach 43ºC in the summer

and 17ºC in winter (Abuelgasim & Ammad, 2017; Lokier et al., 2013). The mean annual rainfall is slightly less than 120 mm, which corresponds to extremely arid climatic conditions. This rainfall is 37% of the precipitation near the Strait of Hormuz, 40%–50% of that in the shallow depths of the UAE coastal areas, 60%–70% of that in lagoons and embayments, and 65% of that in the Arabian Gulf coastal lagoons (Abuelgasim & Ammad, 2017; Alsharhan & Kendall, 2003; Bathurst, 1972; Evans et al., 1969; Paul et al., 2016; Raafat, 2006).

The study area is categorized as one of the largest Sabkha surfaces, both coastal and inland, in the world. This region is dominated by the hot arid climate zone, as evidenced by the salt flats and marshes, which are categorized as the geological features of Sabkha commonly observed under arid and semiarid climatic conditions (Abuelgasim & Ammad, 2019; Evans et al., 1969).

Evaporation is considerably higher because of the extremely hot climatic conditions of the study area. This results in the deposition of large amounts of salts in the soil, increasing the percentage of insoluble salts beyond saturation. These factors and the associated soil salinization pose serious environmental threats to the soil environment in the Sabkha area. Soil degradation leads to decreased soil productivity, uneven dehydration of gypsum contributes to the development of cracks in the soil surface, and high concentrations of sulfate and carbonate salts lead to the corrosion of the steel pipes of water and oil distribution networks (Abuelgasim & Ammad, 2019; Youssef et al., 2012).

3.2.2 Methodology

The methods followed in this study can be broadly divided into three categories: (i) field measurements, (ii) image processing, and (iii) statistical analysis.

3.2.2.1 *In situ* and Laboratory Measurements

Samples of different types of soil were collected randomly from 80 sites in a desert area with dominant sand dunes. The samples covered different types of land and included inland Sabkha and saline soil areas. The samples were divided into two groups, i.e., soil samples collected from the areas in dune zones near major roads and those collected from the inland Sabkha and saline soil areas. This categorization of the soil samples allowed the assessment of the soil salinity and degradation index. Some samples from both groups were used in salinity estimation and model development, and the remaining samples were employed for model validation. The field work was conducted in November 2016, and sampling was performed during dry weather conditions, indicating the occurrence of no rainfall in the study area during sample collection.

The soil samples were analyzed in the laboratories of United Arab Emirates University. Following the standard soil analysis methods presented by Evans et al. (1969), the soil samples were air-dried at room temperature, fragmented by hand or using a geological hammer, and then ground. A 1:2 soil–water suspension was prepared by mixing the soil mass with a volume of deionized water equivalent to double the soil mass. An EC meter (ExStik EC 400) was used to measure the conductance of the soil suspension to indicate the amount of soluble salts in the soil. This EC meter measures conductivity in the ranges of 0–199.9 μS/cm, 200–1999 μS/cm, and 2.00–19.99 mS/cm. Soil samples with EC values higher than the EC meter's upper limit were further diluted to enable accurate EC measurements.

Following Kissel and Sonon (2008), soil salinity was classified into three classes in terms of soil quality and suitability for plant growth, as shown in Table 1. Previous research projects developed soil salinity scales (e.g., the soil quality

guideline) in terms of the sodium adsorption ratio and EC for unrestricted land use (Headley et al., 2007; Kissel & Sonon, 2008). The comparison of the soil EC values obtained in this study with the soil salinity scale found in the Soil Test Handbook for Georgia (Kissel & Sonon, 2008) indicates that most of the study samples are in the very high salinity level.

Table 3.1: Soil salinity classes. Modified from Kissel and Sonon (2008)

EC (dS/m)	Soil Salinity Class	Description
< 1	Low	- Plants may starve if the soil lacks organic matter - Satisfactory if the soil contains abundant organic matter
1 - 2	Medium	The satisfactory range for established plants
> 2.00	High	- Suitable for some types of plants and unsuitable for seedlings or cuttings - If EC increases to more than 2 dS/m, then the soil will be unsuitable for plant growth - Plants will be severely dwarfed, and the seedlings and rooted cuttings will frequently die.

3.2.2.2 Data Acquisition

The RS data for this research were downloaded from the United States Geological Survey Earth Explorer (https://earthexplorer.usgs.gov/). The data collected were the Landsat 8 Operational Land Imager (OLI) and day and night MODIS LST data (Aqua and Terra) MYD11A1 and MOD11A1, which were geometrically corrected and rectified to UTM zone 39. The images acquired on November 6, 2016 (path 161 and rows 43 and 44) were utilized to correspond with the field work. MODIS data with horizontal (h) and vertical (v) title number h22v06 were downloaded. The

data were then prepared and analyzed using the ERDAS IMAGINE 2014 software. The PCI Geomatica software was employed to perform atmospheric correction, and ArcGIS 10.5 software was used for image indexing and analysis and creating the database. ArcMap tools were used to compose the images and for soil salinity mapping. MODIS/Terra and Aqua satellite imagery were used to examine the correlation between *in situ* salinity measurements and LST values obtained from satellite imagery in the study area. The results were analyzed statistically using Microsoft Excel.

3.2.2.3 Image Analysis

Four spectral indices were utilized in this study to achieve the study objectives. These indices are NDVI, the Bare Soil Index (BSI), the spectral salinity index 1 (SSI1), and SI.

3.2.2.3.1 NDVI

NDVI represents the normalized ratio of near-infrared and red reflectance and has been used in many scientific studies related to environmental issues such as soil and vegetation degradation (Rouse et al., 1974). NDVI is calculated as follows:

$$\text{NDVI} = \frac{\lambda \text{NIR} - \lambda \text{Red}}{\lambda\,\text{NIR} + \lambda\,\text{Red}} \qquad (3.1)$$

where NIR is the near-infrared reflectance ($\lambda \approx 0.8\ \mu m$) and Red is the red-band reflectance ($\lambda \approx 0.64\ \mu m$). Variations in soil brightness can lead to noticeable variations in NDVI values (Carlson & Ripley, 1997).

3.2.2.3.2 BSI

BSI is the second index considered in this study. It combines the surface reflections of blue, red, green, and near-infrared radiation and is employed to detect soil variations from the Landsat 8 OLI and Thematic Mapper images. BSI was used to assess the condition of barren soil, which is helpful in determining the state of land degradation because of salinity. BSI also helps to determine the relation between soil salinity and plant growth, mainly in the coastal and inland Sabkha that covers most of the study area (Ibrahim et al., 2019). BSI is calculated as follows (Rikimaru et al., 2002):

$$\text{BSI} = \left[\frac{(\lambda\,\text{Red} + \lambda\,\text{Green}) - (\lambda\,\text{Red} + \lambda\,\text{Blue})}{(\lambda\,\text{NIR} + \lambda\,\text{Green}) + (\lambda\,\text{Red} + \lambda\,\text{Blue})} \times 100\right] + 100 \qquad (3.2)$$

3.2.2.3.3 SSI1

SSI1 was also employed in this study. It is one of the common indices used to estimate soil salinity in dry land and arid and semiarid areas, and it is sensitive to the soil salinity in arid and semiarid regions (Ibrahim et al., 2019). SSI1 is calculated as follows (Ibrahim et al., 2019):

$$\text{SSI1} = \sqrt{\text{Blue}} \times \text{SWIR2} \qquad (3.3)$$

where SWIR-2 is the shortwave infrared-2 reflectance ($\lambda \approx 2.2\ \mu m$) and Blue is the blue-band reflectance ($\lambda \approx 0.48\ \mu m$).

3.2.2.3.4 SI

SI is the salinity index derived from broadband satellite images that indicates the relation between the actual soil salinity and the variation in vegetation. Thus, many studies have evaluated soil salinity by referring to vegetation reflectance (Allbed et al.,

2014). This index is defined as the square root of the reflectance of blue radiation multiplied by the reflectance of the red radiation (Khan et al., 2001):

$$SI = \sqrt{Blue} \times Red \qquad (3.4)$$

where Blue and Red denote the reflectance in the blue and red light regions of the spectrum ($\lambda \approx 0.48$ µm and $\lambda \approx 0.64$ µm), respectively.

3.2.2.3.5 LST

Temperature was converted from Kelvin (K) to Celsius (°C) using the following equation. First, the unit was multiplied by an assigned scale factor of 0.02 to obtain the value in Kelvin, after which the resulting value was subtracted by 273.15 to convert K to °C.

$$LST\ (°C) = a \times DN - 273.15 \qquad (3.5)$$

where °C is the LST in Celsius and a is the scaling factor of the MODIS LST product (Wan et al., 2015).

3.3 Results and Discussions

Results of the laboratory analyses of soil samples indicated that although non-saline soils characterize certain parts of the study area, soils in the majority of the Sabkha area are highly saline (Table 3.1). The highly saline parts of Sabkha area are categorized as salt flats. Additionally, although the maximum EC value in the study area is 170.1 dS/m, most of the non-saline soil locations are located far from the Sabkha and have a minimum EC value of 0.09 dS/m. Statistical analyses were conducted on the five main study variables: EC, SI, SSI1, NDVI, and BSI (Table 3.2).

Table 3.2: Descriptive statistics for the five study variables (EC, SI, SSI1, NDVI, and BSI)

Parameter	EC (dS/m)	SI	SSI1	NDVI	BSI
Min.	0.09	0.06	0.10	0.00	0.6
Max.	170.10	0.18	0.26	0.10	0.12
Mean	15.67	0.08	0.21	0.07	0.08
Standard Deviation	32.66	0.03	0.03	0.02	0.03
Standard Error	3.65	0.00	0.00	0.00	0.00

NDVI and BSI show the strongest correlations with soil salinity, with coefficient of determination (R^2) values of 0.43 and 0.25, respectively (Table 3.3). Regression analysis demonstrates that the model predicting EC from NDVI and BSI has a prediction power of 80%, as indicated by an R^2 value of 0.80. Thus, only NDVI and BSI were used to generate the final salinity model for the study area. Results reveal that the probability (p) values were less than 0.05, indicating a statistically significant correlation between the RS data and field measurements. Thus, these data can be used to model the spatial distribution of soil salinity in the study area.

3.3.1 The Relation between Vegetation Indices and Soil Salinity

The soil analysis results show that the relation between NDVI and soil salinity is statistically significant ($R^2 = 0.43$, $p < 0.05$). This statistical significance indicates that the relation between NDVI and soil salinity is caused by one of them affecting the other and that there is less than 5% probability of rejecting the relation between NDVI and soil salinity. Table 3.3 and Figure 3.2 shows the regression model quantifying this relation:

$$Salinity = -1074.8 \times NDVI + 92.83 \qquad (3.6)$$

Table 3.3: Results of the analysis of correlation among the study variables

Variable	Soil Salinity	SI	SSI1	BSI	NDVI
Soil Salinity	1				
SI	0.21	1			
SSI1	0.21	0.26	1		
BSI	0.25	0.23	0.41	1	
NDVI	0.43	0.19	0.46	0.8	1
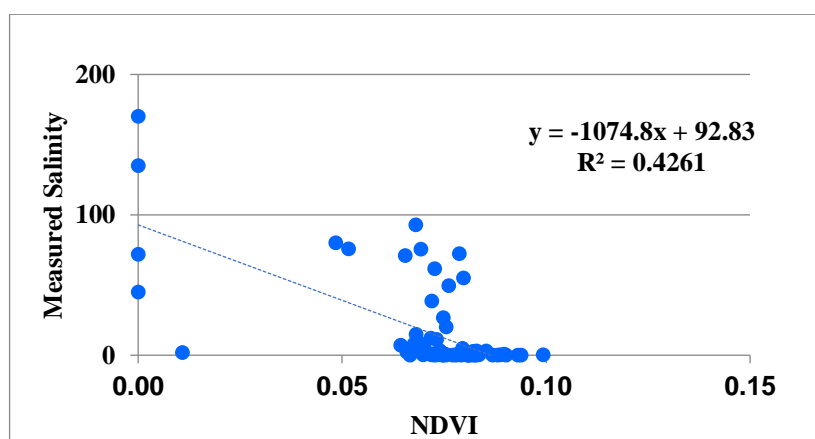
Figure 3.2: The relation between the measured soil salinity and NDVI

It is worth underlining that the relation between soil salinity and NDVI differs from site to site in the study area.

3.3.2 The Relation between the Vegetation Index and BSI

Figure 3.3 shows the relation between land degradation (expressed in terms of BSI) and vegetation cover (in terms of the NDVI). Results indicate a statistically significant relation between BSI and NDVI ($p < 0.05$), and the regression model that predicts BSI from NDVI has a moderate prediction power ($R^2 = 0.79$) This relation is obtained because NDVI and BSI use the red and NIR spectra in the equations. Additionally, BSI reflects the percentage of land degradation when considering a generally low rainfall; however, it does not indicate whether an area is extremely low

in vegetation, as estimated by NDVI. Low NDVI values are associated with extreme climatic conditions such as extremely low annual rainfall (≤120 mm/year) and high evaporation rates (2,000 mm/year). Furthermore, salinization has negative effects on plant roots, which passively affects plant growth.
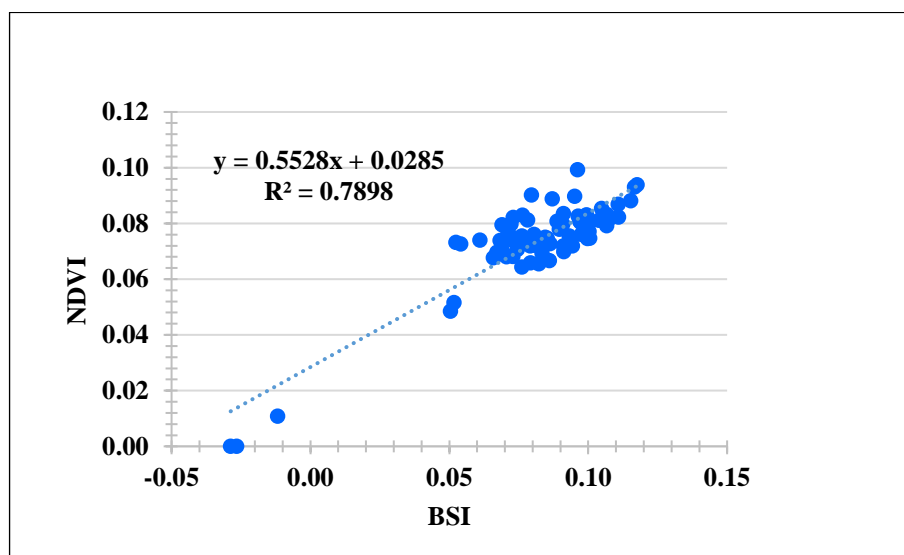
Figure 3.3: The relation between the NDVI and BSI

3.3.3 The Relation between Soil Salinity and BSI

The relation between the measured soil salinity and BSI to determine whether soil salinity leads to land degradation was investigated. Results (see Figure 3.4) revealed a statistically significant relation between soil salinity and BSI ($R^2 = 0.25$, p < 0.05), indicating strong evidence against there being no relation between soil salinity and BSI (Table 3.3). The relation level was different from expectations because the salinity in Sabkha soil can be attributed to the salty groundwater near the surface in that area based on Al-Mhaidib (2003). Thus, shallow water that can be attributed to droughts or very low rainfall can affect the BSI results. The linear regression model describing the relation between these variables can be expressed as follows:

$$\text{Salinity} = -567.74 \times \text{BSI} + 59.381 \qquad\qquad (3.7)$$

Results support that any increase in soil salinity will adversely affect the growth of vegetation, thereby decreasing the NDVI and increasing the BSI. In consideration of these results, the ArcGIS software was used to generate a digital soil salinity map based on the aforementioned regression models using the raster calculator. Regression models were used to estimate and model soil salinity for the study area.
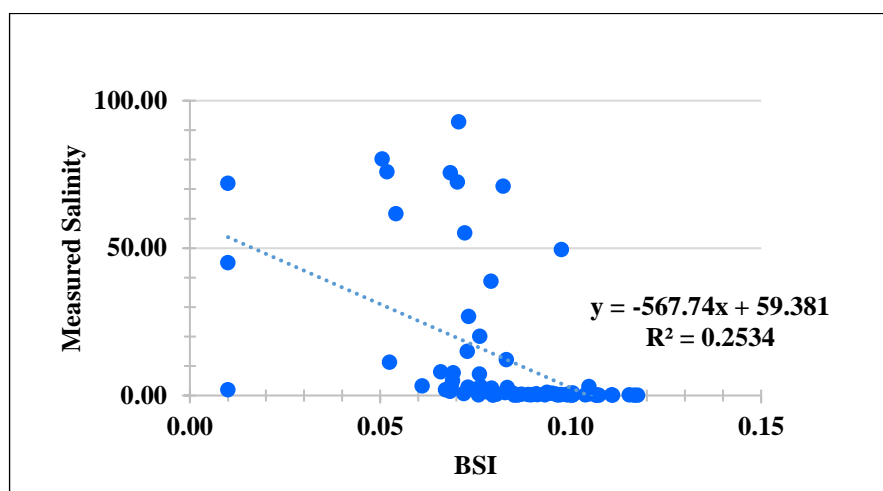
Figure 3.4: The relation between the measured soil salinity and BSI

To present an example of soil salinity mapping based on the soil salinity categories and show the geospatial distribution of soil salinity within the study area. The soil salinity levels were classified and mapped based on the soil salinity classification of Kissel and Sonon (2008). Figure 3.5 presents the predicted soil salinity map for the study area generated based on the NDVI–BSI regression model (Equation 3.8), which can be expressed as follows:

$$\text{Soil Salinity} = -284 \times \text{BSI} - 537 \times \text{NDVI} + 76 \qquad\qquad (3.8)$$
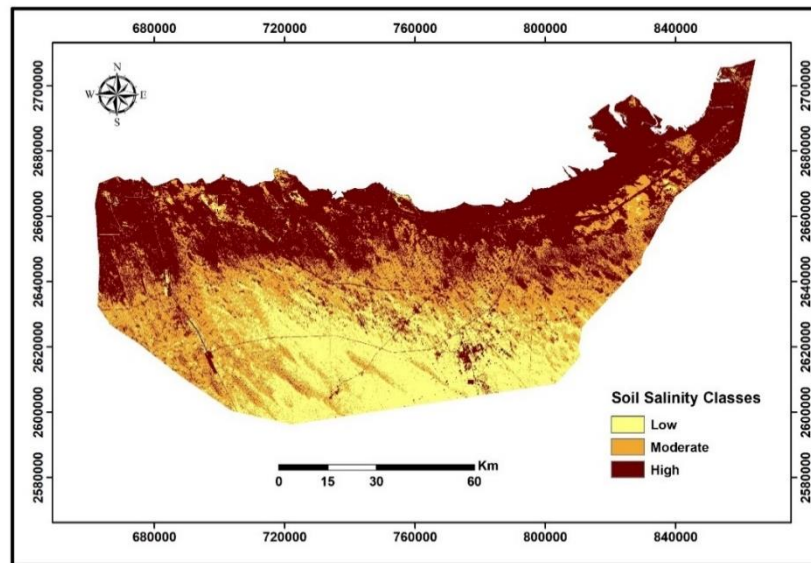
Figure 3.5: Predicted Digital Soil Salinity Map

BSI is sensitive to soil salinity and is thus regarded as a good model for mapping the high soil salinity levels of the Sabkha area. However, this index does not accurately predict low soil salinity levels. This can be attributed to the fact that there are types of soils, such as low salinity soils, that show no spectral response in the NIR–SWIR spectral range (Abuelgasim & Ammad, 2019).

The model obtained based on these indices have proved to be capable of mapping and accurately estimating soil salinity at different levels within the study area and has a prediction power of 36% ($R^2 = 0.36$). This model is based on NDVI and BSI, which are calculated using the surface reflectance of NIR radiation, making this a useful tool for monitoring soil salinity.

The study findings show that most saline soils are located in the inland Sabkha, which may be attributed to the salty groundwater near the surface in that area. Al-Mhaidib (2003) mentioned that the upward movement of water due to capillary action because of the increased continuous evaporation rate results in the increased salinity of Sabkha soils and salt deposition at the top surface of the Sabkha. Additionally, soil

salinity is generally higher in the northern part of the study area near the Arabian Gulf, which can be attributed to the deposition of carbonates by wind erosion of inland dunes due the northerly (Shamal) winds (Abuelgasim & Ammad, 2019). The non-saline soils are mostly located in the southern inland parts of the study area.

3.3.4 The Relation between Soil Salinity and LST

The MODIS LST data were analyzed against the *in situ* salinity data. However, some of the daily LST data were excluded from correlation analysis because the corresponding *in situ* salinity data were unavailable. Here, it was present the most meaningful and relevant results of the analyses. Results showed no statistically significant relation between LST/NDVI and LST/BSI, with correlations of $R^2 = 0.14$ and 0.05 for LST/BSI and LST/NDVI, respectively. $p < 0.05$ indicates that there is less than 5% probability to reject the relation between LST and various indices, where the effect of LST on vegetation and land degradation is different, as indicated by the correlation values. All the LST data were obtained on November 6, 2016 in correspondence with the *in situ* measurements. Four types of LST data were analyzed against the *in situ* salinity data, and the correlation of all the data varied from 0.22 to 0.56. The nighttime LST data exhibited a significant correlation of greater than 0.4, as shown in Table 3.4. Results indicate that there is a statistically significant physical process-driven correlation.

Table 3.4: LST with salinity *in-situ* correlation results

	Aqua_Day	Aqua_Night	Terra_Day	Terra_Night
r	0.22	0.56	0.25	0.43
R^2	0.05	0.32	0.06	0.16

The highest positive correlation for salinity can be observed with the nighttime Aqua LST data (0.56, Table 3.4), whereas the correlation with daytime LST is very

low. Figure 3.6 shows the LST correlation against *in situ* salinity from this highest correlation on November 6, 2016. Thus, the presented results demonstrate that the best correlation could be achieved using nighttime LST data. Considering the low spatial resolution of the MODIS data, the obtained results are statistically significant. Results show that salinity will increase more in areas with higher temperatures and that increased temperatures can lead to increased salinity. This assumption is supported by the statistical results, where a correlation of 56% and an R^2 of 0.32 were achieved. For future studies, the number of *in situ* measurements must be increased and satellite data with higher spatial resolution must be used.
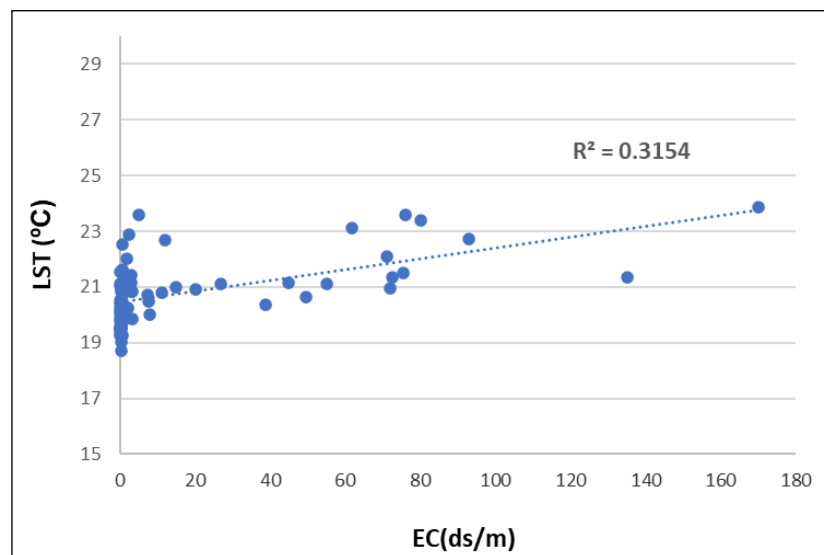
Figure 3.6: The relation between the nighttime Aqua LST and salinity correlation

3.3.5 Validation

A low correlation ($R^2 = 0.36$) was found between the measured EC values and the corresponding soil salinity estimates of the model when validating the developed model (see Figure 3.7). Nevertheless, the soil salinity model developed based on NDVI and BSI can be used for detection and prediction in case of salt-affected soils.
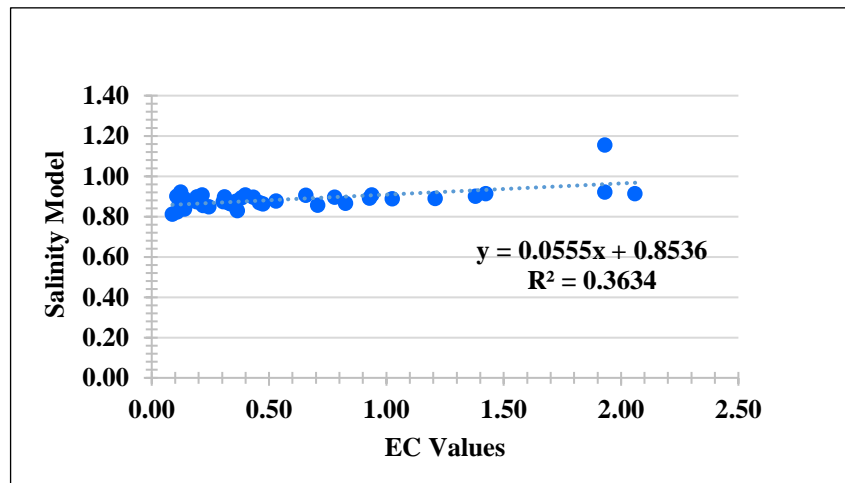
Figure 3.7: The relationship between the measured EC values and the soil salinity estimated from the model

Generally, the reflectance in the visible and NIR bands is beneficial for identifying saline and non-saline surfaces. Many studies (Akbar et al., 2011; Allbed et al., 2014; Asfaw et al., 2018; Ibrahim, 2016; Wu et al., 2014b) have shown that spectral indices (e.g., NDVI, SI, SSI1, and BSI) can be used to assess soil salinity and identify the salt-affected areas using imagery data. Thus, the model developed in this study is a promising tool for tracking soil salinity in the study area.

3.4 Conclusions

A model was developed for estimating and monitoring soil salinity in Abu Dhabi (UAE) using RS-based spectral indices and field measurements of soil salinity. Results support the possibility of modeling and mapping soil salinity using RS and GIS techniques. The integration of RS data and field measurements is a powerful tool for detecting salt-affected soils. The developed model could detect 77% of the salt-affected soils in the study area. Thus, this model can be confidently used to detect soil salinity in areas experiencing soil salinization. This model's ease of use and acceptable results make it a promising tool for predicting soil salinity. Although the imagery data

used in this study are of low resolution (30 m × 30 m), the model provides useful results reflecting the variations in soil salinity distribution. Accordingly, this study proves the model's ability to determine degrees of soil salinity in the region using RS data and GIS geospatial analysis for effective soil management and monitoring. In addition, this study showed a low correlation between soil salinity and nighttime LST, indicating that salinity will increase with the increasing temperature. However, the correlation between soil salinity and LST is an ongoing research topic. For future work, the researcher recommends a more detailed investigation on this topic by increasing the number of *in situ* measurements and using satellite data with higher spatial resolutions.

Chapter 4: Retrieval of Monthly Maximum and Minimum Air Temperature Using MODIS Aqua land Surface Temperature Data Over the United Arab Emirates (UAE)

Abstract

Spatially distributed air temperature (Ta) data are essential for environmental, climatological, and hydrological studies. Ta data are generally collected from meteorological stations that usually do not provide high spatial distribution patterns because of the sparse networks, particularly in arid regions. This problem can be overcome by using remotely sensed datasets at both regional and global scales. Currently, the Moderate Resolution Imaging Spectroradiometer Land Surface Temperature (MODIS LST) is the most acceptable dataset used to retrieve Ta. In this study, a combination of land-based temperature measurements and satellite datasets for estimating the Ta spatial distribution over the arid region of the United Arab Emirates (UAE) was used. Land-based Ta data from 11 weather stations distributed over the UAE covering a period from 2003 to 2019 were used together in this study with MODIS Aqua LST MYD11A2 Collection 6 product for both daytime (LSTd) and nighttime (LSTn) data. The results indicate a significant correlation between LST and Ta with regression coefficients $R^2 > 0.94/0.96$ and Root Mean Square Error (RMSE) about 1.75/0.97ºC of LSTd/T_{max} and LSTn/T_{min}, respectively. Large variability was observed between the daytime and nighttime mean temperature distribution in the studied period indicating the importance of the MODIS LST as a reliable proxy for Ta, where it is sparse in most of the cases. The production of these countrywide air temperature grids provides vital tools for the planning and management of environmental, social, and economic developments in the era of global climate change.

4.1 Introduction

Meteorological data such as air temperature (Ta) represent essential information for the economic development of the society for a variety of predictions ranging from precipitation trends, storms, heat waves, tourism, among other areas. Ta is important as it is commonly used in climate modelling, global change predictions, and modelling the exchange processes between the atmosphere, biosphere, and hydrosphere. Accurate determination of its spatial, temporal distribution and variability is vital for applications in the fields of hydrology, agriculture, environmental and ecological assessments, climate change, and related societal development (IPCC, 2017).

Ta data are usually collected by measurements at meteorological stations over both land and water surfaces. The measurements provide the benefit of high temporal resolution and accuracy. However, these data being point measurements do not reflect Ta spatial distribution and missing variability may not be observed (Otgonbayar et al., 2019). These limitations can bias Ta spatial distribution estimation, especially in the advanced spatial interpolations (Huang et al., 2015).

Moreover, changes in topography (elevation), and geometry of station location also affects the interpolation accuracy, specifically in elevated areas (Huang et al., 2015; Noi et al., 2016; Shah et al., 2012; Vancutsem et al., 2010; Zhu et al., 2013). A large part of these discrepancies from *in-situ* measurements of Ta has been overcome by using remotely sensed thermal infrared radiance that can be used to derive Land Surface Temperature (LST). The LST is described as a radiating temperature of the

land surface, which is observed by satellite sensors (Fadhil, 2011; Kloog et al., 2014). LST can only be derived from infrared (IR) channels for clear sky conditions as most of the clouds are opaque to IR energy, which is emitted from the surface. Although LST is not directly driven by solar radiance (Xu et al., 2012), it has a strong correlation with *Ta,* and it is considered one of the essential sources of data for *Ta* retrieval over a region or large area (Chen et al., 2016; Hereher, 2019; Hereher & El Kenawy, 2020; Jones et al., 2004; Phan et al., 2019).

The combination of meteorological stations data with the remotely sensed dataset assists the making of mesoscale maps for the distribution of LST by upscaling point data from meteorological stations (Huang et al., 2015; Shah et al., 2012). Remote sensing data offer a good solution to overcome the limitations of the interpolation methods. The capability to get both high temporal and spatial resolutions makes LST data an essential benefit of satellite observations over conventional climatic datasets (Kloog et al., 2014; Serra et al., 2020).

Many satellite sensors provide thermal data to retrieve LST, such as the Landsat TM/ETM+/TIRS, Advanced Spaceborne Thermal Emission and Reflection Radiometer (ASTER), Advanced Very High-Resolution Radiometer (AVHRR), and the Moderate Resolution Imaging Spectroradiometer (MODIS). Among these satellite data, Landsat and ASTER have a coarse temporal as well as spatial resolution of 16 days and 90-100 m, respectively (Phan et al., 2019). Thus, for *Ta* estimation, MODIS LST is considered a suitable source of data, and it is widely used in different applications due to its free availability, high thermal resolution, and can be obtained easily (Hereher, 2017a; Hereher & El Kenawy, 2020; Meyer et al., 2019; Zhou et al., 2017b).

To this moment, no research has been conducted to estimate *Ta* over the UAE. Therefore, the primary objectives of this study were to derive the components of two Ta (max and min) from LST using MODIS data over the UAE.

4.2 Data and Methods

4.2.1 The Study Area

The study area is the United Arab Emirates located between latitudes 22°- 26° N and longitudes 51°- 56° E (Figure 4.1). It has an approximate area of about 83,600 km^2. It is located on the Arabian Peninsula, one of the driest places on earth with an annual average precipitation of 100 mm that may reach up to 300 mm in the mountains and less than 50 mm in the desert (Murad & Aldahan, 2019). The desert occupies about 80% of the UAE land area. Although the annual average air temperature is around 28ºC, it is much warmer (up to 50ºC) in summer (Jun.–Aug.) and cools down to 10ºC in winter (Dec.– Feb.). The average number of sunny days is about 300, and dust storms occur within the range between 5 and 60 hours per year depending on location, with the highest events near to the desert areas and lowest along the mountains (Barbulescu & Nazzal, 2020).

4.2.2 Data

4.2.2.1 Topography Data

The study area is almost flat and homogeneous in the western and coastal parts, with most topographic undulations related to the sand dunes field. In the northeastern part of the UAE, there are mountain ranges with a maximum altitude up to 1,830 m. The spatial distribution of the terrain topography is shown on Figure 4.1, as estimated from the Shuttle Radar Topography Mission (SRTM).
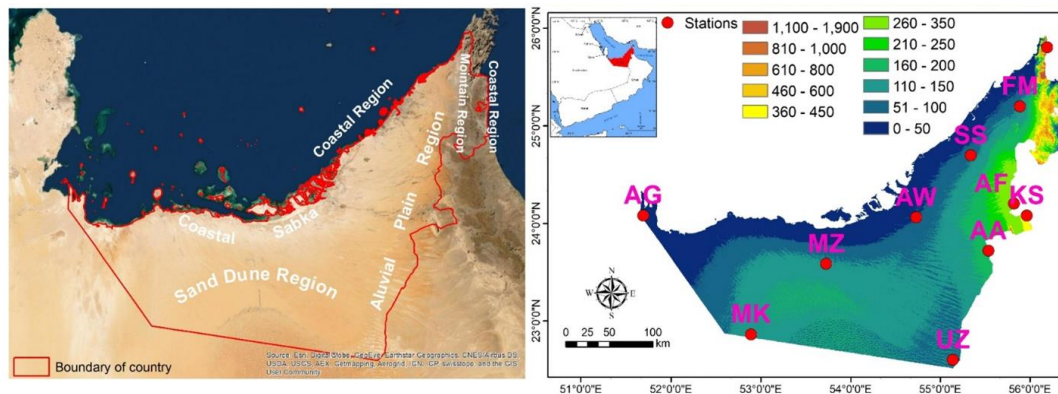
Figure 4.1: Topography, major geomorphic regions, and the spatial distribution of meteorological stations

4.2.2.2 Air Temperature Data

Monthly mean T_{max} and T_{min} (ºC) data for the period 2003 - 2019 were obtained from 11 automatic meteorological stations from different parts of the country collected by the National Center of Meteorology and Seismology (NCMS) (Figure 4.1). All the stations provided full records without gaps or missing values over the entire period. The distribution of the meteorological stations that were used here covers the mountainous area at an elevation of approximately 1,739 m (Jabal Jais station), one coastal area (Al Gheweifat station), and the remaining nine stations are dispersed in the desert and bare land. The available weather stations are mostly below an altitude of 450 m above sea level.

4.2.2.3 MODIS LST Data

The MODIS instrument is aboard the NASA Earth Observing System Aqua and Terra satellites. In December 1999, the Terra satellite was launched, while the Aqua was launched in May 2002. Worldwide coverage is given by their orbital parameters in 1-2 days, and provide LST four times daily, including daytime (LSTd) and nighttime (LSTn). At about 10:30 AM, Terra descends past the equator, and at

about 10:30 PM, it ascends past the equator. In comparison, Aqua passes the equator at about 1:30 AM and 1:30 PM in opposite directions. Every 24 hours, at the same time, both satellites pass above the same location on Earth (https://modis.gsfc.nasa.gov/data/).

There are two thermal infrared bands used to derive the MODIS LST, i.e. 31 (10.78–11.28 μm) and 32 (11.77–12.27 μm) using the split-window algorithm (Wan et al., 2002). The accuracy is 1K in most of the cases under the clear sky, as per the results of ground validation of these LST products. This level of accuracy can achieve requirements for the accuracy of most LST modelling applications (Wang et al., 2008). From mid-2002 (Aqua) and early 2000 (Terra), MODIS LST data has gained significant attention and is widely used for the estimation of Ta. It also has shown its suitability as a proxy for Ta in neighboring countries such as Egypt (El Kenawy et al., 2019a, 2019b; Hereher & El Kenawy, 2020), Iran (Janatian et al., 2017) and Oman (Hereher, 2019). These previous results serve as a verification of the precision of MODIS products, which reach the requirements of Ta estimation.

The LSTd and LSTn adopted here were extracted from the Aqua 8-day LST and Emissivity MODIS product Version-6. The LST product, such as MYD11A2, covers the time period 1st Jan. 2003 - 31st Dec. 2019. The Land Processes Distributed Active Archive Center of NASA (LP DAAC) provided all products in the two MODIS tiles of granules with horizontal (h) and vertical (v) title numbers h22v06 and h23v06 (https://lpdaac.usgs.gov/). Brightness value (16-bit) is represented by each image, in Hierarchical Data Format (HDF), and at a Sinusoidal Projection, in relation to the LST in Kelvin. The images are 1 km spatial resolution and contain layers of LSTd and LSTn.

Although daily data of MODIS Aqua for the product MYD11A1 is available from Jan. 2003, the composite product MYD11A2 was used here. The reason for selecting 8-day data is better data coverage (i.e., no gaps in data except persistent cloud coverage). In other words, due to correction of cloud contamination, the available data is more continuous, and therefore, the quantity of available data points for comparison for 8-day average is remarkably less than the available daily average dataset (Hengl et al., 2012; Shah et al., 2013; Singh et al., 2019). The accuracy of this product (MYD11A2), according to NASA's Goddard Space Flight Center, was reported better when compared to 1 Kelvin in clear sky conditions (https://modis-land.gsfc.nasa.gov/). Thus, for the entire UAE, a set of LST 8-day composite products (MYD11A2) was acquired.

MODIS LST data Version-6 (or collection-6) was used because of significant changes, and improvement that were made for this version (Wan, 2014). In these improvements, the most critical changes of version-6 in comparison to the previous version is removing cloud contaminated LST pixels. The accuracy of the LST version-6 product was reported to be two times better than version-5 (Duan et al., 2018). According to Vancutsem et al., (2010), when selecting the data for a specific area, it is essential to consider the time of overpass. Thus, MODIS Aqua data was selected for the UAE as this sensor overpasses at 1.30 PM and 1.30 AM, which is closest to T_{max} and T_{min} measurement time, so the LSTd and LSTn from the satellite measurements could be estimated and compared with the ground weather station recorded T_{max} and T_{min}.

4.2.3 Methods

4.2.3.1 Pre-processing MODIS LST Data

At weather stations, many steps were followed to retrieve the data of LST under clear sky conditions. A total of 1564 MODIS images (MYD11A2, h22v06, and h23v06, Version-6) were collected. The HDF images were projected to WGS1984 UTM Zone 40N, for the study period, over the UAE, using the nearest neighbor resampling method. The corresponding layers (LSTd and LSTn) were extracted in TIF format. After that, a mosaic of two tiles was created, and the images were clipped using the boundary polygon, which defines the study area. Finally, LST data were aggregated to a monthly period by averaging the 8-day composite data to obtain monthly average LSTd and LSTn, to provide direct comparison to the maximum and minimum monthly average that were used to represent *Ta* data.

Using batch processing of extract multi-value, MODIS LST data for the pixels were extracted from TIF format MODIS images in which the weather stations are located to points in the ArcGIS program. Using the following equation, all these LST data (DN values) were converted to Celsius temperature:

$$\text{LST (}^{\circ}\text{C)} = a * \text{DN} - 273.15 \qquad\qquad (4.1)$$

where ${}^{\circ}$C is Celsius LST, and *a* is scaling factor (0.02) of MODIS LST product, which converts the values of scientific data sets into the real values of LST (Kelvin degree) (Wan et al., 2015).

Next, removing outlier data was performed: if clouds are present on a location (pixel), then MODIS LST products are unavailable for that location (Wan, 2008); however, some pixels which are slightly covered by clouds are not removed as the covering is minimal, and the cloud-removing mask algorithm cannot detect those (Noi

et al., 2017). Hence, all unrealistic values of LST data, which have values higher than 100ºC or less than −50ºC or any value beyond the valid range, were marked as no data and ignored in the procedure to provide a seamless dataset. Consequently, only clear, reliable pixels, and good quality data were used according to the Quality Assessment (QA) layer. All images for each month were placed together to make a single file for each daytime and nighttime. The monthly average for LSTd and LSTn was determined using the Cell Statistics model for all the images between 2003 – 2019. Finally, the Extract Multi Value model was used to derive LSTd and LSTn from a single pixel where weather stations are located and those values were converted to Excel Spreadsheets before matching them with the corresponding T_{max} and T_{min}, derived from eleven stations. For the processing, analyzing, displaying, and quality control of the MODIS data, ESRI ArcGIS™ 10.4 software was used.

4.2.3.2 Estimation of Air Temperature Using MODIS LST Data

Numerous methods have been developed and applied for *Ta* estimation from MODIS LST data. Benali et al., (2012) and Noi et al., (2016) point out there are three popular methods: statistical, temperature-vegetation index (TVX), and energy-balance modelling. Energy-balance approaches, the sum of incoming anthropogenic heat fluxes and net radiation, are considered similar to the sum of the surface's sensible and latent heat fluxes. Energy-balance approaches, however, require many parameters, which are mostly not directly provided by remote sensing. This is the main disadvantage of energy-balance methods (Benali et al., 2012; Liu et al., 2019; Mostovoy et al., 2006).

On the other hand, only satellite data is required in the TVX and the statistical method, which is easily accessible and is ordinarily available with thermal data

(Misslin et al., 2018). One drawback to the TVX method is that performance depends upon the negative correlation among the normalized difference vegetation index (NDVI) and LST, and there is a high variation in NDVI with different satellite sensors. However, this method is not satisfying in some cases because of the supposition that it frequently does not fit to the effect of the reality and seasonality, scarce of vegetation cover throughout the arid environment, soil moisture, or land cover type (Janatian et al., 2017; Stisen et al., 2007; Yang et al., 2017b). Therefore, the statistical method is a suitable and straightforward method, which does not present the same limitations.

There is a simple statistical linear regression between Ta and LST (Hereher, 2019; Hereher & El Kenawy, 2020; Mostovoy et al., 2006; Vogt et al., 1997) and also advanced approaches in which more than one independent variable are used (Benali et al., 2012; Noi et al., 2016; Vancutsem et al., 2010; Xu et al., 2012; Zhang et al., 2011b). The main advantages of the linear regression method is that the regression against station data minimizes systematic regional errors in data of the satellite, they normally provide accurate Ta estimation within the spatial and temporal frame they were obtained, and thy are easier to operate. Thus, simple linear regression is the most intuitive and widely used Ta estimation method (Janatian et al., 2017; Stisen et al., 2007). However, the statistical methods normally perform well in the spatial and temporal domains, they still require large amounts of data to train the algorithms, especially for the advanced approaches, and have restricted generalization (Stisen et al., 2007).

The criteria of combining data retrieved from satellite and meteorological stations for the same date comprise a one-to-one relationship, linking monthly LSTd and LSTn from satellite data with monthly data obtained from a station (T_{max} and T_{min}). Therefore, for each meteorological station, the LST values (LSTd and LSTn) of the 1

km^2 pixel are extracted, which are superimposed on the station. This process is done for all the existing images data of the study period. The LSTd images values are linked with T$_{max}$, and the LSTn images values are linked with T$_{min}$. Then the relationship of linear regression is estimated, and for each month, the coefficient of correlation between the monthly LSTd in the satellite image was determined with the T$_{max}$ of each weather station of the corresponding month. In the same way, the correlation between monthly T$_{min}$ from the weather stations and monthly LSTn from the satellite data was determined.

The regression equation was generated for the estimation of monthly air temperature maximum (Ted) and minimum (Ten) from data of LSTd and LSTn for the whole region. The annual daytime, nighttime, and diurnal variation temperature maps were also estimated. The following simple linear regression model was constructed to estimate the Ted and Ten from the LST data:

$$\text{Ted} = a \text{ LSTd} + b \tag{4.2}$$

$$\text{Ten} = a \text{ LSTn} + b \tag{4.3}$$

where a and b are coefficients of regression, which are estimated using ordinary least-squares regression. Ted and Ten are the estimated monthly average maximum and minimum air temperature, respectively. The LSTd and LSTn derived from the data of Aqua MODIS can be used as independent variables (x), and Ta (T$_{max}$ and T$_{min}$) is a dependent variable (y). In previous studies, to estimate air temperatures from LST, linear regression was successfully applied (Hereher, 2019; Hereher & El Kenawy, 2020; Huang et al., 2015; Kloog et al., 2014; Mostovoy et al., 2006). By applying the correlation between the day and night LST data readings versus all records from the 11 stations, the regression model for extracting maximum and

minimum air temperatures was determined. Two popular criteria were used to assess the performance of the regression model: the determination coefficient (R^2) that was calculated from the Ta values and LST data from linear regression analysis, and the Root Mean Square Error (RMSE). Calculation of these statistical factors was performed using Excel Microsoft.

4.3 Results and Discussions

As shown in Figure 4.2, a strong linear correlation exists between LST of satellite images and Ta data of meteorological stations in the study area, for both daytime and nighttime LST. The determination coefficient (R^2) for LSTd and T_{max} is 0.94, and 0.96 for the LSTn and T_{min} association. The determination coefficient is calculated for the 2003-2019 dataset. For estimation of maximum (Ted) and minimum (Ten) air temperature from the data of MODIS LST, the previous Equations 4.2 and 4.3 were used as the following:

$$Ted = 0.9218 \ LSTd \ \text{-}7.8667$$

(4.4)

$$Ten = 0.9372 \ LSTn + 0.215$$

(4.5)

Figure 4.3 shows the scatterplot diagram of the association between the LSTd and T_{max} and LSTn and T_{min} for the individual studied stations. The coefficients of determination between LSTd and T_{max} were very high. The coefficient value between LSTd and T_{max} ranges from 0.943 - 0.957, while the LSTn and T_{min} correlation were slightly higher at all stations, ranging from 0.963 - 0.985.
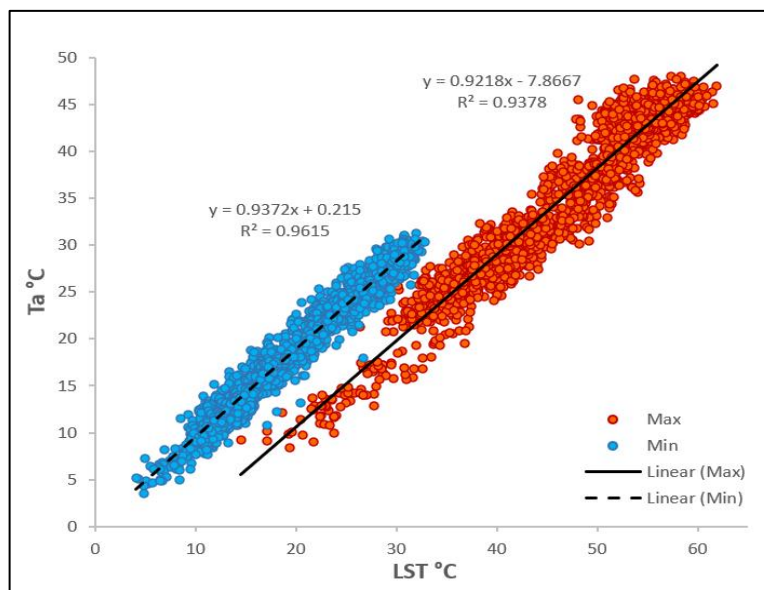
Figure 4.2: The regression correlation between LSTd and T$_{max}$ (red) and LSTn and T$_{min}$ (blue) for the period 2003-2019 of all stations
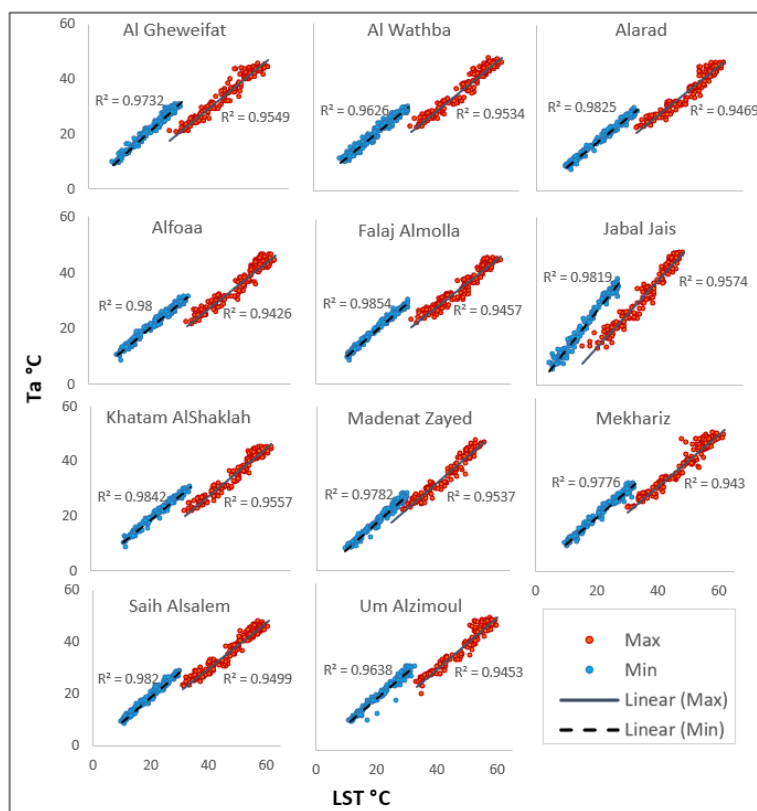
Figure 4.3: Scatterplots diagram showing the association between LSTd and T$_{max}$ (red) and LSTn and T$_{min}$ (blue) for all stations used in this study. The R^2 value is presented to show the sign of association and the magnitude, (Note the high value of R^2)

From Figures 4.2 and 4.3, a strong linear correlation between LST and Ta was observed. Despite the strong LST and Ta correlation, their values differ partially. At all stations, the LST and Ta relationship is slightly better defined by the linear regression during the night than the day. The LSTd is generally higher than T_{max}, whereas LSTn is slightly lower and quite close to the T_{min}. In other words, during the study period, the difference (LSTd-T_{max}) is higher than (LSTn-T_{min}) in all stations. These differences between Ta and LST increased in the summer season (Jun. to Aug.), in which the daytime is hotter and longer, as shown in Figure 4.4A. This trend has also been observed in many other studies, e.g. (Hereher, 2019; Hereher & El Kenawy, 2020; Huang et al., 2015; Zhu et al., 2013). Figure 4.4 shows that Ta and LST have seasonal cycles that are similar and correlated due to the energy exchange between Ta and LST that depends on seasonal variation of incoming solar irradiance. This feature relates to the stable stratification of the air parcel due to the radiative cooling at the surface and weakening of turbulence generated by surface friction during the nighttime (Lin et al., 2016). The Earth's surface almost acts as a homogeneous and isothermal surface. Results (Figure 4.4) show more complex interactions between Ta and LST during the daytime due to the more turbulent surface and weather conditions that are affected by direct solar illumination and therefore produce a slightly lower model fit (Kloog et al., 2014; Vancutsem et al., 2010). The increase in temperature and concentration of thermal energy at the surface during daytime as the ground absorbs solar radiation causes a partial decoupling of the day LST and Ta (Lin et al., 2016). This feature makes the LST of the daytime hotter as compared to Ta (Figure 4.4A). Also, due to the sunlight and shade effects in pixels during the daytime, a more significant angular anisotropy effect is expected for LST of daytime as compared to

the LST of nighttime, which similarly explains the slightly lower model fit (Benali et al., 2012; Zheng et al., 2013).

Furthermore, atmospheric water vapor is also a significant component that traps hot land surface long-wave radiations (Zhang et al., 2011b). In the study area of this study, the concentration of water vapor in summer is more like other trace greenhouse gases. Water vapor also has a warming effect on both air and land surface, however, in terms of radiative forcing, the warming effect magnitude of the greenhouse gases is different for the land surface and air (Zhang et al., 2011b). This additionally explains why the best performance is at nighttime with a minimum RMSE value of 1.49ºC, whereas, at daytime, the difference between LSTd and T_{max} is significant with RMSE of about 10.37ºC. Nevertheless, after applying the linear regression method, a significant reduction in statistical error was observed, with 1.75ºC at daytime and 0.97ºC at nighttime in all the stations. Figure 4.4B and 4.5 support the utilization of the linear regression method, showing that the estimated air temperature (Ted and Ten) nearly matches the measured air temperature (T_{max} and T_{min}).
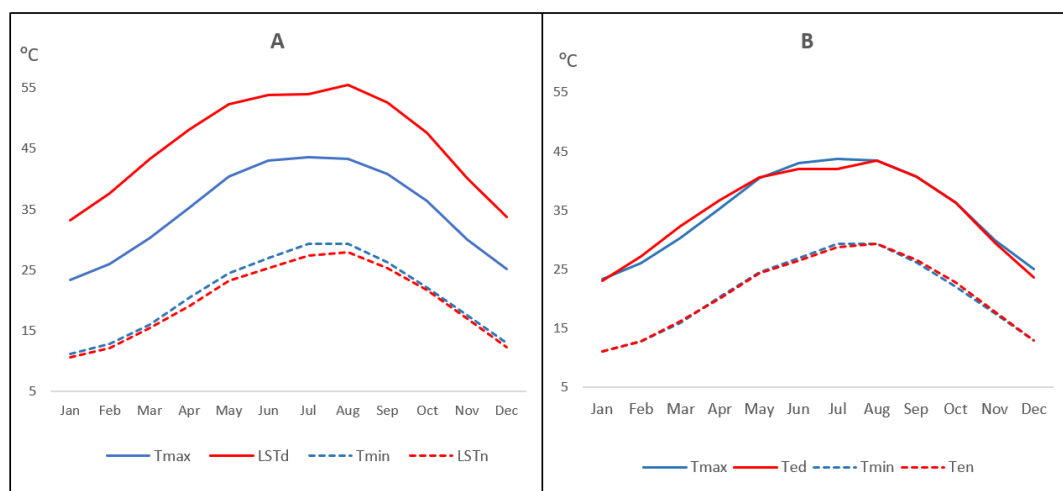
Figure 4.4: The annual cycle of nighttime and daytime temperatures. Calculated from weather stations (blue) and Aqua LST data (red), (A) before applying the linear regression method; and (B) after applying the linear regression method
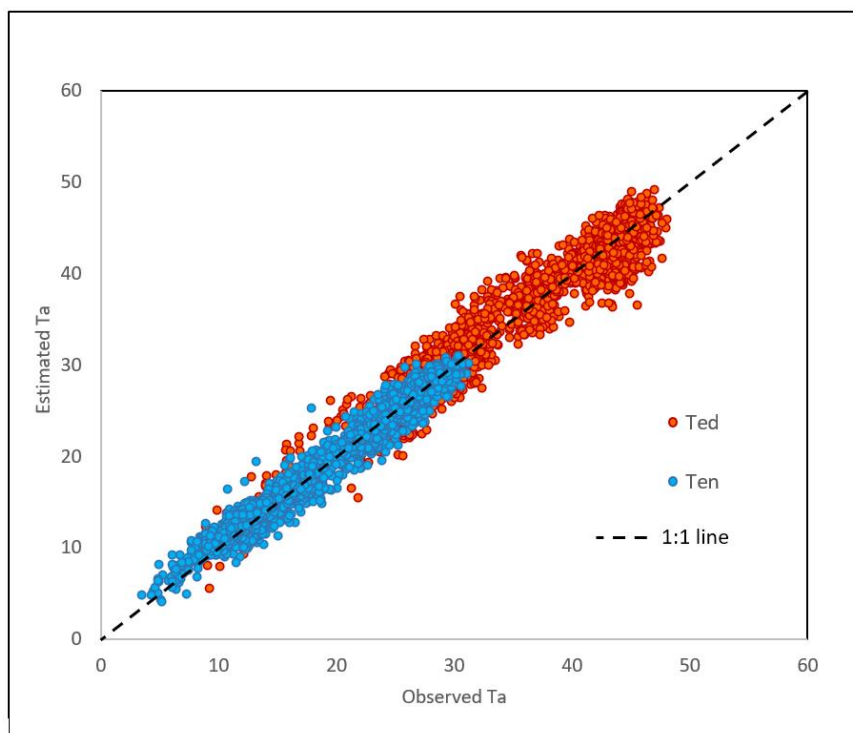
Figure 4.5: A scatter plot for stations' measured Ta (T$_{max}$ and T$_{min}$) and estimated air temperate (Ted and Ten)

The high statistical confidence of the liner regression between data from satellite images and observed Ta is discussed here. Therefore, by substituting the LSTd and LSTn values, they can be used to derive unknown T$_{max}$ and T$_{min}$ of any area, respectively. Accordingly, and applying Equations 4.4 and 4.5, the UAE's derived daytime and nighttime air temperatures monthly average (Ted and Ten, respectively) are shown in Figures 4.6 and 4.7. The average annual daytime and nighttime max and min air temperatures and the Diurnal Temperature Range (DTR) are shown in Figure 4.8.

The UAE's estimated average monthly maximum air temperatures (Ted) during the entire study period (2003-2019) indicate spatial variation in daytime air

temperature where the interior is hotter than the coastal and mountain areas (Figure 4.6). Furthermore, there are four major zones of Ted variations that maintain positions that is partly related to seasonal changes. A winter season is marked by the December to February with temperature zoning gradually decreasing from the inland towards the coasts. During March to May (spring season), the hotter inner land Ted zone expands and dominates the distribution pattern. This trend of expansion continues in the summer months (June-August and even September), leaving only the months of October and November months to initiate cooling and then a return to the winter season pattern in December (Figure 4.6). The Ted variability of the different zones in the different seasons range from > 45ºC for the hottest zone to as low as 10ºC in the coldest zone (Figure 4.6). The distribution pattern of these seasonal zones is rather different for the Ten, where a rather homogenous zone for inner land occurs during the winter season and partly extends into March (Figure 4.7). This pattern is decoupled into two major zones in April to June with a variable zonation pattern and returns to one major inner land zone from July to November. The extent of change in Ten varies from > 30ºC to < 8ºC. In areas with high altitude (more than 1000 m) such as Jabal Jis, the average air temperature is generally below 10ºC and occasionally may reach 0ºC or less.

The general distribution of air temperatures in the UAE during the winter season nighttime (Ten) is 10-15ºC in most areas, while it is at 25-30ºC in the summer season (Figure 4.7). In all seasons other than the summer months, the air temperatures are moderate during nighttime (< 25ºC). There is a relatively low-temperature zone in the interior desert with temperatures of 25-30ºC in summer and 10-15ºC in winter. The air temperature during daytime and nighttime has the same spatial patterns across the UAE. Namely, during the daytime, the air temperature increases moving further away

from the north and northwest and along the coastline to the south and southeast where the bar desert receives more solar radiation, which heats the ambient air. Air temperature in towns is higher than the surrounding region; this process is known as the Urban Heat Island (UHI), and at daytime, the inverse occurs, so it is called the Urban Cool Island (UCI), which may be essential for future research in the region.

To explore the difference between Ted and Ten patterns, the Diurnal Temperature Range (DTR) was used, which is an essential element for reflecting thermal environment analysis (Figure 4.8). The results reveal the persistence of four major Ted zones with temperature trends increasing from the coastal and mountain areas towards the inner land with a temperature span between 19 and 40ºC. Despite the fine temperature zonation given in Figure 4.8, the zonation can be generally grouped into two zones of 34-40ºC inner land zone and 19-34ºC coastal and mountain zone. The Ten mean annual zonation is characterized by a major inner land zone with temperature below 22ºC and a costal and mountain zone with a temperature between 23 and 27ºC. The hotter Ted in mountain and coastal zones in comparison to Ten is due to the proximity to the sea and the higher elevations that leads to a temperate air temperature environment.

DTR is an essential element of the climate system and was used for urban thermal environment analysis, for example, extensive heat waves, heat-related health issues, landscaping and recreation, and engineering of heat transfer efficiency in buildings and roads (Chen et al., 2020; Duan et al., 2014; Wang et al., 2019a; Yang et al., 2020). The pattern of DTR closely resembles the pattern of Ted, where the mountains and coastal zones indicate cooler temperatures than the inner land zones. The span of the DTR is between about 19ºC to < 1ºC, with most of the areas with temperature below 11ºC occurring in the mountain and coastal zones. It is important

to mention that most of the large cities, e.g. Dubai, Abu Dhabi, and Sharjah, in the UAE, are also located along the coastal zone. The relatively small DTR along the coastal zones is likely the temperate thermal environment that is modulated by proximity to the sea as vegetation cover is rather scarce in the UAE. The relatively large DTR in the inner land (mainly covered by sand dunes) is that the ambient air warms slower, and the land surface warms faster in the day, and similarly, the surface cools faster in the night. Therefore, the desert reveals higher diurnal variation air temperature than the mountains and coastal regions (Figure 4.8).

The mean annual Ted and Ten in the studied period (2003-2019) reveals rather small variations with the Ted around 35ºC and Ten around 20ºC (Figure 4.9). There is, however, a slight increase in the trends from 2003 to 2019, with about 0.31ºC and 0.78ºC per decade, for the Ted and Ten, respectively. This temperature increase may not be uniform all over the UAE, as also evidenced by the spatial distribution patterns. The projection of these data for future predictions of climate change, and assuming constant decadal values, indicates that there will be a more rapid increase in the nighttime temperature compared to the daytime. On average, there will be about a 1 - 2ºC increase in the mean annual air temperature by the end of 2030, which is comparable to the estimate made by Murad and Aldahan (2019) for the period 1972-2020.
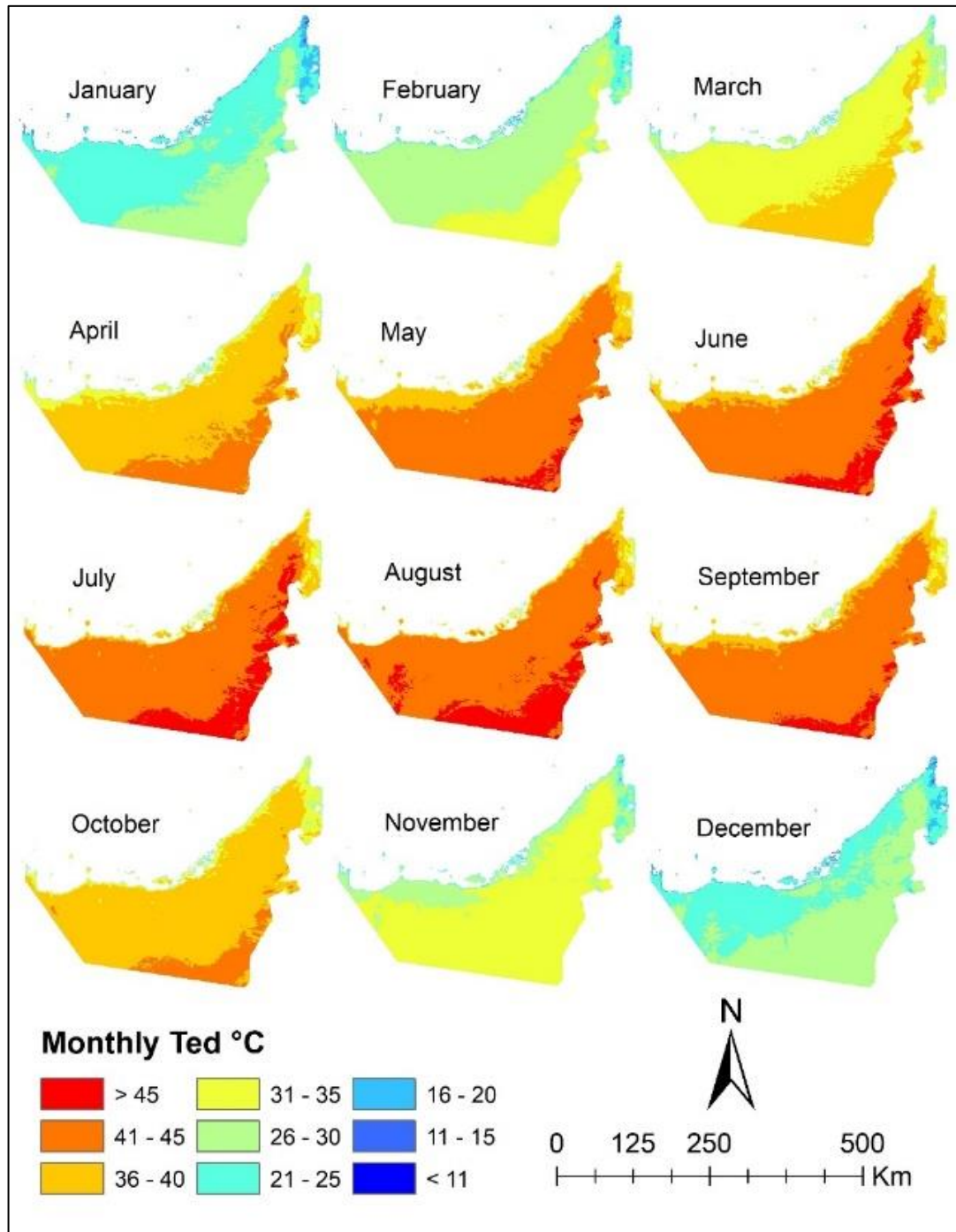
Figure 4.6: Spatial distribution of average monthly maximum air temperature (Ted) for UAE over the period 2003-2019
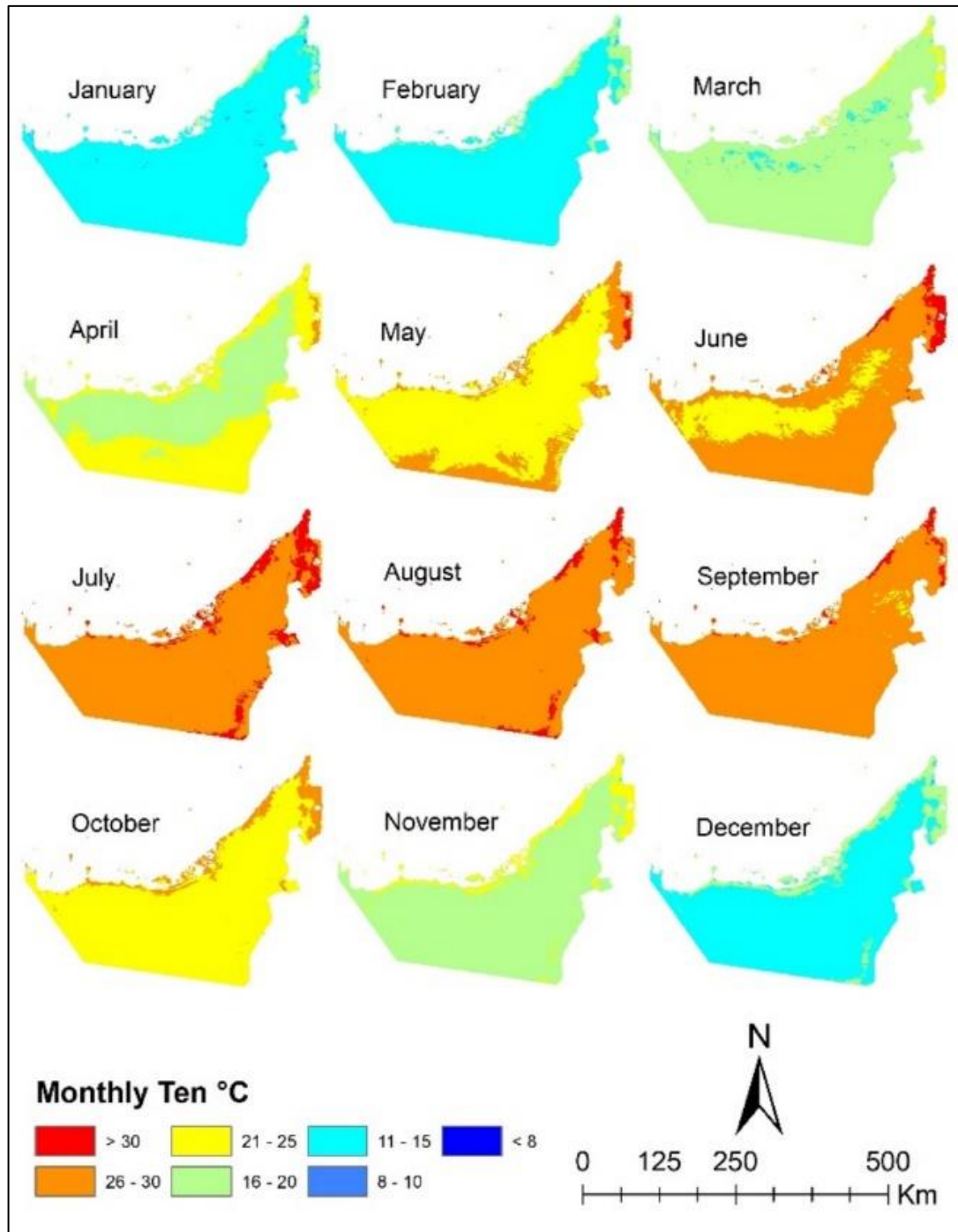
Figure 4.7: Spatial distribution of average monthly minimum air temperature (Ten) for the UAE over the period 2003-2019
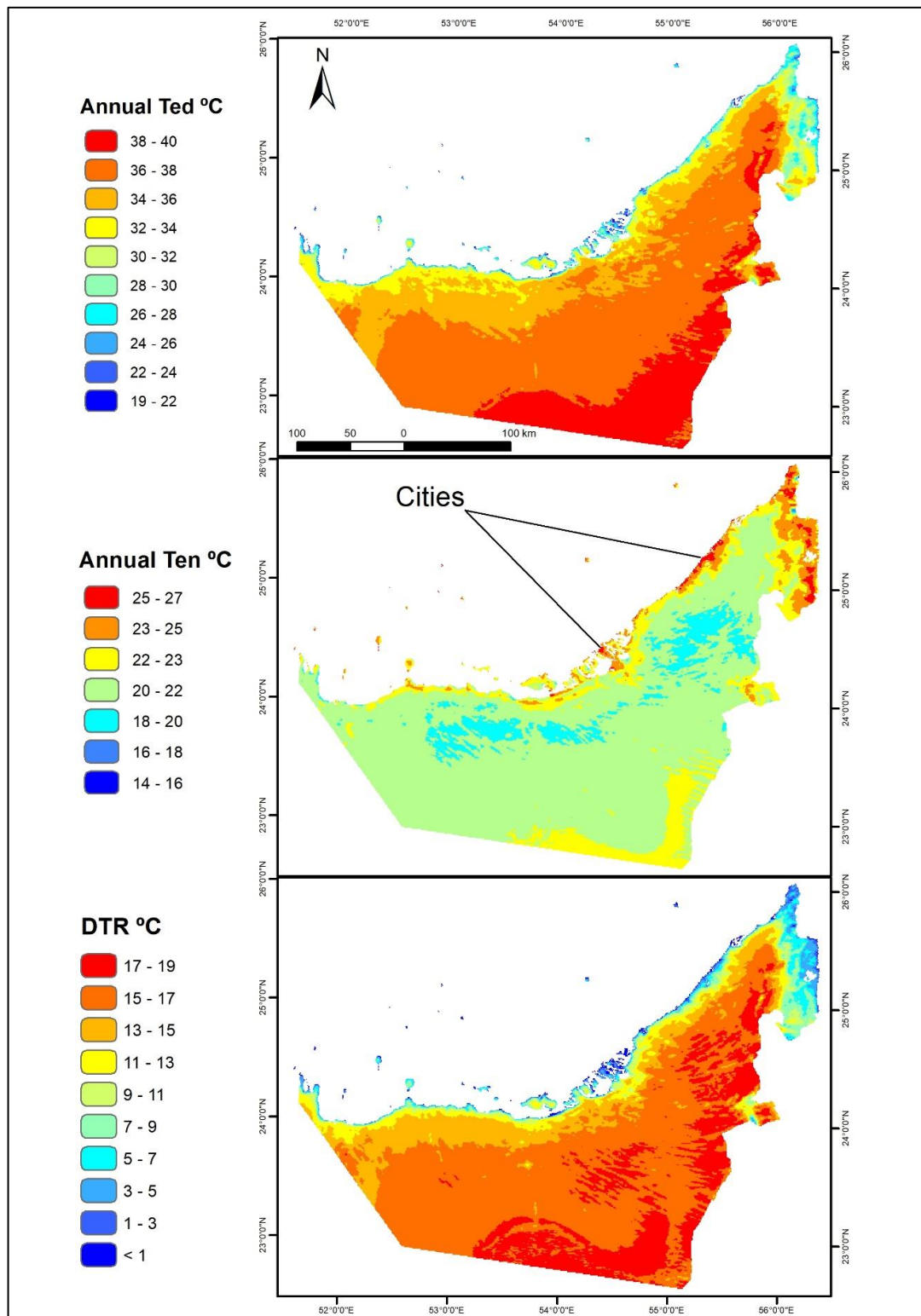
Figure 4.8: The annual mean maximum (Ted), minimum (Ten), and Diurnal Temperature Range (DTR) of air temperature of the UAE for the period 2003-2019
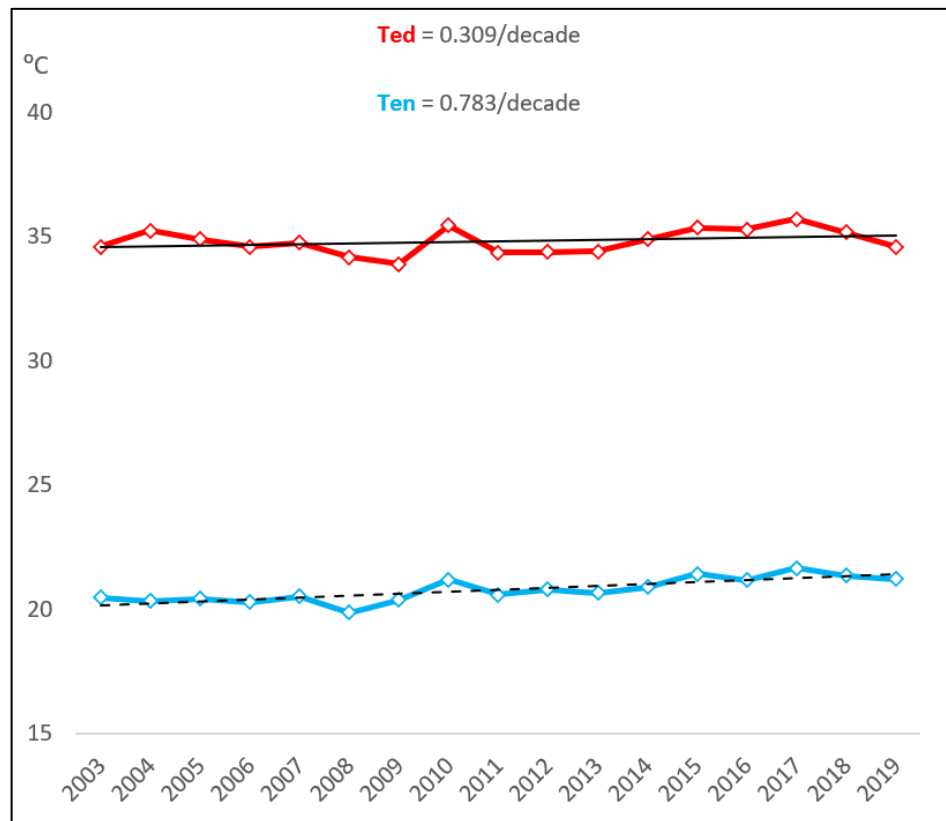
Figure 4.9: The mean annual (Ted, red line) and (Ten, blue line). For time series of the 11 weather stations used here in the period 2003–2019

4.4 Conclusions

This paper, for the first time, presented the estimation of monthly average maximum and minimum air temperature (Ted and Ten) over the UAE using Aqua MODIS LST data (LSTd and LSTn) and measured air temperature (T_{max} and T_{min}) observations from 11 weather stations from 2003-2019 by employing the linear regression method. The significant findings of this study show a strong correlation between these two datasets ($R^2 > 0.94$) and a high accuracy achieved in the linear regression with minimal errors (RMSE < 2°C), which implies that the linear regression method provided a reasonable monthly air temperature maximum and minimum. Based on this result, MODIS Aqua LST products have been shown to be a reliable

source for Ted and Ten. The detailed 1 km^2 air temperature products (monthly air temperature maximum, minimum) as given by the linear regression can itself act as a meteorological station with confident and provide accurate records where each pixel represents the associated temperature.

Therefore, a remotely sensed dataset could be an alternative and surrogate to the ground meteorological stations, which then provide data with high resolution and extensive geographical coverage. For example, some areas in the UAE do not have any meteorological stations, however, this present investigation efficiently determined these locations' air temperature in a rigorous fashion. Specifically, in the Al Khazna area, which is about 45 km east of Al Wathbah (AW) ground meteorological station, the estimated maximum and minimum temperature for May was 41.7ºC and 23.5ºC, while the AW station records were 41.8ºC and 22.7ºC for the maximum and minimum air temperature in May, respectively.

This study is instrumental in the UAE or other neighbouring countries because the results have numerous applications in the fields of hydrological, agriculture, environmental, ecological, climate change, economic, and societal growth. As an example, for the construction of new urban communities and the latest reclamation projects in UAE's desert area, the selection of low diurnal temperature variation should be considered because it directly affects the quality of life and economic factors pertaining to living in these regions. Furthermore, time-series data can provide the potential for evaluation of anthropogenic activities' effect on climate change (such as urbanization, changes in land-use), at both the local and regional climate scale.

The limitation of the MODIS LST products in *Ta* estimation is that it works appropriately in clear-sky conditions as it retrieved data by using thermal infrared data.

Moreover, the data of LST from MODIS starts from March 2000, restricting the prediction of *Ta* before that.

In future studies, specifically conducted on large areas with more varied and more complex land surface characteristics, other auxiliary variables should be considered that can reflect land surface characteristics and resulting temperature variations. UHI and UCI should be analyzed in further research. Due to rapidly advancing sensor technology, soon, the existing spatial resolution of 1 km will be more improved.

Chapter 5: Analysis of Surface Urban Heat Island (SUHI) Using Nighttime MODIS LST Data as A Signal for Regional Micro-Climate Change-A Case Study in Dubai City, The United Arab Emirates (UAE)

Abstract

For the first time, Landsat images and Moderate Resolution Imaging Spectroradiometer (MODIS) Aqua Land Surface Temperature (LST) data have been employed in the current research to measure temporal-trend and spatial-patterns of Surface Urban Heat Island Intensity (SUHII) all over Dubai, UAE during 2003 to 2019. This research has been conducted for annual, summer and winter seasons. Around 17 years of chronological satellite database indicate the existence of a night-time SUHI. This research can advise climate change adaption endeavors, particularly urban-planning policies. Considerable Surface Urban Heat Island Intensity has been detected in the research area from the analysis of 17 years LST data. The winter season detected comparatively increased SUHII compared to the summer season. The metropolitan region of Dubai tournaments maximum SUHII due to especially developed areas. The time series analysis found an increasing trend in SUHII from 2003 to 2019, indicating intensified SUHI impacts in Dubai. Overall average SUHII of Dubai study area during annual, winter and summer seasons is 2.66ºC, 2.83ºC, and 2.23ºC, respectively. The magnitude in SUHII increases for annual, winter and summer by roughly 1ºC/decade. Urbanization in Dubai has transformed natural terrains of barren and desert land to man-made engineered textures and infrastructures. So, the SUHII and its extension start rising gradually with the development of city in both seasons. The elevated amount of SUHII is mostly concentrated in dense and high buildings. That extension shifted further away from the coastlines. The outcome uncovered the maximum SUHII attained over 7.3ºC in winter. While in summer, it did

not exceed 5.5ºC. Besides, the peak mean SUHII within the urban boundary fluctuated between (0 to 0.5ºC) in 2003 to (3.5 to 4ºC) in 2019. The highest SUHII (> 5ºC) has been recorded in a few locations that were regarded as Hot-Spot Sites (HSS). Amongst HSS, Dubai International Airport (DXB) is the hottest HSS in the summer season for the rise in number of travels. This phenomenon has been verified by difference of SUHII in DXB before and during the suspension. This research also illustrates some of the strategies for SUHI reduction.

5.1 Introduction

Rapid urbanization in cities around the globe results in substantial land use and land cover changes on the Earth's surface. It has been perceived as one of the most significant anthropogenic impacts on the climate (Zhou et al., 2011). Followed by Gutro, (2006), a UN (United Nations) assessment anticipated that 60-70% of world population will reside in cities by 2025, and many of the fastest growing regions for city growth are situated in arid locations. One of the foremost obvious and widely documented climatological impacts associated with urbanization is the urban heat island (UHI) effect that urban and suburban areas have higher temperatures than nearby rural or nonurban areas (Hu & Brunsell, 2013; Miles & Esau, 2017). As an indicator of urban climate modification, UHI has been studied broadly since Luke Howard initially recorded it in 1818 (Lin et al., 2017). The UHI phenomenon has been specified and recorded for numerous the major cities around the globe.

The UHI is linked to urban land changes, when impervious surfaces replace the nonurban area, resulting in a rise in heat storage and a drop in latent heat flux in urban areas (Mathew et al., 2018; Qiao et al., 2019; Zhou et al., 2016a). Urban temperature raise is mainly due to the absorption and trapping of solar irradiation in built-up areas connected to the thermal capacity of construction materials (e.g., concrete and asphalt), which rapidly alter surface albedo (solar energy absorption), evapotranspiration and emissivity (Zhou et al., 2017a). Consequently, a variation in air and Land Surface Temperature (LST) between urban area and nonurban areas (Azevedo et al., 2016) measured as UHI intensity (UHII).

The literature has been broadly recorded the adverse impact of UHI. Such as, it rises the temperature of cities; give rise to global warming (EPA, 2016); increases energy-demand of cities (Radhi & Sharples, 2013). This incident also indirectly render to climate changes around the world (Alghamdi & Moore, 2015); environmental deterioration (Lin et al., 2017); air-pollution (Zhu et al., 2020a); human healthcare and comfort (Schwarz et al., 2011); eco-system functionality (Keeratikasikorn & Bonafoni, 2018a); and promote heat related mortality-rate (Cui & De Foy, 2012; Lowe, 2016). Any single reason of these is enough to prompt interest in UHI studies. It is necessary to comprehend UHI attributes and the urban climatology responsible for it. This kind of circumstances predicts the increased effects of the UHI in the rising warm climate presumed to be sustained over the next few decades. UHI is mostly correlated with air temperature data obtained in-situ weather stations. Still, the representativeness is dubious because of comparatively inadequate data resources, and the irregular distribution of stations does not allow of an understanding over the study area (Bonafoni et al., 2017). While the surface UHI (SUHI) is conducted utilizing satellite derived LST data. The LST is the directional radiometric temperature of the

assembled surfaces viewed by the satellite. It is obtained by measuring thermal infrared radiation after correcting for emissivity and atmospheric effects. That overcomes the issues of in-situ measurements commonly with more comprehensive sources, extensive coverage, through different temporal intervals and constant periodicity (Alghamdi & Moore, 2015), assuring a more practical analysis of the interurban SUHI spatial variability. Accordingly, urban climatologists are referring more often about the remote sensing LST as accessible and convenient to represent SUHIs (Miles & Esau, 2017; Tran et al., 2006). Furthermore, advancement in satellite technology and data availability have facilitated a great number of SUHI research in several urban areas across the globe, providing temporal and spatial analysis of the urban heating structures (Hu & Brunsell, 2013; Keeratikasikorn & Bonafoni, 2018b).

SUHI mapping can fulfil the increasing demand for incorporating landscape ecosystems and urban development plans, providing scientific assistance for urban development policies. Following this context, remote sensing imagery is generally utilized to map impervious surfaces along with SUHI, the previous broadly known as a significant urban development indicator impacting the thermal pattern.

Many of the satellite sensors provide thermal infrared data at several spatial resolutions, in a range of 100m to over 1000m to acquire LST. The most popular of satellite sensors are the Advanced Spaceborne Thermal Emission and Reflection Radiometer (ASTER), Advanced Very High Resolution Radiometer (AVHRR), Landsat, and exceptionally the Moderate-Resolution Imaging Spectroradiometer (MODIS). Those sensors retain a similar configuration. The sensors are passive. Thus, they receive and measure reflected shortwave radiation (non-thermal bands) and emitted long wave radiation (Thermal bands) by the atmosphere and surface of Earth (Mohamed et al., 2017). This is important for SUHI studies because the conception of

controllers of SUHI is generally established in analyzing the relationship between two main factors comprising the LST/SUHI intensity of a region and the associated underlying land cover/use configuration and composition. Therefore, remote sensing imagery is a unique data for researchers to derive these factors through processing one data set (satellite imagery) for an entire city (Keeratikasikorn & Bonafoni, 2018a).

Landsat thermal bands have relatively high spatial-resolution (60 m to 120 m) and long-time series. Moreover, the inclusive Landsat thermal database was available freely since 2009. But the thermal research utilizing Landsat database are limited to daytime studies only. The restricted temporal range (16 days) and the unusual cloudless climates are other difficulties (Zhang et al., 2014a). Similarly, ASTER procures high resolution (90 m) during the daytime and in night, however, it has low temporal resolution. Moreover, although the common ASTER LST outputs have been accessible since 2001, the full database of ASTER data became accessible for free in 2016 (Zhou et al., 2019).

AVHRR LST has been uncommon for SUHI studies, because of the coarse spatial resolution and its operation is not as promising as MODIS LST (Noi et al., 2017). For this reason, the MODIS Terra and Aqua satellite sensors have been extensively utilized for LST measures and comprise a very significant and acceptable data source for SUHI research in recent years (Zhang et al., 2014a; Zhou et al., 2019). That mainly because its high temporal-resolution, global coverage within 1 km spatial resolution, unrestricted accessibility and can be obtained effortlessly (Tran et al., 2006). Additionally, it collected thermal data by the split window techniques, instead of the mono channel of the Landsat. MODIS allows the research of inter-annual, diurnal, and intra-annual variability of SUHI at different spatial scales. The standard MODIS LST data were made accessible in 2000.

Even though the incident of SUHIs is generally associated to urban sprawling and expanding industrial and human activities, the geographical location, urban materials, climate condition, seasons and duration of day and night may create different impacts. Besides, SUHIs exist at any time of the day. The following provides an overview on the importance of daytime and nighttime SUHI. Many researchers have observed that SUHI is greater in the daytime than nighttime (Schwarz et al., 2011; Wu et al., 2019; Zhou et al., 2018). In the contrary, other researchers have insisted that the SUHI appears at nighttime, when buildings and roads radiate the heat of sun absorbed during the day (Gupta et al., 2020; Mathew et al., 2017). Besides, temperature in the night is regulated by surface heat fluxes. The urban built-up store extra heat compared to the nonurban areas and consequently SUHI exhibits at night, particularly in arid regions where (Raj et al., 2020).

In the past literatures, SUHI has been explored in different cities around the world and especially emphasized in urban areas of Mediterranean, tropical, and cold climatic regions whereas arid regions with intensely high temperatures have been focused less (Rasul et al., 2016), particularly Middle East countries or surrounding cities that have same kind of arid desert climates. A few research on the SUHI phenomenon have published. Some research that focused on daytime, their findings revealed an inverse impact of the common SUHI phenomenon, where the urban areas recorded comparatively cooler than the suburbs. This phenomenon is called Surface Urban Cool Island (SUCI) for instance: in Abu Dhabi and Dubai, (Frey et al., 2005); Abu Dhabi, UAE (Lazzarini et al., 2013); Al Ahsa Oasis, Saudi Arabia (Alali, 2015). Other researchers have recorded that night SUHI, for example: Tehran, Iran (Haashemi et al., 2016), Riyadh, Saudi Arabia (Sherafati et al., 2018), Alahmad et al., (2020) in Kuwait.

Dubai has witnessed rapid urbanization during the past 20 years. It will probably go on in next decades also, driving increase of the SUHI intensity. In spite of a rapid urbanization in Dubai, the SUHI has remained non-discussed in prior studies. To bridge this gap, the objective of this research is to set to analyze the temporal and spatial changes of night SUHI over the Dubai city in range of 17 years (2003-2019) by using night MODIS Aqua LST data. Moreover, Landsat remote sensed images have been created to map and classify land cover to extract urban regions and the reference nonurban areas information.

5.2 Data and Methods

5.2.1 Study Area

Dubai is one of the seven emirates (states) establishing the United Arab Emirates (UAE). It is situated on the South-eastern shore of Arabian-Gulf. Dubai city is located between 24° 350N to 25° 180N latitude, and 54° 530E to 55° 440E longitude coordinates and surrounds a region of approximately 3,757 km^2 with coastline of around 72km. It is the second largest city and the most densely populated and developed city of UAE. It shares border lines with Abu Dhabi in the south and west side, Sharjah in the north-east (Figure 5.1).

Dubai is located in an arid climate followed by the Köppen climate classification (Peel et al., 2007). So, it has a mostly hot and dry climate, higher temperatures in summer (June to August) and in winter season (December to February) is moderately cooler. Precipitation is unusual and happens only in winter season, also have mean humidity over 90% in the summer season as claimed in National Centre of Meteorology (NCM). There is rarely to no vegetation cover, mostly restricted to landscaping in urban areas or to farming sectors.

In the last part of the 20th century, Dubai changed economical formation from predominantly petroleum based to an emphasis on tourism and financial activities. The reputation of Dubai as a city of commerce has attracted the people from other countries to come into this city. This migration occurs every year resulting considerably higher density of population. Accordingly, it has undergone substantial development over the last 20 years, both in terms of urbanization and population, and the trend is predicted to continue. In 2003, the population of Dubai was around 1,014,379. It had expanded to 3,355,900 (7.85% citizenship) by 2019 as recorded by Dubai Statistics Centre (www.dsc.gov.ae). Such growth has headed towards spatial expansion of urban areas, which can potentially carry to changes in SUHI of Dubai city.
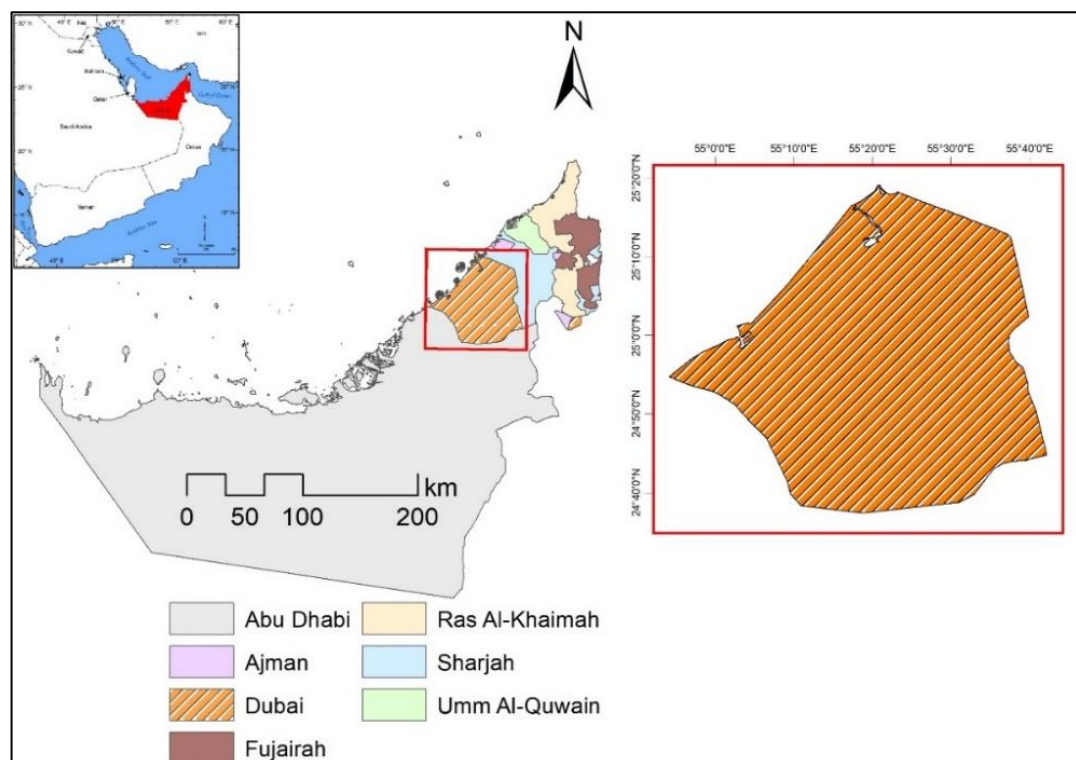
Figure 5.1: The study area, Dubai city, UAE

5.2.2 Land Cover Classification

Land covers data for 2003 and 2019 were obtained from the Enhanced Thematic Mapper Plus (ETM+) on board the Landsat-7 satellite and the Operational Land Imager (OLI) on board the Landsat-8 satellite from the United States Geological Survey (USGS) Earth Explorer (https://earthexplorer.usgs.gov/). The spatial resolution of this database was 30m, including one scene (Path: 160; Row: 43), cloud free vision for the whole study area on 28th May 2003 and 16th May 2019. The land covers were classified using supervised classification into four types: the vegetations refer to the trees, grassland, and cropland. Urban and built-up land comprising all the impervious surfaces of the city enclosing over 50% of the pixel considered. Bare land includes desert and barren lands. Water body contains lakes, ponds and reservoirs (Figure 5.3a). The accuracies of the classified products were evaluated by utilizing the high resolution images incorporated in Google Earth Pro®. The overall accuracy of the data was 92.7% with a Kappa coefficient of 0.89.

Land cover maps have been aggregated to 1 km for keeping consonance with the size of MODIS LST data. To be upscaled the 30×30 m land cover data pixels to the 1 × 1 km LST data, majority criterion was applied, combined with a nearest neighborhood transformation: the land cover type appointed to the majority of the land cover pixels in each LST pixel was used (Figure 5.1b). The topography of the area is primarily flat, and the elevation gained slowly from northwest to southeast and achieved around 290 m (Figure 5.1c) followed by the 30m resolution Digital Elevation Model (DEM), which was acquired from the Shuttle Radar Topography Mission (SRTM). The data was obtained from the USGS Earth Explorer (https://earthexplorer.usgs.gov/).

5.2.3 MODIS Data

Moderate Resolution Imaging Spectroradiometer (MODIS) has been completely accepted in a wide number of SUHI research, because of its global coverage, retrieval quality, high temporal resolution, high radiometric resolution and dynamic ranges, and accurate calibration in visible, near infrared and thermal infrared bands (Rasul et al., 2017b; Tran et al., 2006; Wan et al., 2004), which gives free daily LST data at a resolution of 1 km. MODIS comprise both the Aqua and Terra polar orbiting satellites, which pass the equator 2 times/day for each (Clinton & Gong, 2013; Wang et al., 2008). Across Dubai city, the crossing times are around 13:30 and 01:30 (Dubai Local time) for Aqua, 10:30 and 22:30 (Dubai local time) for Terra. The MODIS 1km LST data are attained by utilizing the generalized split window algorithms with screenings for cloud-effects usage of bands 31 and 32 in the 10.78mm to 12.27mm spectral span (Wan, 2014; Wan et al., 2002). The MODIS LST products were repeatedly validated across a set of sites and time periods using numerous ground truth and verification attempts (Duan et al., 2018; Wan, 2014).

According to Cui & De Foy, (2012), the daytime SUHII in arid climates was small and was not extensively implicated by the impervious surface region. Further, SUHI appears to be a special characteristic of arid cities (Alahmad et al., 2020; Clinton & Gong, 2013; Lazzarini et al., 2013). Moreover, the least surface temperature is recorded at midnight. It made Aqua night data an ideal option which is close to the SUHII intensity maxima. This study used the MYD11A2 version-6 (V6) performance from MODIS Aqua includes an eight-day composite of LST data at nighttime from 1st January 2003 to 31st December, 2019. Eight-day LST composite products can underestimate the quantity of gaps generated by clouds or some unwanted situations in the long time series that are advantageous to perform spatial comparison for SUHI

studies (Hu & Brunsell, 2013; Schwarz et al., 2011). Modern time LST products (V6) have covered earlier version accurateness problems, and measure errors in arid areas for bare land and validation analyses presently propose their application in these areas (Lu et al., 2018a). The night LST data for the study period under no cloud circumstance were extracted for Dubai city that is covered by two MODIS tiles, all data in the two MODIS tiles of granules with horizontal (h) and vertical (v) title numbers h22v06 and h23v06 were received from the Land Processes Distributed Active Archive Centre (LPDAAC) of NASA (https://lpdaac.usgs.gov/). The administrative boundary data for the UAE and Dubai city was gained from the Global Administrative Region Boundary Data Set (http://www.gadm.org/).

5.2.3.1 MODIS Data Pre-processing

Data was collected form Jan 2003 to Dec 2019 (1564 images) and was reprojected utilizing the Arcmap software to convert images to Geo-TIFF formats at UTM 40ºN with the WGS84 datum. Subsequently, a mosaic of two tiles and clipped the images using the boundary polygon which defined the study area was created. For better interpretation, temperature was converted from the Kelvin (K) unit to Celsius (ºC). Firstly, the unit was multiplied by an assigned scale factor of 0.02 to get Kelvin units. After that, it was subtracted by 273.15 to convert K to ºC (Wan, 2013). Every abnormal LST data with measurements greater than 100ºC or under −50ºC or any other measurements than the acceptable limit were noted as no data and ignored in the operation to deliver an acceptable dataset. Only valid pixels and good quality data were utilized following quality assessment (QA) layer. Additionally, any missing values were adjusted utilizing the average value of each series. Ultimately, LST data was aggregated to monthly period by averaging the eight-day composite data (almost 3-4

available monthly) to get monthly mean LST. According to the product quality control flag, the data that was utilized had an average LST error of $\leq$ 1ºC.

All images for each month were stacked jointly in a single file. The annual and seasonal mean for LST (ignoring no data value) was defined utilizing the Cell Statistics method for all the images between 2003-2019. The ESRI ArcGIS™ v10.4 software system and Microsoft Excel (spreadsheet) were utilized for the processing, analysis, exhibition, and quality control of the MODIS data.

Then, time series from 2003 to 2019 were constructed that comprised seasonal and annual nighttime LST. The seasonal and annual average values for urban LST (LSTu) and nonurban LST (LSTn) of the study area for pixels were calculated utilizing the outcomes of the urban and nonurban area identification. SUHI intensity of study area was then measured as the difference between LSTu and LSTn. A flow chart diagram of this task is illustrated in Figure 5.2.

5.2.4 SUHI Intensity Calculation

It is referred that SUHIs contain an intense danger to human wellbeing and comfort. Thus, the spatial extent of human activities needs to be specified when outlining the nonurban and urban areas to measure the SUHI. A significant parameter for researching SUHI is SUHI intensity (SUHII), which was estimated by the LST contrasts between urban and nonurban area (reference). Hence, it is important to select credible reference. However, the methods to specify the reference area differed extensively in various studies. Some of studies used areas like suburban (Yang et al., 2017a), rural (Schwarz et al., 2011; Yao et al., 2018b), forest (Zhou et al., 2018) and in a few cases one pixel in surrounding area has been utilized (Zhang et al., 2014a) . In this study, surrounding area (bare land/desert) was defined as nonurban areas that

may perform as the reference area for the analysis, after checking it has not been changed during the study period by utilizing chronological images from Google Earth Pro. For calculating the night SUHIIs, urban and reference nonurban areas were more delineated by steps below:

(1) Extracted urban area and reference nonurban location which fit the resolution of MODIS LST, the areas with impervious surfaces encompassing over 50% of the land were considered as urban areas (Figures 5.3a & b). To measure the mean of the LST of the urban and nonurban area more precisely, water body and vegetation land pixels were excluded, because significantly lower temperatures compared with urban and nonurban areas (Clinton & Gong, 2013).

(2) The reference area should remain unaffected by the urban area. It must locate far from urban areas at least 1km, since the SUHI's footprint was highly considerable than urban areas size (Yao et al., 2018a; Zhou et al., 2015).

(3) Pixels with DEM greater than 50m (Figure 5.3c) were removed depending upon the 30m SRTM DEM dataset to avoid the cooling impact on the SUHI quantification (Huang et al., 2019; Imhoff et al., 2010; Zhou et al., 2011). The remaining land-units were defined as the finally selected urban and reference nonurban areas as shown in Figure 5.3d.

Finally, the night SUHII under clear sky conditions at the Aqua satellite overpasses between 2003–2019 were measured by every pixel, by deducting the average LST of reference nonurban from the LST of all pixels by following Equation:

$$SUHII = LSTu – LSTn$$

(5.1)

Where LSTu is LST of urban pixels, and LSTn is average LST of reference nonurban. (Dec-Feb) and (Jun-Aug) are determined to depict cold winter and hot summer respectively. On the other hand, the data for the fall and spring seasons (transitional seasons) are not evaluated. Thus, the SUHII for each pixel for winter, summer and annual was calculated and utilized to present the SUHI of Dubai city. Linear regression analyses were conducted in Microsoft excel to evaluate the temporal trends of SUHI intensity. Comprehensively, the selected methodology is explained using the flow chart diagram in Figure 5.2.
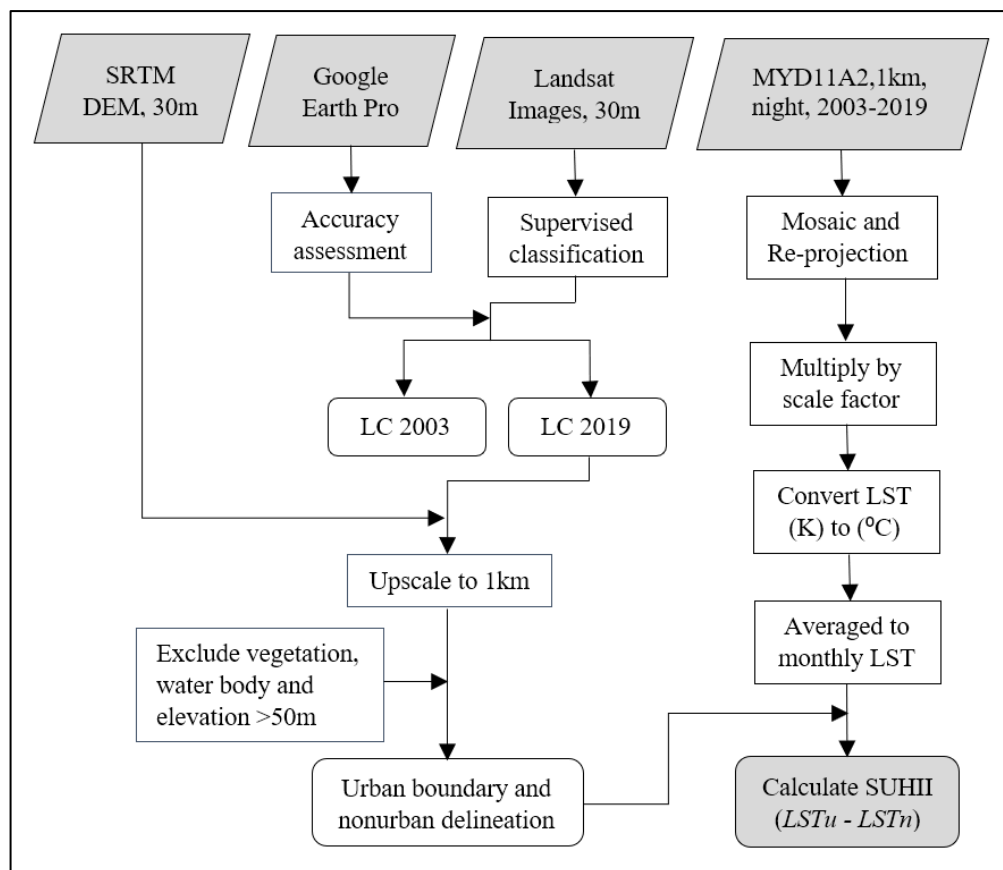
Figure 5.2: Flow chart exhibiting the process of SUHII calculation
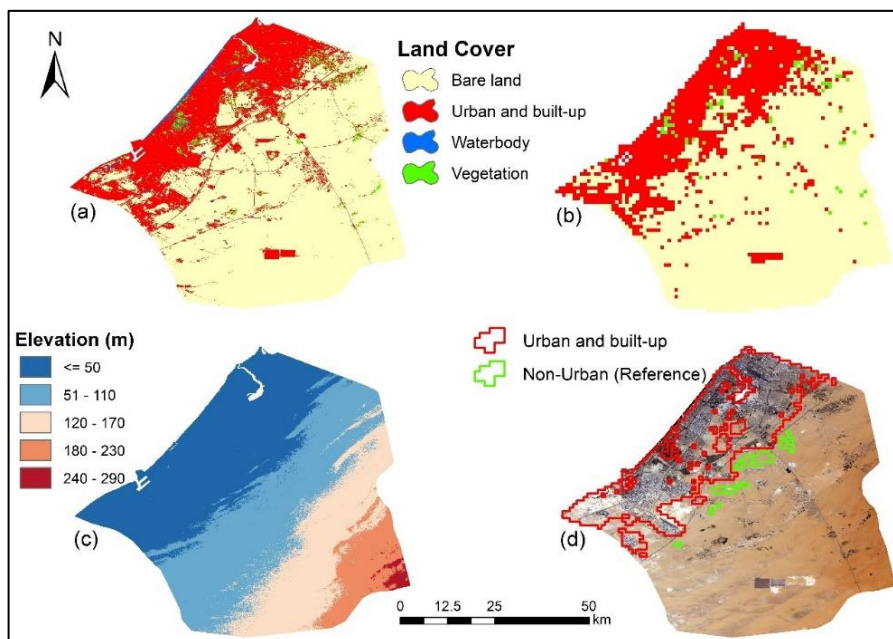
Figure 5.3: The illustration of urban and reference nonurban areas for calculating SUHIIs. (a) Landsat land cover 30 m × 30 m; (b) resampled land cover 1km × 1 km; (c) elevations; (d) final urban area (red), reference (green) boundaries, and Landsat true color image of study area (16th May 2019).

5.3 Results and Discussions

5.3.1 Temporal Changes in SUHII

The seasons were specified followed by LST; the seasonal LST is at its maximum in Dubai during summer season and records minimum LST during winter season as shown in Figure 5.4, Summer and winter seasons endured either the maximum or the minimum SUHII impacts, and the SUHIs in summer have highly affected human lives (Yao et al., 2018b). Accordingly, these two seasons were primarily focused on for the analysis with spring and autumn excluded.
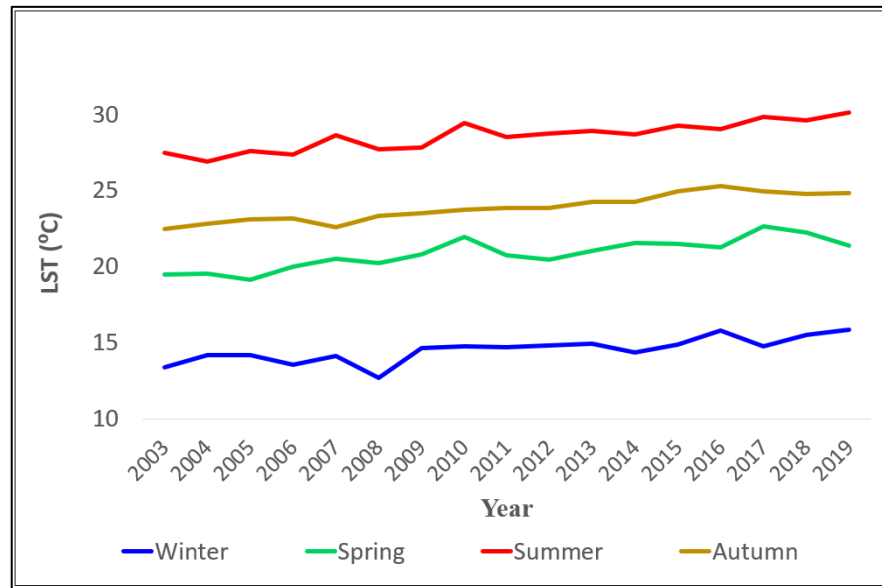
Figure 5.4: LST-data of seasons in Dubai from 2003 to 2019

Figure 5.5a and b show the monthly and seasonal mean SUHII during the study period from 2003 to 2019, the mean SUHII for seventeen years was 2.66ºC. The summer season undergoes comparatively lower SUHII if contrasted to winter. The mean SUHII during daytime in summer was 2.23ºC, and in winter SUHI intensity was 2.83ºC. The SUHII varied with its levels reaching a higher value of 2.94ºC in December. And the minimum SUHII was observed in July with a measurement of 1.91ºC. (Figure 5.5b). This outcome aligned with the previous literature from local and worldwide studies (Barat et al., 2018; Goswami et al., 2016; Lazzarini et al., 2013; Mathew et al., 2017; Miles & Esau, 2017), they found that SUHII in summer was less than winter season. In contrast, many studies indicated the night SUHII show high values in summer (Li et al., 2018a, 2018b, 2017; Yao et al., 2017, 2020; Zhou et al., 2018).
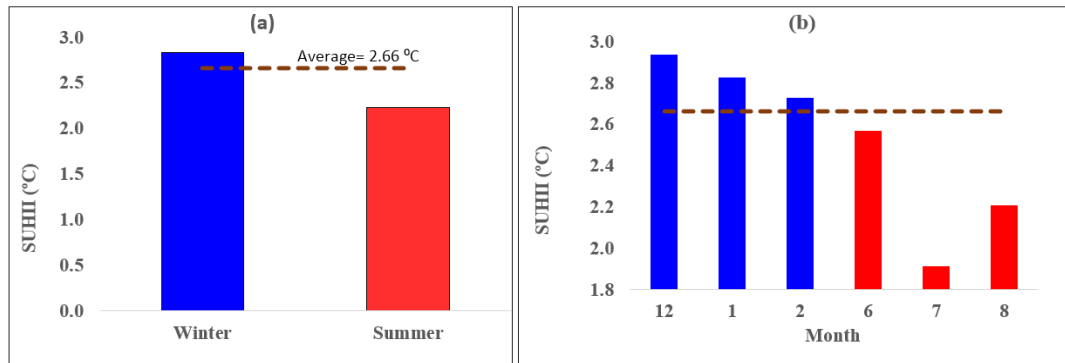
Figure 5.5: Variations of SUHII. (a) annual and seasonal SUHII; (b) monthly SUHII. Over the urban areas in Dubai city during study period 2003-2019

As indicated before, in Dubai city the SUHI is maximum in winter compared with summer. That may associate to the following reasons: the specific heat capacity for conventional urban surfaces materials for instance concrete, asphalt, aluminum, and bricks is more than sand (Lazzarini et al., 2013; Reisi et al., 2019). This means that sands in desert land exhibit a huger reduction in LST than the urban surfaces over nighttime. However, during summer season daytimes are longer and shorter nights, with peak temperatures that makes the sand of desert land warmer promptly, so the desert does not get sufficient time to cool at night. Therefore, the urban and desert temperatures get closer. On the other hand, in winter season, the nighttime duration is extended, and the daytime duration is less than summer, so the opposite happens. It is worthwhile to mention that, in winter season, sometimes the night temperature of desert area goes down nearly 0°C that creates large deference to the LST of urban and reference desert area (Figure 5.5).

Other reasons could be related to the existence of urban aerosols or haze in the atmosphere (dust and water vapor). It is also contributing factor to nighttime SUHI, which is common in arid areas in the summer season (Barbulescu & Nazzal, 2020; Lazzarini et al., 2013). As it impacts on the transmission and emission of incoming radiation and enhances the interception of outgoing radiation (Qiao et al., 2019). A

more intense analysis of the mesoscale climate of the area will enable to improve classification and understanding of these specific conditions.

Moreover, mainly most residents and citizens travel abroad in summer months. Such as, followed by General Civil Aviation Authority (GCAA: https://www.gcaa.gov.ae/). In 2019, approximately 280,000 passenger/day fly from Dubai International Airport (DXB) during the summer season especially in July when the educational vacations begin. Therefore, the human activities will drop that will direct the SUHII to be less than winter season across Dubai. As observed in Figure 5.5b that July has the lowest SUHII value. Furthermore, the correlation scattering diagram between population and SUHII for the winter and summer of 2019 is demonstrated in Figure 5.6. As it can be seen that the correlation in winter is higher (R^2=0.81) in comparison to summer, which has no correlation (R^2=0.21). Therefore, the contraction of population due to the summer holidays resulting in SUHI alleviation in summer. This finding clarifies the reason behind the SUHII in winter higher than summer season. It also shows how population/human activity play significance role in SUHII. Hence, the SUHII in DXB particularly attains the maximum value in summer season and that can be found in Section 3.4 below.
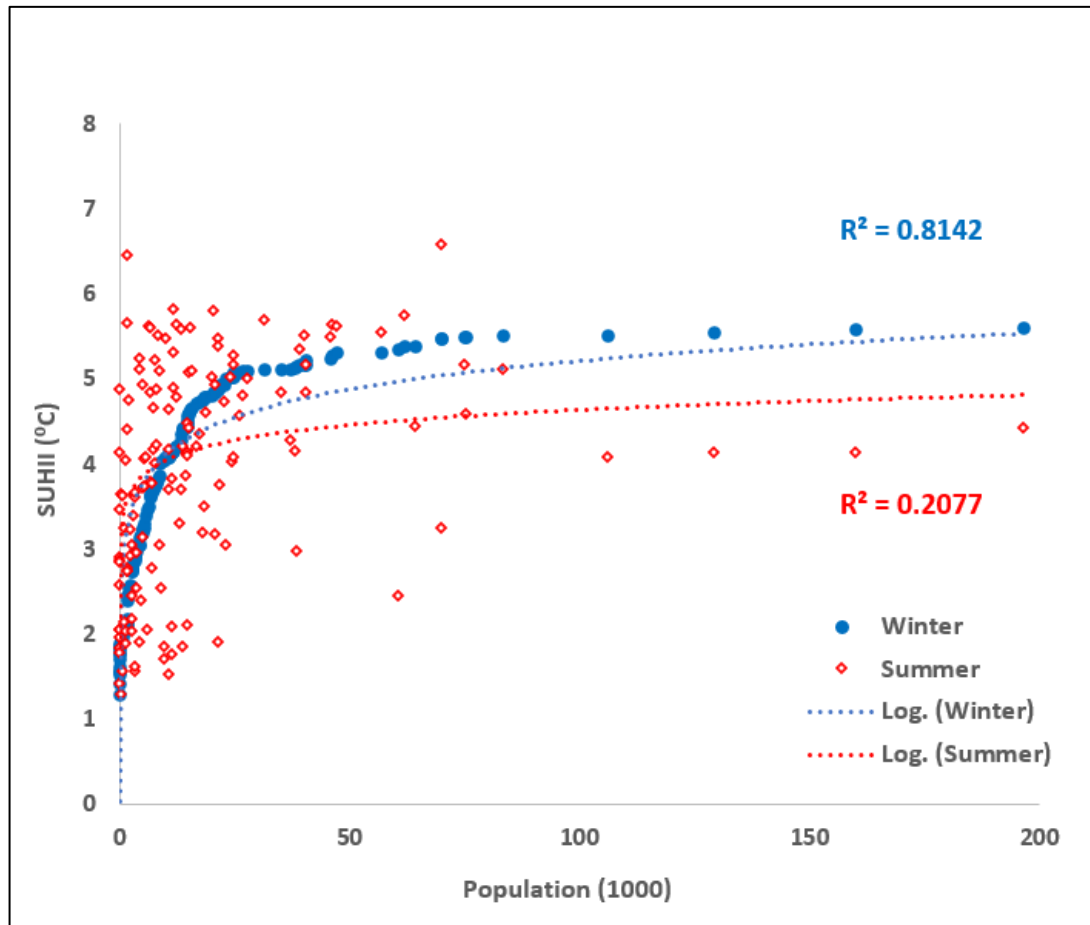
Figure 5.6: Scatter plot of the population and SUHII for winter and summer in 2019

5.3.2 Temporal Trends of SUHII From 2003 to 2019

In this section, temporal trend changes in SUHII across Dubai are analyzed for the 17 year period. Figure 5.7 shows the temporal trends of mean SUHII in considered seasons and annually from 2003 to 2019. The annual and both selected seasons SUHII increased significantly for the whole study period. The changing trends of SUHII are totally constant among annual, winter and summer. The magnitude of increase in SUHII for annual, winter and summer is (~1ºC/decade). The summer trend SUHII is slightly gaining at a quick rate than winter season and it was 0.1105ºC/ year, followed by annual SUHII 0.0995ºC/year, and winter SUHII 0.0971ºC/ year. Moreover, the SUHII enhanced in the winter season, where the lowest value of 1.97ºC in 2003 to the

highest value of 3.56ºC in 2018. While the SUHII derived for the summer, it exhibits

relatively lower value of 1.21ºC in 2003 and to a higher value of 3.26ºC in 2017. It is

also evident to an overall annual rise of 1.66ºC in 2003 to an utmost 3.45ºC in 2017,

2018 & 2019.
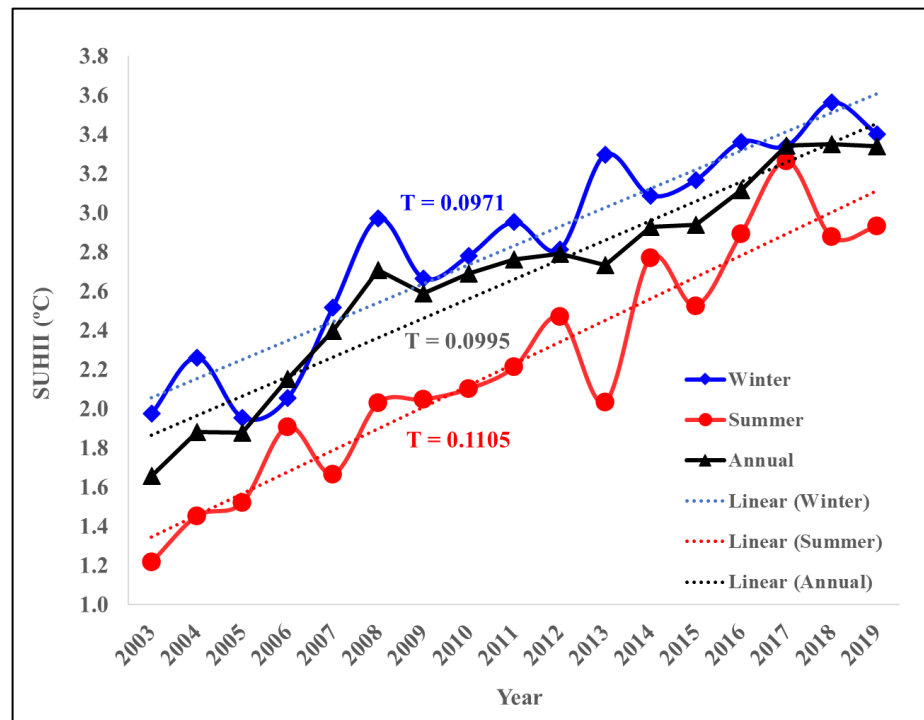
Figure 5.7: The temporal trends of mean SUHII from 2003 to 2019. Summer, winter
season and annually. T= trend (ºC/year)

5.3.3 Spatial Distribution of SUHII

The spatial distribution of SUHII for each year in selected seasons from 2003

to 2019 across Dubai is displayed in Figures 5.8 and 5.9. The results clearly ascertain

the expanding of SUHII and the spatial extent over 17 years. Typically, the SUHII

values grow stronger in winter and weaker in summer throughout 17 years. The

recorded highest SUHII in winter attained over 7.3ºC. However, the SUHII resulted in

the summer, the highest recorded intensity did not transcend over 5.5ºC over the entire

study period. Overall, in both seasons, a significant SUHII incline was documented extending from south-eastwards from the coastline (city center) to nonurban areas where temperatures can be in range of (5.5-7.5ºC) less heat than the city centre in both seasons.

According to the land cover that was obtained from Landsat data, the built-up area of Dubai has undergone an overall increase from 455 km^2 in 2003 to 1012 km^2 in 2019. These areas mainly came from natural barren/desert lands are being rebuilt to urban infrastructures. As well as the urban expansion has been increasing from northwest costal area toward southeast nonurban areas where sandy desert land is located. This replacing natural lands with impervious surfaces that shifts natural characteristics to lessened albedo, and additional anthropogenic heat and higher heat storage. These changed direct to the increase of SUHII. Besides, during the nighttime, the energy flux from the surface to the atmosphere is the sum of heat stored during the in the daytime and released at nighttime, and of anthropogenic heat created in the night inside the city (Peng et al., 2012; Wang et al., 2019a). The surface heat storage is associated to albedo and heat capacity and conductivity of the urban areas in daytime. It is emitted upward to the atmosphere in the nighttime, renders to maintain high temperature over urban areas. Besides, a negative correlation between night SUHII and albedo (Peng et al., 2012; Shastri et al., 2017) as well as a positive correlation between night SUHII and the heat capacity (Lazzarini et al., 2013). Thereafter, as a comprehensive overview of Figures 5.8 and 5.9, SUHII and its extension begins expanding gradually along with the expansion of urbanized areas. Further, high value of SUHII is primarily concentrated in dense and high buildings and it reduces continuously shifting away from coastline to lesser urbanized and less densely populated and nonurban areas. In southeast part of Dubai, lower thermal capacity/heat

storage of desert that are not impacted by the urban area or human activities resulting in the lowest night SUHII values were detected in comparison to urbanized areas (Figures 5.8 & 5.9). As noticed, the association among SUHII and urbanization is quite consistent among different years regardless of the seasons. SUHI is generally affected by the scale and intensity of human activities rather than seasons. Therefore, the spatial distribution pattern of SUHII was similar in both winter and summer as shown in Figures 5.8 and 5.9. Even though the considerable differences of SUHII values were found in different seasons. So, the spatial magnitude of urban infrastructure or urban land covers is a basic component contributing to the spatial patterns of the SUHII. This is concordant with other studies. These indicated that the main effect was anthropogenic heat emancipation and landscape pattern distinctions in urban and nonurban areas, and night SUHII has positive relationship with urbanized areas (Alahmad et al., 2020; Clinton & Gong, 2013; Cui et al., 2016; Li et al., 2017; Mohammad et al., 2019; Tan & Li, 2015).

The population of the city of Dubai has witnessed a rise of almost 2.34 million in 17 years. It increased drastically from 1.1 million in 2003 to 3.35 million in 2019 with a growth rate about 235% from 2003 to 2019. And it is projected to expand up to 5 million by 2030, which would be approximately 5 times of 2003 as estimated by Dubai Statistics Centre (https://www.dsc.gov.ae). Since lake status of urban vegetation layer with increasing population, hereafter increasing built-up areas and associated anthropogenic heat emissions resulting in SUHII with raised values and extension. This outcome is consistent with a large amount of studies, which is found by expanding urban area, the SUHII tends to rise (Benas et al., 2017; Clinton & Gong, 2013; Firozjaei et al., 2018; Imhoff et al., 2010; Miles & Esau, 2017; Mohan et al., 2012; Tran et al., 2006; Wang et al., 2016, 2019a; Zhou et al., 2016a).

Generally, the peak of average SUHII inside urban boundaries changed from (0-0.5ºC) in 2003 to (3.5-4ºC) in 2019 indicating the permanence of an urban heating. Also, most of values over 1ºC of SUHII became more in 2019 and it would increase in value in future (Figure 5.10). Therefore, it is essential to execute heat island mitigation strategies in the city of present time. For further intensifying heat island effect in Dubai can be prevented.
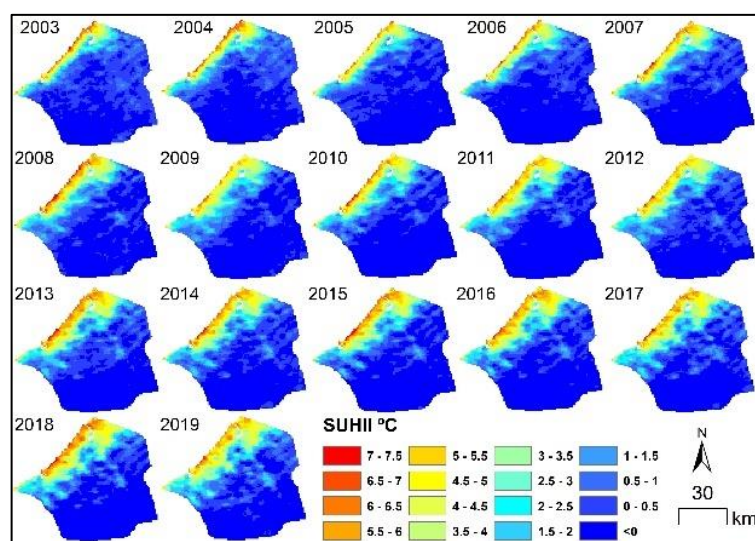
Figure 5.8: Spatial distribution of annual SUHII (ºC) in winter from 2003 to 2019
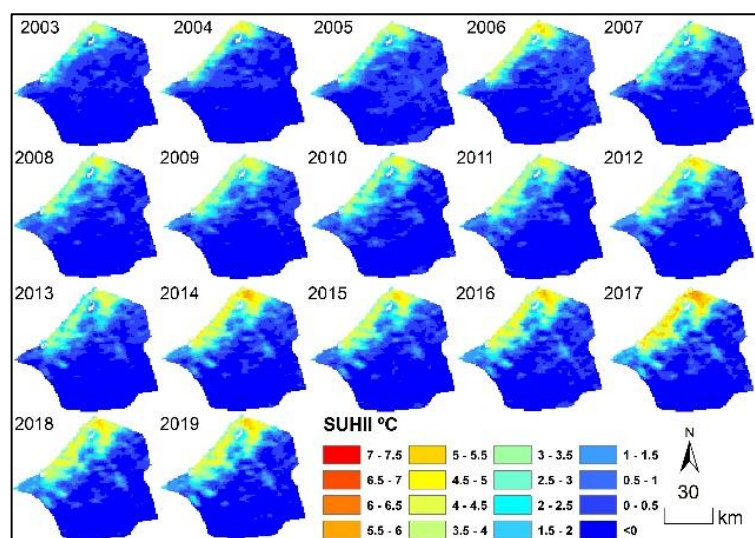
Figure 5.9: Spatial distribution of annual SUHII (ºC) in summer from 2003 to 2019
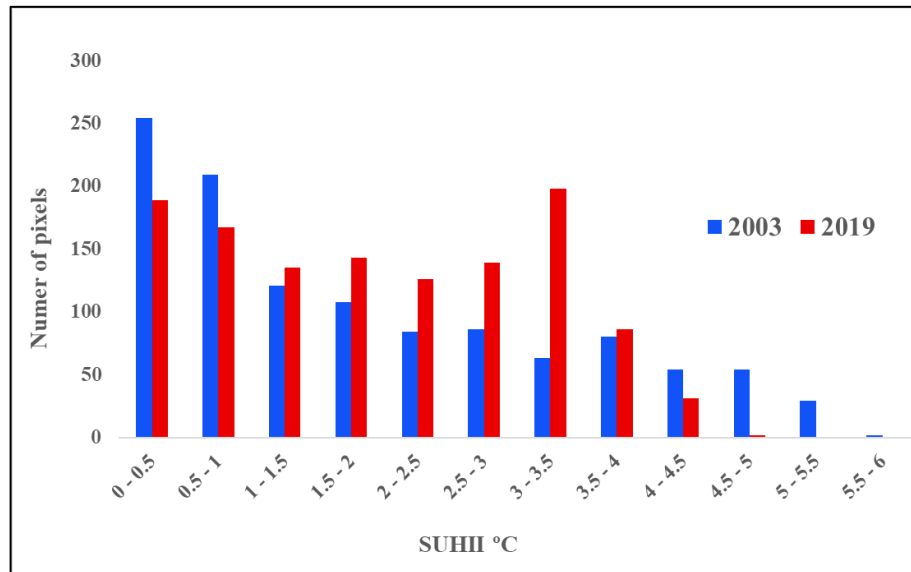
Figure 5.10: Dispersion of the number of pixels (1km²) into urban boundary with different SUHII in 2003 and 2019

Additionally, SUHIIs are particularly driven by explicit annual thermal conditions without regarding urban growth. These results confirm how the spatiotemporal urban heat patterns rely extensively on the background climate, such as air temperature, solar radiation, precipitation, and wind velocity (Zhou et al., 2018). To exemplify, the maximum mean SUHII was noticed in winter of 2018 (Figure 5.7). The reason behind these is that this year had the least number of rainy days from the record of the National Centre of Meteorology (www.ncm.ae).

5.3.4 Hot Spotted Sites

Figure 5.11 represents some sites of 1 km spatial resolution that are specified as greatest values of average SUHII (>5ºC) during the entire 17 year (Figure 5.13), these sites are named as Hot-Spotted Sites (HSS). These can assist the designated departments in municipality authority to point out focus areas for taking steps for cooling procedures. HSS includes densely populated areas, such as the Deira (DER) and Um Suqaim (UMS); Dubai International Airport (DXB); Burj Khalifa (BKH)

which is the world's tallest tower; Shaikh Zayed Road (SZR) is described as high density of tall buildings and high concentrations of cars; finally, Jabal Ali Industrial (JAI).

Among these HSS, SZR and JAI are the hottest locations during 17years in Dubai city with over 6ºC of mean SUHII. The SZR is home to most numbers of Dubai's skyscrapers (Figure 5.11d), and It is verified that high-rise buildings are causing heat that cannot escape into the atmosphere. Besides, these high rise buildings create a complex geometrical structure that traps energy inside and shifts the airflow, this increasing the proportion of energy availability to heat the urban surface (Tam et al., 2015). Additionally, this road is the main passage of city and counted as one of the most UAE's busiest highways. Due to many automobiles are also known as a component that increases the SUHII as inferred in a previous research (Firozjaei et al., 2018). Thus, SZR generates one of the highest mean SUHII. Most of the factories in UAE are situated in JAI. Those factories were built using high temperature capacity materials as shown in (Figure 5.11e). Further, those factories release a huge quantity of the anthropogenic heat. As a result, its mean SUHII exceed 6ºC as well.

DXB is the major international airport operating in Dubai and is also the third most active airport in the world by passenger number according to Airports Council International (https://aci.aero/). That illuminates with the dark airport surfaces (Figure 5.11a) that makes DXB obtained high mean SUHII of 5.13ºC.

The BKH area (Figure 5.11c) also shows high SUHII of nearly 5.14ºC. This could be clarified by the height and the buildings materials of high thermal capacities.

Even though, there is no high altitude buildings or factories in DER and UMS (Figures 5.11b & f), but these areas were specified by large urban size (dense low rise buildings) as illustrated in Figure 5.11b. Additionally, they are known as the densely

populated areas in Dubai city (https://www.dsc.gov.ae). So, the mean SUHII varies between 5.27ºC to 5.40ºC respectively for UMS and DER.
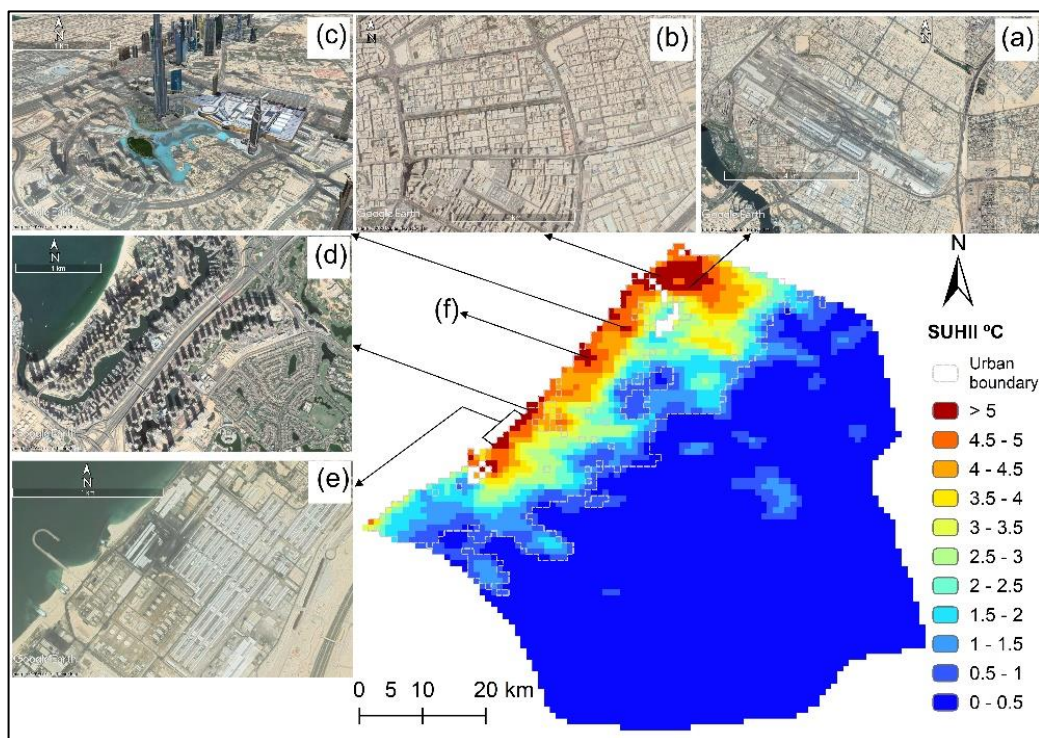
Figure 5.11: Spatial distributions of highest sites (pixel) of mean SUHII (ºC) from 2003 to 2019. Letters (a-f) indicate Hot-Spotted Sites (HSS) of the study area, namely (a) DXB; (b) DER; (c) BKH; (d) SZR; (e) JAI; (f) UMS. (Images source: Google Earth™ mapping services)

Figure 5.12 exhibits the mean SUHII trends for five HSS (excluding UMS) in duration of (2003-2019). It is noticed that the trend is nearly constant for all HSS (exception BKH). BKH's construction was started in 2004 and finished in 2009 (www.burjkhalifa.ae). It is apparent that, mean SUHII increased drastically from 2004 onward and remarkable difference of SUHII time series trend is witnessed between BKH and others with highest trend of 0.202ºC. That exhibits how land cover change led to an increase in SUHII. On the other hand, DER which is the one of the oldest district and any new construction is very limited according to Dubai municipality (www.dm.gov.ae). It appears with the lowest trend of 0.007ºC. Moreover, all other

sites show comparatively less difference in trend. It ranges between 0.025ºC-0.049ºC as exhibited in Figure 5.12.
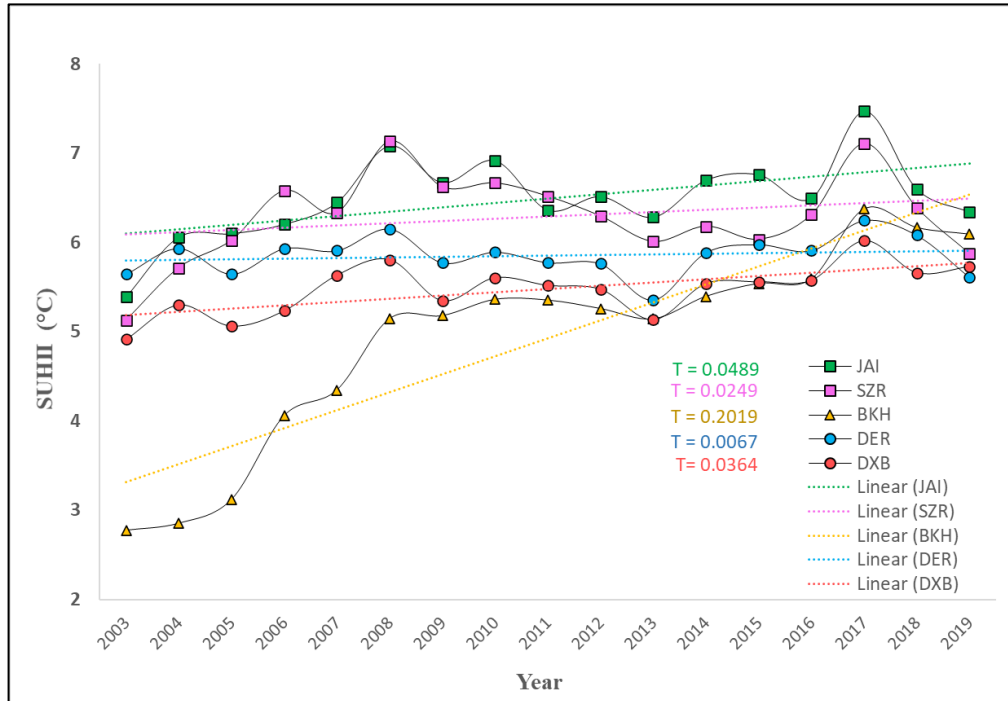
Figure 5.12: Annual mean SUHII trends for each HSS

More analysis was done on how the differences in energy used in transportations and heat generation in DXB influence in SUHI. As demonstrated in Figure 5.13, DXB has the maximum SUHII in summer and minimum difference between winter and summer is nearly 0ºC. The reason behind this is continuously travelling and airplane movements throughout the year resulting in heat production and that rises especially in summer as indicated previously in (Section 3.1). Thus, the SUHII in summer has similar value as winter and highest summer SUHII in the HSS as documented in Figure 5.13. Due to the epidemic condition of COVID-19, all business activities have been prohibited in UAE. The government discontinued most passenger's flights and all transition flights. Hence, the summer month (June 2020) and the same time of the 2019 have been selected to assess the variations of SUHII

before and during COVID-19 in DXB. As interpreted based on statistical presentation on Figure 5.14, aircrafts travelling are appreciably participating to the increase of SUHII in summer of 2019, because of anthropogenic heat generations. Whereas in June 2020, because of prohibition and absence of those activities that render to alleviation of the SUHII. Obviously, this investigation demonstrates and confirms the positive correlation between SUHII and emitted heat energy, and the way it made DXB one of HSS in Dubai city. Since the DXB located in an urban area, that would lead to a raise of health-related issues of residents.
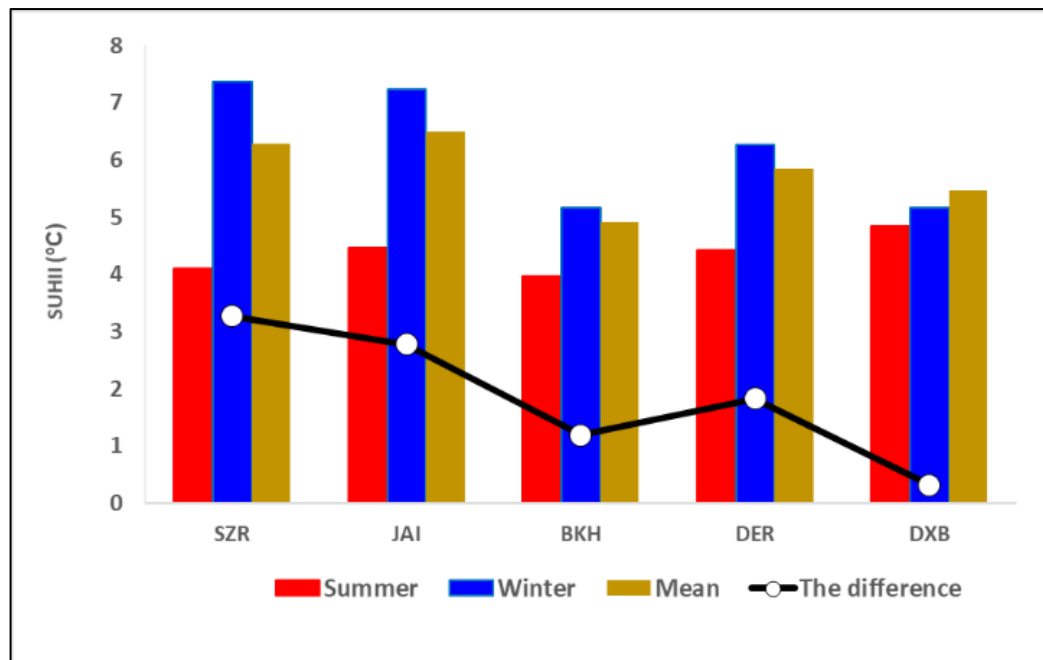
Figure 5.13: Variations of mean SUHII for each HSS in winter and summer. The difference between winter and summer SUHII, and annual mean SUHII during period (2003-2019)
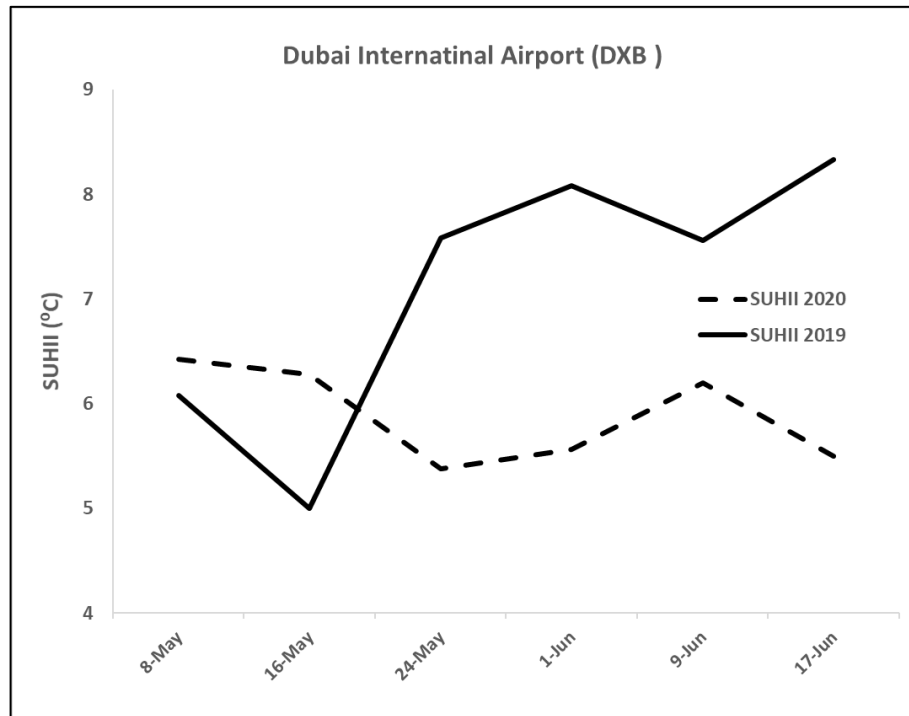
Figure 5.14: Graphical representation exhibiting fluctuations of DXB SUHII in summer 2019 and in summer 2020

In general, HSS emerged within the city boundaries with huge density of population, dense and high buildings, industrialized and strong anthropogenic heat release (Hu et al., 2019c). Urban infrastructures with building dense, tall skyscrapers and surface materials influencing the nighttime surface energy interaction, therefore, affect the nighttime SUHI (Tran et al., 2006; Voogt & Oke, 2003). Densely situated and tall buildings absorb heat, decrease airflow, and produce hot air from Air Conditioner (AC) usage (Deilami et al., 2018). Further, manmade dark impervious surfaces absorb shortwave radiations and reserve heat energy in daytime and then emit longwave radiations slowly at night, contributing to the nighttime SUHI (Wang et al., 2016). Urban areas are packed with vehicles and other heat generating activities released from burning fuel (Hart & Sailor, 2009). In short, anthropogenic activities and heat emission (e.g., AC operations, fuel usage in transportation, industrial heat

production) in the urban area is critical contributor to urban temperature rising and have more effects in space that in time (Mohammad et al., 2019; Peng et al., 2018).

5.3.5 Mitigation of SUHI

Nowadays, the construction of highways, manufacturing frameworks, and buildings in Dubai city cannot be avoided. This situation will obviously lead to the increment of SUHI values. Thus, it requires urgent consideration from government, policymakers, urban-planners, private organizations, and community. The mitigation and adaptation strategies of urban temperature environment management need to be concentrated on lessening the SUHI effect on Dubai city, especially the vital areas. Therefore, the HSS should be specified as the major zones. Otherwise, the SUHI will incline to nonstop exacerbation. There are numerous mitigation strategies proposed internationally to tackle urban heat issues.

As discussed hereby, this research found a negative correlation between SUHII and albedo at night. So, using lower albedo surface materials (asphalt and concretes) with high albedo and high emissivity surfaces and less conductivity for new infrastructure may maintain the surface cool when exposed to solar radiation.

It is widely recognized that the increase of vegetation and green covers in the urban texture is one of the fundamental methods to reduce SUHI (Haashemi et al., 2016; Keeratikasikorn & Bonafoni, 2018a). Hence, for SUHI reduction, green infrastructure and, roof-top gardens, parks, roadside trees plantation, reserved green area, introducing reflective rooftops and walls (e.g., white/bright color), checking building materials and other urban renewal methods had been ascertained to be useful, along with controlling the sources of anthropogenic thermal emission (Azhdari & Taghvaee, 2018; Bonafoni et al., 2017; Cui & De Foy, 2012; Elmes et al., 2017; Sun

& Chen, 2017; Yu et al., 2017). Alongside, people can make roof curtains, green-walls and gardens. This can improve the moisture in the city and can additionally decrease the rate of thermal emission and SUHI phenomenon. Observed evidence exhibited that large scale applications of green roofs decreased ambient heat by 0.3 to 3ºC (Santamouris, 2014). Vegetation can intercept solar-energy, provide shade to surfaces and has a higher albedo than pavement, plants absorb and accumulate less heat, while the evapotranspiration process helps to reduce the temperature of the atmosphere (Alahmad et al., 2020; Millward & Sabir, 2011). Furthermore, rising water bodies via artificial streams are promising to reduce temperatures at the nighttime SUHI (Rasul et al., 2017a). Earlier studies also suggested that urban planning can impact on urban heating and proper land use strategies can reduce the effects of SUHI (Kardinal Jusuf et al., 2007; Tan & Li, 2015). Besides, disperse or stretched urbanizations are fit for SUHI mitigation as found in some work (Zhou et al., 2017a). Eventually, any contraction in the effect of SUHI on local temperatures in Dubai city is inclined to have a positive effect on the live ability and wellbeing of its residents and make living more satisfying and comfortable.

5.4 Conclusions

The understanding of the variation of the surface thermal environment is crucial for SUHI adaptation and mitigation. For this research, the urban and nonurban reference areas of Dubai city in UAE were identified depending on land cover data. Likewise, the spatial and temporal change of SUHII which is acquired from MODIS LST was analyzed from the annual, summer and winter during 2003 to 2019. The findings indicated that, SUHII was occurred in nighttime in Dubai city, with the stronger SUHI in winter season compared with summer season, but their extension

was analogous during study period. Additionally, utilizing temporal trend analysis, there was an increasing trend in SUHII in selected seasons and annually from 2003-2019, that reaches around 1ºC/decade. By analyzing spatial patterns of SUHII alteration, the outcomes showed increase in the value and expanse of SUHII with the growth of the urbanization across the Dubai city, and the more intensively situated in coastline with dense and tall buildings, airports, industrial areas, and densely populated area and more human activities, in comparison to nonurban areas in barren land and desert. The HSS in Dubai have undergone a severe SUHII more than 5ºC. However, increasing population and change in land use and land cover, and related anthropogenesis thermal activities needs strategic mitigation steps in the city to stop further strengthening of the heat island effect.

This detailed research can generate additional information for the government and the public to understand climate change in specific micro-climate in the Dubai city. It is very necessary, because it will be used as a preliminary or reference information for future development planning.

5.5 Limitations and Future Studies

Some limitations in this study should be mentioned here. Firstly, this study was not proficient to validate the excellence of the data of the LST data, because no accessibility to the fresh/raw data that were acquired in the satellite passes. However, no obvious flaws was encountered within the processed LST values. Secondly, the spatial resolution of 1km might not interpret with finer features of hot-spots inside the urban city. Additionally, satellites might not be proficient enough to accurately capture temperatures from surfaces that are hidden by trees or high constructions. Subsequent constraint based on the cloud cover impact including missing pixels, and the pixels

covered by thin clouds. Finally, it is noteworthy that this analysis of SUHI in Dubai city is only over 17 years of satellite data. This is also clarified that there was limitation in chronological data archive of MODIS. However, findings obtained in this research may be relatable to a corresponding duration in a 30 year data set. Methods used in the current research might also be applied in SUHI analysis of other cities. Therefore, studies for additional time periods and for other cities in UAE are planned. Additionally, the impacts of climate conditions, for example, cloud cover, wind, and precipitation on the SUHI need to be taken into account in future studies, moreover, land use with more attributes need to be seriously considered.

Chapter 6: Impact of COVID-19 Lockdown Upon the Air Quality and Surface Urban Heat Island over the United Arab Emirates

Abstract

The 2019 pandemic of Severe Acute Respiratory Syndrome-Corona Virus Diseases (COVID-19) has posed a substantial threat to public health and major global economic losses. The Northern Emirates of the United Arab Emirates (NEUAE) had imposed intense preventive lockdown measures. On the first of April 2020, a lockdown was implemented. It was assumed, due to lower emissions, that the air quality and Surface Urban Heat Island (SUHI) had been strengthened significantly. In this research, three parameters for Nitrogen Dioxide (NO_2), Aerosol Optical Depth (AOD), and SUHI variables were examined through the NEUAE. As revealed by satellite data for two cycles in 2019 (March 1st to June 30th) and 2020 (March 1st to June 30th), the percentage of the change in these parameters were evaluated. The research's core results showed that during lockdown periods, the average of NO_2, AOD, and SUHI levels declined by 23.7%, 3.7% and 19.2%, respectively, compared to the same period in 2019. Validation for results demonstrates a high agreement between the predicted and measured values. The agreement was as high as R^2=0.70, R^2=0.60, and R^2=0.68 for NO_2, AOD, and night LST, respectively, indicating significant positive linear correlations. The current study concludes that due to declining automobile and industrial emissions in NEUAE, the lockdown initiatives substantially lowered NO_2, AOD, and SUHI. In addition, the aerosols did not alter significantly since they are often linked to the natural occurrence of dust storms throughout this span of the year. The pandemic is likely to influence several policy decisions to introduce strategies to

control air pollution and SUHI. Lockdown experiences may theoretically play a key role in the future as a possible solution for air pollution and SUHI abatement.

Keywords: COVID-19; NO$_2$, AOD, SUHI, Lockdown, Northern Emirates.

6.1 Introduction

Emerging of Coronavirus disease 2019 (COVID-19) is a transmittable disorder characterized by severe acute respiratory syndrome coronavirus-2 (SARS-CoV-2) (Islam et al., 2020). By massive human-to-human transmission, COVID-19 has deeply hit the world and prompted the human mortality rate and massive economic casualties around the world (Bukhari & Jameel, 2020). The number of cases of Covid-19 globally hit approximately 34 million by the first of October 2020, while the number of deaths reached 1 million (WHO, 2020c). In late 2019, the first case of COVID-19 was identified in China and since then has spread very quickly throughout the world (Li et al., 2020b). On 11 March 2020, the World Health Organization (WHO) announced the novel coronavirus disease as a pandemic (WHO, 2020b). The WHO COVID-19 dashboard (https:/covid19.who.int/) can be used to find the specifics of global COVID-19 cases. The first COVID-19 infection was reported in the United Arab Emirates (UAE) on 29 January 2020, and the first death was recorded on 21 March 2020. Since then, as per the Ministry of Health and Prevention (https:/www.mohap.gov.ae/), there has been an alarming surge in active and death cases due to COVID-19.

In people with cardiovascular and respiratory disorders, who is also closely related to air pollution, the mortality risk of COVID-19 is substantially higher (Archer et al., 2020; Isaifan, 2020; Zhu et al., 2020b). Emissions leading to respiratory health conditions from primary pollutants containing particulate matter (aerosols) and gases

such as Nitrogen Dioxide (NO_2) and also have adverse environmental effects like soil and water acidification (Griffin et al., 2019; Mulenga & Siziya, 2019; Xu et al., 2020). Besides, the WHO (2020a) reports that approximately 4.2 million inhabitants die worldwide per year from factors primarily related to air pollution. It is presently accompanied by increased death tools in COVID-19 infected patients (Conticini et al., 2020; Wu et al., 2020).

Urban Heat Island (UHI) is among the most noticeable and frequently reported urbanization climatological consequences, by which urban and suburban regions are hotter than surrounding areas (rural/nonurban) (Hu & Brunsell, 2013; Miles & Esau, 2017). The negative influence of UHI has been extensively described in the literature. For example, rises energy demand (Alghamdi & Moore, 2015), which implicitly leads to global climate change (Alghamdi & Moore, 2015); environmental degradation (Lin et al., 2017); air pollution (Zhu et al., 2020a); human comfort and health (Schwarz et al., 2011); ecosystem function (Keeratikasikorn & Bonafoni, 2018a); is a significant factor of rise in the rate of COVID-19 cases (Li et al., 2020a; Mukherjee & Debnath, 2020) and leads to heat-related deaths (Cui & De Foy, 2012; Lowe, 2016). UHI is measured based on air temperature, while satellite-derived Land Surface Temperature (LST) data has been used to conduct the surface UHI (SUHI). LST is described as the surface temperature of the Earth's skin, playing an important role in the interchange of heat and energy among land surfaces and the atmosphere to assess changes in the environment (Moradi et al., 2018).

Distinct mitigation initiatives such as social distancing, cluster and whole lockdowns, comprehensive travel bans, mass quarantines, and so on have been introduced globally to prevent the COVID-19 pandemic risk. Such risk mitigation initiatives have had a significant effect on socio-political ties and economic

development at local and global levels (Ranjan et al., 2020a). Nevertheless, due to the reduction of anthropogenic-based pollutants, such precautionary strategies to prevent COVID-19 transmission have significantly enhanced air quality. The most critical challenge in the 21st century is the degradation of air quality worldwide due to the different sorts of anthropogenic interventions (Mehdipour & Memarianfard, 2017; Motesaddi et al., 2017). At such a moment, lockdown incidents enforced by the COVID-19 pandemic pressured the anti-environmental activities to cease. Resultantly, throughout the pandemic situation, the level of air quality in the various continents of the Earth is significantly enhanced. In this sense, Tobías (2020) recorded a 45%, 51%, 31% and 19% decline in the level of PM_{10}, NO_2, SO_2, and CO, respectively, over Barcelona in Spain within the lockdown span of a month. Owing to industrial lockdown, Isaifan (2020) recorded a substantial decrease in NO_2 and carbon emissions (30% and 25%, respectively) in China. During the lockdown, Karuppasamy et al. (2020) documented a 55% contraction in NO_2 in India. A recent analysis in the Middle East has also shown a decrease in the number of air pollutants in Morocco of 75%, 49%, and 96% for PM_{10}, SO_2, and NO_2, individually (Otmani et al., 2020). Moreover, in Iran, Nemati et al. (2020) recorded noticeable advancement in the time of pandemic in air pollution. Likewise, during the COVID-19 pandemic, many other recent studies have shown a significant decline in the level of air pollutants such as NO_2, SO_2, PM_{10}, $PM_{2.5}$, CO, and so on, globally (Archer et al., 2020; Collivignarelli et al., 2020; Dantas et al., 2020; Islam et al., 2020; Kaplan & Avdan, 2020; Kerimray et al., 2020; Nakada & Urban, 2020; Ranjan et al., 2020a; Wang & Su, 2020).

The aforementioned studies concentrate primarily on evaluating the level of air pollutants during the pandemic scenario of COVID-19. Although a considerable correlation between air pollutants and LST has been identified in some research

(Alseroury, 2015; Feizizadeh & Blaschke, 2013; Hashim & Sultan, 2010; Kahya et al., 2016; Weng & Yang, 2006), the SUHI variability during the pandemic scenario has not yet been investigated. Like other nations, from the 1st April to the end of June 2020, COVID-19 forced to shut down industries, public transit, airlines, vehicles, and other anthropogenic operations in all Emirates in the UAE and had imposed a curfew daily between 8 pm and 6 am (www.mediaoffice.abudhabi). Therefore, since it is associated with the level of emissions, it is expected that the full or partial lockdown will lead to improved air quality and reduce the SUHI. However, no studies on the impacts of COVID-19 on air quality and SUHI throughout the UAE have been conducted. Consequently, the current study has been undertaken to investigate the potential impacts of COVID-19 lockdown operations on NO_2, Aerosol Optical Depth (AOD), and SUHI in the Northern Emirates of the UAE (NEUAE). The study also aims to validate satellite data over the study area using ground station records. Concentrating on NEUAE, this work is supposed to be a clear complement to evaluating the impact of lockdowns on air quality and SUHI by the science community and environmental protection policymakers, as well as its usefulness as a basic substitute action plan to improve air quality and SUHI.

6.2 Data and Methods

6.2.1 Study Area

The United Arab Emirates (UAE) consists of seven federation Emirates (states): Abu Dhabi (ADH), and six northern Emirates, including Ras Al Khaymah (RAK), Dubai (DUB), Umm Al Qaywayn (UMQ), Sharjah (SHJ), Fujayrah (FUJ), and Ajman (AJM) (Figure 6.1a). The Northern Emirates of the UAE (NEUAE) were chosen as a study area located at approximately between latitudes 26° 365 to 26° 335

N and longitudes 54° 530 to 56° 240 E. Topography of the study area is mostly flat, with a mountain chain reaching an altitude of ~1800 m in the Northeastern and Eastern parts (Figure 6.1b). The NEUAE is typically an arid region with a humid environment, located in the Arabian Peninsula's Eastern corner. It borders the Arabian Gulf to the north, the Gulf of Oman to the east (Figure 6.1). The annual average of air temperature is about 28°C. It is much hotter (approximately 45°C) in the summer season (June to August) and colder (December to February) to 10°C in the winter season. In the hot months, dust storms generally occur (Barbulescu & Nazzal, 2020). Moreover, during the winter season, over 80% of the yearly rainfall occurs (FAO, 2008).

Around 71% bulk of the UAE population is based in the NEUAE. Around 50% of the population resides in DUB, followed by SHJ by 31%, and only 1% resides in UMQ, as per the Federal Competitiveness and Statistics Authority (www.fcsa.gov.ae). Besides that, as documented by the United Nations (2019), more than 86.5% of the people live in urban areas situated on the coastline (Figure 6.1c). Furthermore, over the past two centuries, fast and pervasive economic and political change has caused the increased population explosion, accelerated urbanization, higher energy consumption, and emission of vehicular and industrial. That adds to anthropogenic activities being increased.
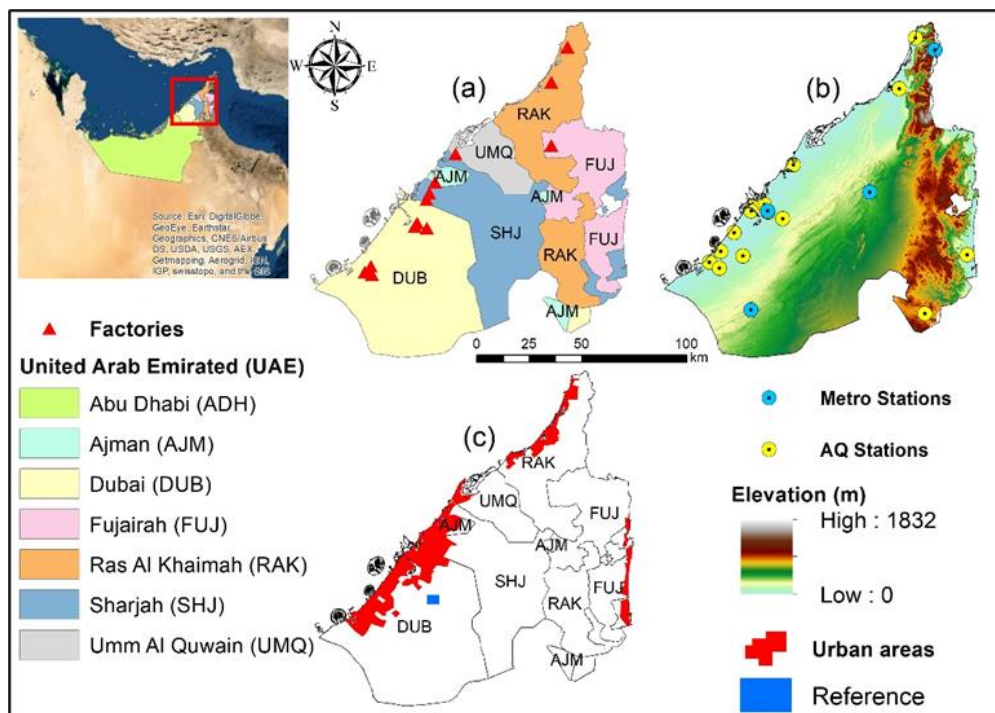
Figure 6.1: Location map of the study area. (a) study area and major factories, (b) elevations and spatial distribution of meteorological and air quality stations, (c) urban areas, and reference

6.2.2 Data

Between March to June 2019 and 2020, two different air pollutants NO_2 and AOD, and night LST data were collected for the NEUAE. The average monthly NO_2 and AOD data have been acquired from Google Earth Engine (GEE). NO_2 is produced by the Sentinel-5p TROPOMI (Tropospheric Monitoring Instrument) mission of Copernicus ESA. While AOD and night LST were obtained by MODIS MAIAC (MCD19A2) and MODIS Aqua (MYD11A2), respectively. Due to the finite temporal scope of Sentinel-5p data, it is worth noting that the baseline was 2019. A summary of the datasets used in this study is shown in Table 6.1.

Table 6.1: Summary of the datasets used in this study

Data source	Parameter	Spatial resolution	Temporal resolution	Data access link
Sentinel5p TROPOMI	NO_2	3.5 x 5 km	daily	https://scihub.copernicus.eu/
MODIS MAIAC	AOD	1 x1 km	daily	https://lpdaac.usgs.gov/
MODIS/ AQUA	Night LST	1x1 km	8-day	https://lpdaac.usgs.gov/
SRTM	DEM	30 x 30m	-	https://earthexplorer.usgs.gov/
NCM	NO_2 & $PM_{2.5}$	-	Monthly	-
DM	Ta_{min}	-	Monthly	-

6.2.2.1 TROPOMI/Sentinel-5p Data (NO_2)

TROPOMI was launched on 13th October 2017 as a passive hyperspectral nadir-viewing imager aboard the Sentinel-5 Precursor satellite, which is also recognized as Sentinel-5P (Veefkind et al., 2012). Sentinel-5P is a near-polar orbiting sun-synchronous satellite positioned at an altitude of 817 km in an ascending node with an equator crossing time at 13:30 (local time) offering daily worldwide coverage. Furthermore, since July 2018, TROPOMI delivered calibrated data from its nadir-viewing spectrometer that measures reflected sunlight in the ultraviolet, visible, near-infrared, and shortwave infrared with seven bands, where the fourth band spectral range is 405-500 nm, which could be used for NO_2 monitoring (Venter et al., 2020). Recent works have shown that measurements of TROPOMI are quite well associated with actual ground measures of NO_2 (Griffin et al., 2019; Lorente et al., 2019). TROPOMI products included in this research are L3 offline version products. Band

four's spectral and spatial resolutions are 0.55 nm and 5.5 x 3.5 km, respectively, and the signal to noise ratio is also massively enhanced (Cheng et al., 2019).

6.2.2.2 MODIS Data (AOD and LST)

In a near-polar solar-synchronous circular orbit, Moderate Resolution Imaging Spectroradiometer (MODIS) was launched onboard NASA's Aqua and Terra satellites. Note that local crossing times are approximately 01:30 and 13:30 for Aqua satellite, while 10:30 and 22:30 for the Terra satellite. MODIS has a 2330 km (cross-track) swath and provides near-global coverage on a daily basis. MODIS is an imaging radiometer with 36 wavebands, covering the wavelength spectrum from the visible to the thermal infrared. AOD data was possessed from the cloud-masked MCD19A2-v6 product, that is a MODIS Terra, and MODIS Aqua combined AOD retrieved with the Multi-Angle Implementation Atmospheric Correction (MAIAC) algorithm (Lyapustin et al., 2018). To map ground-level $PM_{2.5}$ concentrations, this dataset has been used effectively (Wei et al., 2019). Also, in the current analysis, AOD at 550 nm (green band) was utilized because of its superior accuracy (Lyapustin & Wang, 2018). Concerning night LST data, for 2019 and 2020, MODIS Aqua's MYD11A2-v6 performance entails an 8-day composite of LST data at night from 1 March to 30 June 2019 and 2020. In the long time series, the 8-day LST composite products will undervalue the quantity of gaps created by clouds or other unwanted circumstances, that are beneficial for SUHI studies to conduct a spatial comparison (Hu & Brunsell, 2013; Schwarz et al., 2011). Modern Time LST products (v6) have resolved past version accuracy issues, also measure errors and validation assessments in bare land and arid regions currently suggest their use in these areas (Lu et al., 2018b). For the present work, MAIAC AOD and night LST data on a 1 km nadir resolution were

retrieved from the NASA Land Processes Distributed Active Archive Center (https:/lpdaac.usgs.gov/analysis/).

6.2.2.3 SRTM Data (DEM)

The area's topography is predominantly plain, and the elevation slowly increased from north-west to south-east and east, reaching approximately 1830 m (Figure 6.1b), accompanied by the Digital Elevation Model (DEM) 30 m resolution, obtained from the Shuttle Radar Topography Mission (SRTM). The SRTM DEM data was downloaded from the USGS Earth Explorer (https:/earthexplorer.usgs.gov/) to pick a suitable reference location for SUHI calculation.

6.2.2.4 Meteorological Data

The air quality and meteorological records utilized in this study were collected from the Municipality of Dubai (DM) and the National Center of Meteorology (NCM) for validation. From the aforementioned sources, three parameters were obtained: NO_2, $PM_{2.5}$, and minimum air temperature (Ta_{min}) for each of the years 2019 and 2020, from March to June. It is worthwhile to mention that Ta_{min} has been chosen due to matching with MODIS night LST overpass time, which is closer to Ta_{min} (Alqasemi et al., 2020). Likewise, $PM_{2.5}$ has been selected as AOD is considered as a proxy for $PM_{2.5}$ (Fan et al., 2020; Venter et al., 2020).

6.2.3 Methods

6.2.3.1 Data Pre-processing

Usually, the products MCD19A2 and MYD11A2 were available in sinusoidal grid projection that was re-projected to the geographic coordinate system of WGS

1984. In addition, a mosaic of two tiles was created with MYD11A2 data. The scale factor has been multiplied by both MCD19A2 and MYD11A2. Then, 273.15 was subtracted to produce a night LST in Celsius from Kelvin. In the process of producing a seamless dataset, every unrealistic LST data with values above than 100ºC and/or below than -50ºC or any value outside the acceptable range was labelled as no data and ignored, only reliable pixels and high-quality data were used as per the layer of Quality Assessment (QA). Besides, using the mean value of each series, any missing values were amended. Afterward, night LST data was aggregated to a monthly period by averaging the 8-day composite data to obtain monthly average night LST. As for TROPOMI-Sentinel-5P NO_2 was resampled to (1x1 km) to ensure conformity with a spatial resolution of MODIS data (i.e., AOD and night LST). Then, the boundary polygon that defined the study area was used to clip all datasets.

Finally, as a preventive strategy for COVID-19, the three months of April, May, and June (AMJ) were averaged as one period applied for all datasets throughout the NEUAE. Furthermore, March month was collected and processed for pre-lockdown in 2020 for NO_2, AOD, and night LST. Similarly, for the identical time spans as the lockdown and pre-lockdown periods, the mean of datasets was obtained for 2019 for comparative analysis, as well as utilized for evaluating the correlation with measured data from ground stations.

6.2.3.2 SUHI Calculation

The night SUHI is a distinctive feature of arid regions, as per number of researchers (Alahmad et al., 2020; Clinton & Gong, 2013; Lazzarini et al., 2013). Additionally, the lowest surface temperature is reported at midnight, making Aqua night data an optimal choice near the SUHI maxima. SUHI is typically measured from

the LST contrasts between urban and surrounding areas (will be cited here as reference). Consequently, choosing a reliable reference is important. In different tests, however, the approaches for determining the reference differed extensively in various studies. The reference should not be influenced by urban, high altitude, vegetation or water (Hu et al., 2019b). Therefore, in this study, the reference was defined as bare land using chronological imaged from Google Earth Pro (GEP) and lower than 50 m relying on the 30 m DEM dataset to prevent the cooling effect on the SUHI quantification. Finally, by subtracting the average night LST of the reference from the night LST of all pixels, the SUHI was calculated by every pixel utilizing the following equation (Equation 6.1)

$$SUHI = LST_{PX} - LST_{RF} \qquad\qquad (6.1)$$

where LST_{PX} is the night LST of all pixels, and LST_{RF} is the mean night LST of the reference.

6.2.3.3 Change Rate (Concentration)

It is critical to understand the alteration in the NO_2, AOD, and SUHI concentrations throughout the lockdown period. After retrieving the data on pollutants and SUHI, the Spatio-temporal pattern of average levels of NO_2, AOD, and SUHI is categorized into four groups; (i) pre-lockdown (March 2020); (ii) during the lockdown period (AMJ, 2020); (iii) the same Pre-lockdown dates (March 2019); (iv) the same 2019 lockdown dates. Furthermore, the change rates were calculated utilizing Equation 6.2 to reflect the percentage of change in the study area's NO_2, AOD, and SUHI levels during the lockdown period related to the past year (i.e., 2019) for the same time span, and also compared to pre-lockdown in March 2020. The change rate of variation between March and AMJ throughout 2019 and 2020 is also put into account.

$$\text{Change rate (\%)} = ((X2020 - X2019) / X2019) * 100 \qquad (6.2)$$

Where, X is NO_2, AOD, or SUHI for the selected periods in 2019 and 2020. In addition, the agreement will be analyzed by calculating the regression coefficients (R^2) among stations and satellite data based on the availability of the metrological and air quality station data. The flowchart for the methodological workflow is presented concisely in Figure 6.2. The sequence of data collection, pre-processing, clipping, resampling, data extractions, and SUHI measurement, change rate, and validation are described in Figure 6.2. For the processing, analysis, and exhibition, the ESRI ArcGIS™ version 10.4 software framework and Microsoft Office Excel were used.
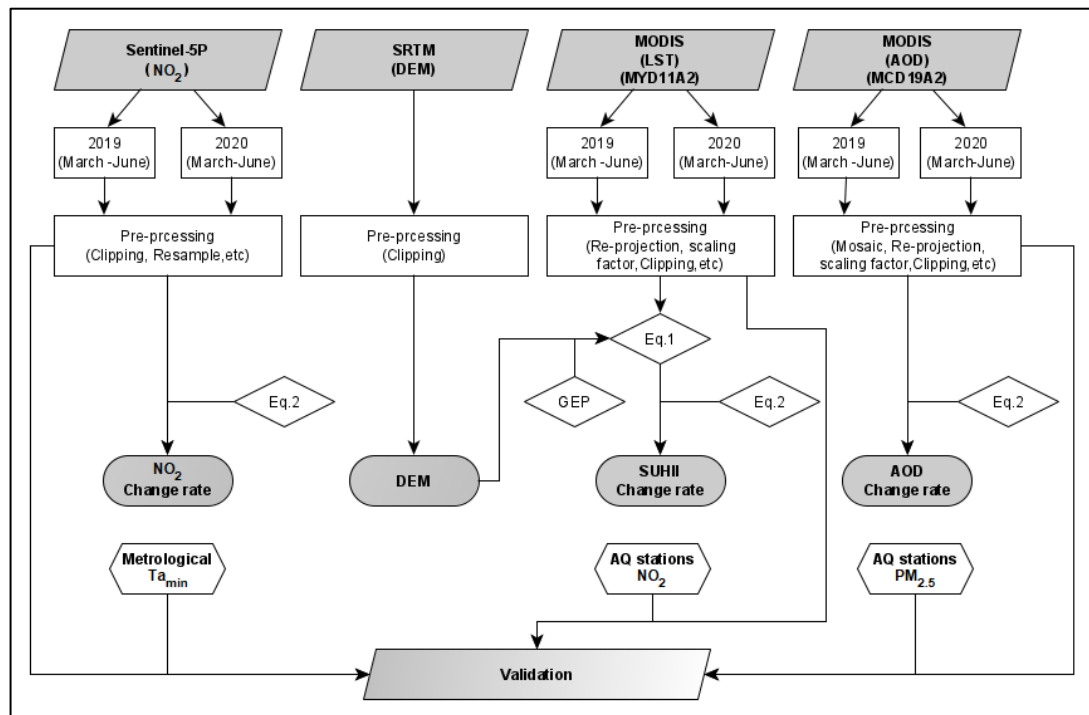
Figure 6.2: Workflow flowchart adopted in the present study

6.3 Results and Discussions

6.3.1 Nitrogen Dioxide (NO_2)

A dramatic drop in NO_2 concentration was recorded during the lockdown period (i.e., AMJ, 2020) in NEUAE due to the COVID-19. Figure 6.3 depicts the substantial spatiotemporal changes in NO_2 levels throughout lockdown and pre-lockdown in NEUAE. The analysis showed that because of restricted transportation and factories' closure, the six Emirates experienced a decline in NO_2 levels. This result is compatible with other earlier studies undertaken in various regions of the globe (Baldasano, 2020; Dantas et al., 2020; Islam et al., 2020; Kaplan & Avdan, 2020; Sharma et al., 2020). Figure 6.4 indicates that RAK noted the highest decline in NO_2 levels among the six Emirates (18.5%), followed by UMQ (~18%), AJM (13%), and FUJ (11.6%) compared with the average NO_2 levels throughout lockdown with the average levels instantly pre-lockdown, for other Emirates relative to DUB (7.5%) and SHJ (5.4%). In addition, this study indicates that, as shown in Figure 6.4, the average decline in NO_2 concentration throughout NEUAE was substantial 12.2%. This decline should be noted that NO_2 emission is closely connected to fuel combusting within the factories area (Figures 6.1a & 6.3). Therefore, the limitations on these areas operations are supposed to result in a substantial drop in NO_2 level throughout the lockdown period. Additionally, within March 2019, NO_2 level was lower than March 2020, as shown in Figure 6.3a and c, that may be due to the precipitation during March 2019.

A substantial decrease in NO_2 is reported in the study area by comparing the NO_2 amount of lockdown period 2020 with an identical period in 2019. The maximum decline was for UMQ (27.8%) followed by RAK (26.8%), SHJ (~26%), FUJ (24.3%), AJM (19.8%) and DUB (18.7%). With the whole study area, the average reduction

was 23.7%, as presented in Figure 6.4. These results are in accordance with the results of the previously published research. Islam et al. (2020) recorded identical outcomes for Bangladesh during the lockdown period as opposed to the same period in 2019. Agarwal et al. (2020) recorded an average reduction in NO_2 during the lockdown in China by 49% and in Mumbai (India) by more than 76%. In the Middle East (Morocco), NO_2 levels were decreased during the lockdown phase compared with the identical period in 2019 (Sekmoudi et al., 2020).

In brief, this decline in NO_2 concentrations at various periods shows that lockdown initiatives related to the COVID-19 pandemic significantly impacted changing NO_2 concentrations in NEUAE.

Figure 6.3: Spatiotemporal distribution of average NO$_2$ over NEUAE. (a) March 2019, (b) average AMJ 2019, (c) pre-Lockdown (March 2020), (d) during Lockdown (AMJ 2020), (e) percentage of change between March 2019 and 2020, and (f) percentage of change between average AMJ 2019 and 2020

	AJM	DUB	FUJ	RAK	SHJ	UMQ	NEUAE
Change rate (Lockdown)	-19.787	-18.729	-24.258	-26.765	-25.889	-27.829	-23.663
Change rate (March&AMJ, 2019)	34.239	37.748	23.212	35.663	18.884	33.933	30.557
Change rate (March&AMJ, 2020)	-12.986	-7.546	-11.584	-18.560	-5.418	-17.945	-12.235

Figure 6.4: Average NO_2 concentration at NEUAE before and during lockdown

6.3.2 Aerosol Optical Depth (AOD)

The same as NO_2, a significant decline in AOD concentration was recorded, as shown in Figure 6.5. Likewise, for the same period, the average AOD values during the lockdown period were lower than the mean AOD values in 2019. The analysis indicates that all six Emirates encountered a decline in AOD concentration because of restricted aerosol sources. Primarily from burning biomass, emissions from factories, vehicles, heavy transport, and machinery (Ranjan et al., 2020b), and dust (Khuzestani et al., 2017). Therefore, a reduction in AOD due to the restrictions of industrial and automobile movement is reasonable. For the specified time frames, the spatiotemporal variations in AOD concentrations in NEUAE are depicted in Figure 6.5. AJM with 5.7% and UMQ with 5.3% were the largest declines, accompanied by SHJ with 3.4%, FUJ, and RAK, both with 3.1%. In Dubai, the lowest drop was 1.7%. The rate of change was 3.7% throughout the overall study area (NEUAE), as shown in Figure 6.6. Similarly, a common declining trend of AOD has been recorded in China (Fan et al., 2020; Filonchyk et al., 2020), India (Gautam, 2020; Pathakoti et al., 2020; Ranjan et al., 2020b), and South Asia (Zhang et al., 2020).

During the average AMJ, the level of AOD increased significantly compared to March (Figure 6.5). Owing to this, rainfall throughout these months (AMJ) is scarce, but the gusty winds ensure that dust storms become frequent (Barbulescu & Nazzal, 2020; Karagulian et al., 2019). Furthermore, according to Al Otaibi et al. (2019), AOD typically rises over the gulf nations in hot summer months. Consequently, in general, rises in the AOD level in AMJ comparing to March were observed. However, the change rate between March and the average AMJ in 2020 decreased relative to the past year for all six Emirates, as shown in Figure 6.6. In 2019, the change rate ranged from 16.3% to 34%, whereas it dropped in 2020 from -0.7% to around 7%. Notably, AOD emission is linked with the major industries, particularly in Dubai (Figures 6.1a, 6.5 & 6.6). Further, Dubai has a minimum reduction in AOD. The most populous and established region of the UAE is the Emirate of Dubai, and also the most famous industrialized regions are in Dubai. It is believed, therefore, that certain considerations may be behind for the least reduction.
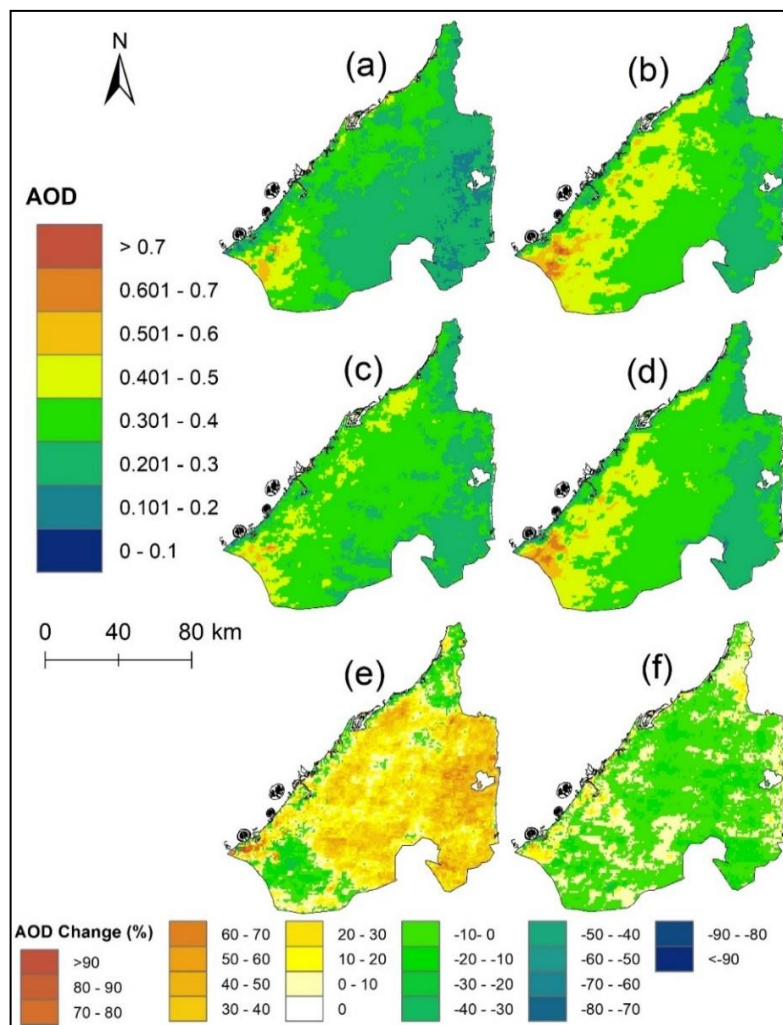
Figure 6.5: Spatiotemporal distribution of average AOD over NEUAE. (a) March 2019, (b) average AMJ 2019, (c) pre-lockdown (March 2020), (d) during lockdown (AMJ 2020), (e) percentage of change between March 2019 and 2020, and (f) percentage of change between average AMJ 2019 and 2020

	AJM	DUB	FUJ	RAK	SHJ	UMQ	NEUAE
Change rate (Lockdown)	-5.673	-1.713	-3.139	-3.108	-3.397	-5.268	-3.705
Change rate (March&AMJ, 2019)	26.020	24.617	34.620	16.253	33.966	24.416	26.299
Change rate (March&AMJ, 2020)	0.758	13.224	-0.680	-1.050	6.927	1.426	3.642
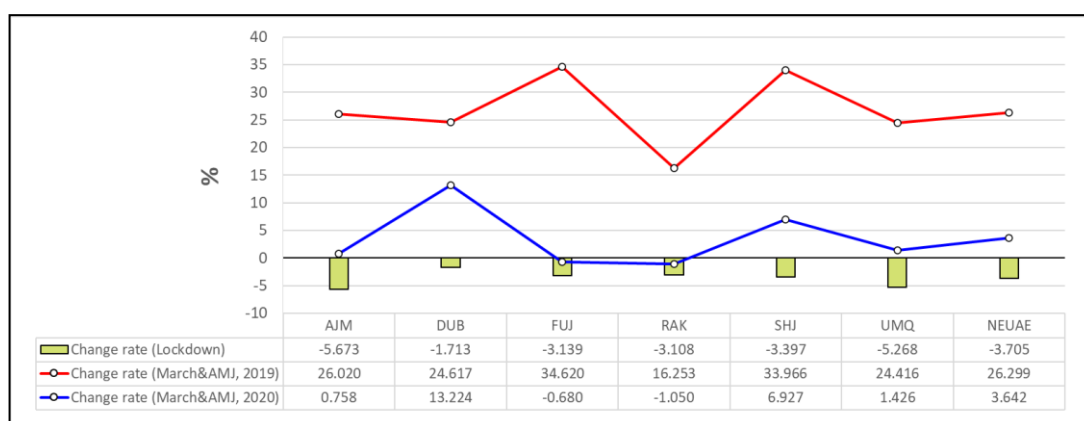
Figure 6.6: Average concentrations of AOD at NEUAE before and during lockdown

6.3.3 Surface Urban Heat Island (SUHI)

SUHI specifically portrays urbanized areas and mountains, as shown in Figure 6.7(a-d). A drop in SUHI levels has also been recorded, like NO_2 and AOD (Figure 6.7f), due to the partial or full nationwide lockdown. The result reveals that during the specific time frame, nighttime SUHI levels over this duration were comparatively less than the 2019 levels (Figures 6.7 & 6.8). The decline has generally been identified in all Emirates, varying from 12.3% to 28.6%, in which the average drop is 19.2% across the whole study area.

Furthermore, the maximum SUHI concentrations are found in FUJ (28.6%) and RAK (23%) as displayed in Figure 6.8, which may be due to the elevations and type of rocks. Figure 6.7 (a-d) also reveals that SUHI increases during AMJ relative to March, owing to heat emission in hot months (e.g., air conditioning system). Nevertheless, the change rate in 2020 between March and lockdown months (AMJ) is less than in 2019. It dropped from 18.3% in 2019 to 6.6% in 2020, as exhibited in Figure 6.8. Overall, the results indicate a reduction in SUHI values owing to the shutdown of anthropogenic activities and sources of heat emissions, like industrial processes, power plants, flight, and transport.
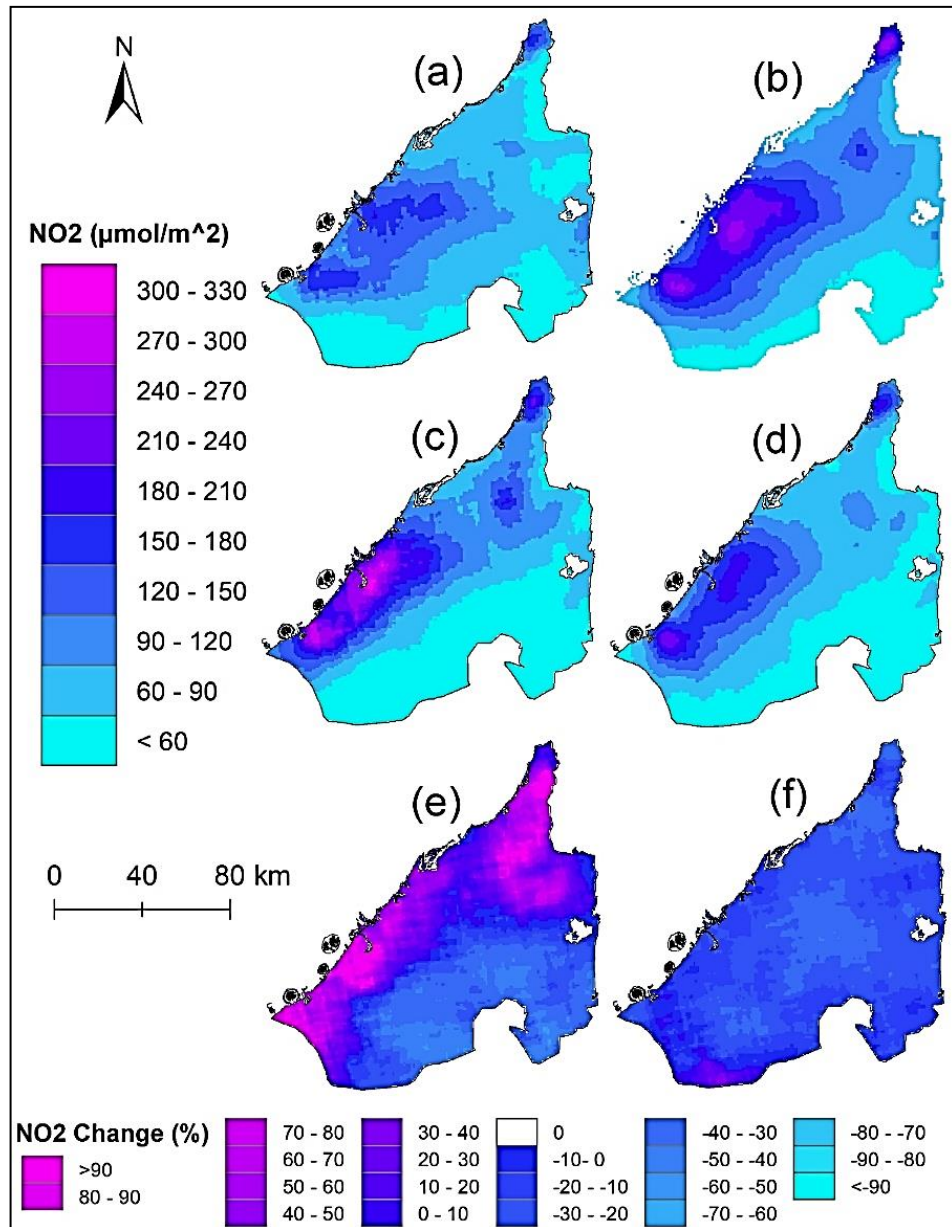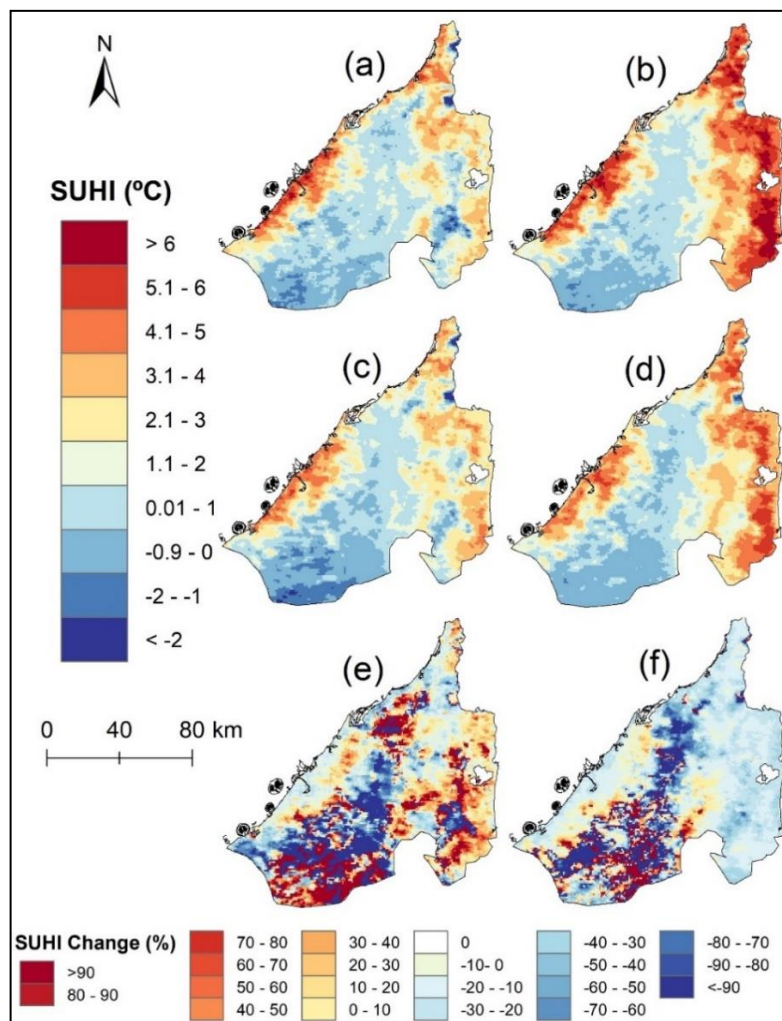
Figure 6.7: Spatiotemporal distribution of SUHI over NEUAE. (a) March 2019, (b) average AMJ 2019, (c) pre-Lockdown (March 2020), (d) during Lockdown (AMJ 2020), (e) percentage of change between March 2019 and 2020, and (f) percentage of change between average AMJ 2019 and 2020
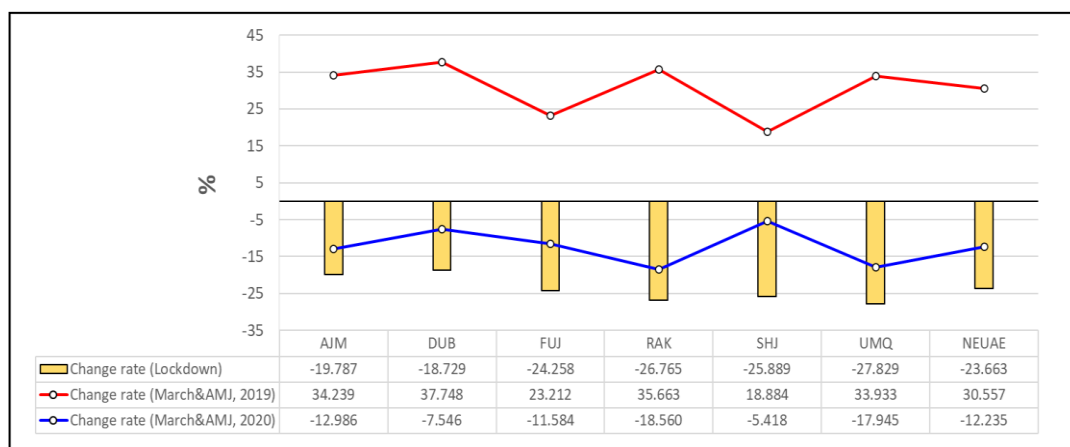

	AJM	DUB	FUJ	RAK	SHJ	UMQ	NEUAE
Change rate (Lockdown)	-12.302	-14.928	-28.588	-22.976	-17.349	-18.861	-19.222
Change rate (March&AMJ, 2019)	12.327	11.157	87.512	9.678	15.501	-6.435	18.320
Change rate (March&AMJ, 2020)	3.291	6.451	30.998	5.486	4.171	-7.565	6.649
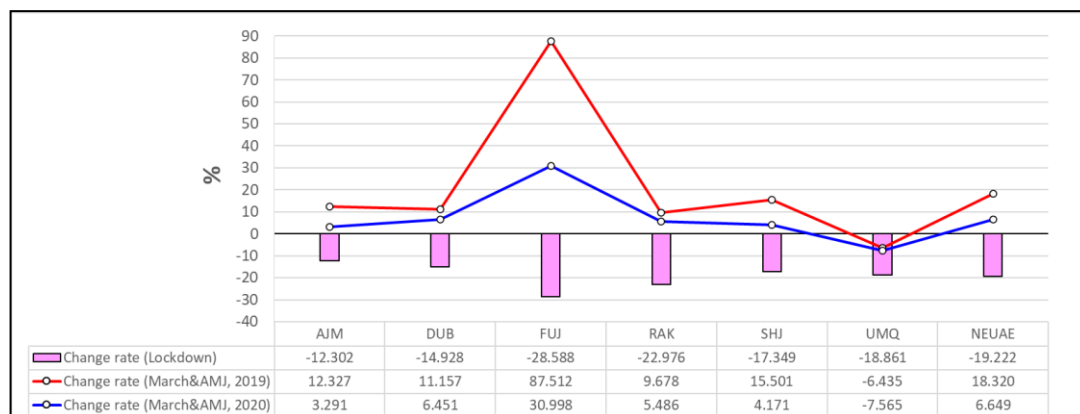
Figure 6.8: Average concentrations of SUHI at NEUAE before and during lockdown

6.3.4 Validation

In this section, the validations of derived data from satellites with the measured data from actual ground stations are investigated. The comparisons consisting of derived NO_2, AOD, and night LST plotted against the measured data NO_2, $PM_{2.5}$, and minimum air temperature (Ta_{min}), respectively, as presented in Figure 6.9. Based on the availability of ground stations data, the validation of the NO_2 and $PM_{2.5}$ data have been made using thirteen and five air quality monitoring stations measurements, respectively, from Mach to June 2019. Whereas Ta_{min} data covers the whole period (March-June) in 2019 and 2020 at four metrological stations (Figure 6.1b). It is noteworthy to mention that, due to the fact that the Aqua satellite crossing the equator at night close to the Ta_{min}, it was decided to validate night Aqua LST data with Ta_{min}. In addition, as mentioned before, the AOD is considered as a proxy for ($PM_{2.5}$); thus, AOD is plotted versus $PM_{2.5}$.

These comparisons show that the TROPOMI Sentinel-5P NO_2 is highly correlated with the air quality monitoring stations data with $R^2 = 0.70$, as shown in Figure 6.9a. Likewise, Figure 6.9b shows the scatter plot of measured $PM_{2.5}$ versus MODIS MAIAC AOD. The statistical analyses showed a moderate coefficient of determination ($R^2 = 0.60$). Further, the high agreement was also found between the MODIS Aqua night LST and the Ta_{min} from stations measurements ($R^2 = 0.68$), as displayed in Figure 6.9c. Overall, the high agreement is found between satellite data and actual measured data; hence, the satellite observations are a tremendous resource for studying air pollution and SUHI over large geographic regions.
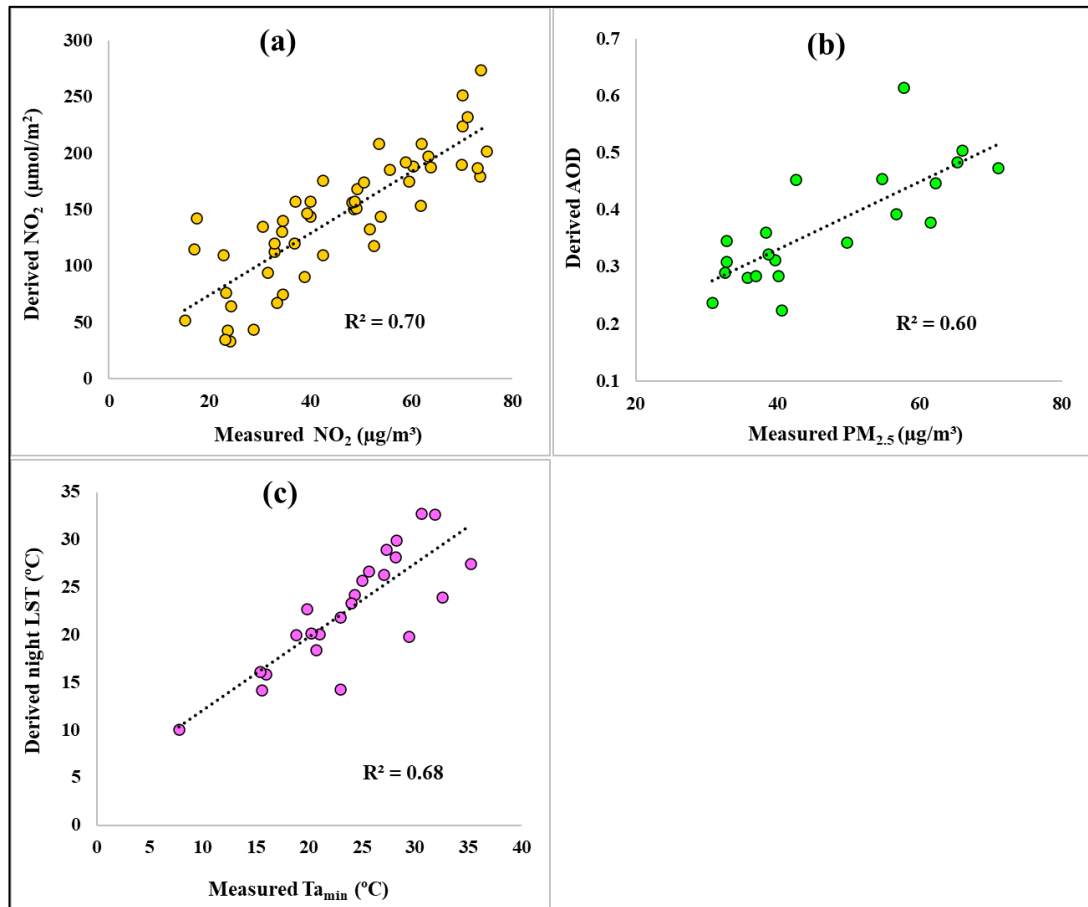
Figure 6.9: The scatter plots of validation for the derived data from satellites and measured data from ground-measuring stations. (a) measured NO_2 and derived NO_2, (b) measured $PM_{2.5}$ and AOD, and (c) minimum air temperature (Tamin) and night LST

6.4 Conclusions

The COVID-19 pandemic has become a significant threat to public health, together with a massive economic loss around the world. The lockdown sparked by the COVID-19 pandemic, however, showed that if a chance is given by society, nature will cure itself. The impact of anthropogenic activities lockdown due to the COVID-19 pandemic on air quality and SUHI in NWUAE was studied by examining NO_2, AOD, and SUHI levels and evaluating variations in spatial distribution. To demonstrate how restrictive anthropogenic activities throughout the COVID-19

lockdown minimized the air pollutants and SUHI in NEUAE, satellite data of different parameters were used in 2019-2020. As predicted, the current investigation discovered that NO_2, AOD, and SUHI concentrations across the NEUAE have been decreased due to the pandemic lockdown. The largest average drop was in NO_2 (23.7%) followed by SUHI (19.2%) and AOD (3.7%) throughout the lockdown period compared with the same period in the year 2019.

Furthermore, the largest average reduction among March and average lockdown months in years 2019 and 2020, was NO_2 followed by AOD. The study also identified that the selected air pollutants and SUHI data are highly correlated with the actual measured data. Therefore, satellite data is a tremendous and reliable resource for researching air quality and SUHI, especially for developing countries like the UAE. In conclusion, this study has established a benchmark paradigm that will potentially assist the authorities concerned with the potential management of air quality and SUHI in the UAE by decision-makers, particularly on industrial and vehicle pollution restrictions. The drawbacks of this work are that some data from ground stations was incomplete. Besides, the baseline was a single year (i.e., 2019) due to the limited temporal scale of TROPOMI/ Sentinel-5P data, and therefore the outcomes may change slightly when providing extra data. Further study is recommended considering the correlation of air pollutants and SUHI with COVID-19 cases in the UAE.

Summary

The thermal infrared measurements calculated by the satellite were used to estimate Land Surface Temperature (LST). LST's extensive requirements for diverse applications of the Earth's resources formed LST's remote sensing a vital component of research. In this dissertation, some essential applications of MODIS LST over the United Arab Emirates were discussed and summarized in the following section.

❖ The first application of LST illustrates the utilization of satellite-based measurements for thermal anomaly detection from the TRMM, MODIS, and Bouguer gravity, demonstrating the ability of satellite LST to observe these anomalies in order to discover ideal groundwater resources.

❖ In the second application, using spectral indices and field measurements, soil salinity was estimated. Statistical analysis of the combined data demonstrates that the NDVI and BSI had the highest correlation of all indices. Night MODIS LST also gives a good correlation with soil salinity over western of the Abu Dhabi.

❖ The third application presented in this dissertation used MODIS Aqua products to obtain maximum and minimum air temperature (i.e., T_{max} and T_{min}) over the UAE. The linear regression approach was used for T_{max} and T_{min} estimation. T_{max} and T_{min} were successfully retrieved through regression analysis between daytime and night-time MODIS LST, respectively, and meteorological station measurements over all stations. The MODIS LST data proved to be a reliable proxy for air temperature and mostly for studies requiring temperature reconstruction in areas with a lack of observational stations.

❖ In the fourth application, MODIS LST was used to study the SUHI phenomena for Dubai city in the UAE. Temporal variability of satellite-derived LST over the urban and surrounding nonurban area were analyzed for 2003-2019. The night SUHI starts rising gradually with the development of the city and population growth.

❖ In the fifth application, the MODIS LST has been used to extract night SUHI to investigate the impact COVID-19 lockdown event on SUHI and selected air pollutants such as NO_2 and AOD over northern emirates of the UAE. Agreement between satellite data and ground stations also was evaluated. All parameters were reduced during the lockdown over the study area.

References

Abbas, M. R., Ahmad, B. Bin, & Abbas, T. R. (2015). Use MODIS satellite data to study new phenomena of underground fire in the Al Ruhban oasis in Al Najaf city, Iraq. *Environmental Earth Sciences*, *73*(7), 3475–3485. https://doi.org/10.1007/s12665-014-3632-8

Abuelgasim, A., & Ammad, R. (2017). Mapping Sabkha Land Surfaces in the United Arab Emirates (UAE) using Landsat 8 Data, Principal Component Analysis and Soil Salinity Information. *International Journal of Engineering and Manufacturing*, *7*(4), 1–11. https://doi.org/10.5815/ijem.2017.04.01

Abuelgasim, A., & Ammad, R. (2019). Mapping soil salinity in arid and semi-arid regions using Landsat 8 OLI satellite data. *Remote Sensing Applications: Society and Environment*, *13*, 415–425.

Agarwal, A., Kaushik, A., Kumar, S., & Mishra, R. K. (2020). Comparative study on air quality status in Indian and Chinese cities before and during the COVID-19 lockdown period. *Air Quality, Atmosphere & Health*, *13*(10), 1167–1178. https://doi.org/10.1007/s11869-020-00881-z

Akbar, N. A., Mehdi, H., & Farshad, A. (2011). Integrated application of remote sensing and spatial statistical models to the identification of soil salinity: A case study from Garmsar Plain, Iran. *Environmental Science*, *8*(1), 59–74.

Al-Khaier, F. (2003). Soil salinity detection using satellite remote sensing. *ITC*.

Al-Mhaidib, A. (2003). Sabkha soil in the Kingdom of Saudi Arabia: characteristics and treatment. *Arts and Humanities*, *14*, 29–80.

Al Otaibi, M., Farahat, A., Tawabini, B., Omar, M. H., Ramadan, E., Abuelgasim, A., & P. Singh, R. (2019). Long-Term Aerosol Trends and Variability over Central Saudi Arabia Using Optical Characteristics from Solar Village AERONET Measurements. *Atmosphere*, *10*(12), 752. https://doi.org/10.3390/atmos10120752

Alahmad, B., Tomasso, L. P., Al-Hemoud, A., James, P., & Koutrakis, P. (2020). Spatial distribution of land surface temperatures in Kuwait: Urban heat and cool Islands. *International Journal of Environmental Research and Public Health*, *17*(9), 1–11. https://doi.org/10.3390/ijerph17092993

Alali, A. M. (2015). *The Effect of Land Cover on the Air and Surface Urban Heat Island of a Desert Oasis* [Durham University]. http://etheses.dur.ac.uk/11290/

Alam, H., Khattak, J. Z. K., Ppoyil, S. B. T., Kurup, S. S., & Ksiksi, T. S. (2017). Landscaping with native plants in the UAE: A review. *Emirates Journal of Food and Agriculture*, *29(10),* 729–741. https://doi.org/10.9755/ejfa.2017.v29.i10.319

Alghamdi, A. S., & Moore, T. W. (2015). Detecting Temporal Changes in Riyadh's Urban Heat Island. *Papers in Applied Geography*, *1*(4), 312–325. https://doi.org/10.1080/23754931.2015.1084525

Allbed, A., Kumar, L., & Sinha, P. (2014). Mapping and Modelling Spatial Variation in Soil Salinity in the Al Hassa Oasis Based on Remote Sensing Indicators and Regression Techniques. In *Remote Sensing* (Vol. 6, Issue 2). https://doi.org/10.3390/rs6021137

Alqasemi, A., Hereher, M., Al-Quraishi, A., Saibi, H., Aldahan, A., & Abuelgasim, A. (2020). Retrieval of monthly maximum and minimum air temperature using MODIS Aqua land surface temperature data over the United Arab Emirates (UAE). *Geocarto International*. https://doi.org/10.1080/10106049.2020.1837261

Alseroury, F. A. (2015). The effect of pollutants on land surface temperature around power plan. *International Journal of Mechanical and Production Engineering, 3,* 17–21.

Alsharhan, A. S., & Kendall, C. G. S. C. (2003). Holocene coastal carbonates and evaporites of the southern Arabian Gulf and their ancient analogues. *Earth-Science Reviews*, *61*(3), 191–243. https://doi.org/https://doi.org/10.1016/S0012-8252(02)00110-1

Alsharhan, A. S., Rizk, Z. A., Nairn, A. E. M., Bakhit, D. W., & Alhajari, S. A. (2001). Aquifer and aquiclude systems. In A. S. Alsharhan, Z. A. Rizk, A. E. M. Nairn, D. W. Bakhit, & S. A. B. T.-H. of an A. R. T. A. G. and A. A. Alhajari (Eds.), *Hydrogeology of an Arid Region: The Arabian Gulf and Adjoining Areas* (pp. 79-99). Elsevier. https://doi.org/10.1016/B978-044450225-4/50005-1

Archer, C. L., Cervone, G., Golbazi, M., Fahel, N. Al, & Hultquist, C. (2020). *Changes in air quality and human mobility in the U.S. during the COVID-19 pandemic*. http://arxiv.org/abs/2006.15279

Asfaw, E., Suryabhagavan, K. V, & Argaw, M. (2018). Soil salinity modeling and mapping using remote sensing and GIS: The case of Wonji sugar cane irrigation farm, Ethiopia. *Journal of the Saudi Society of Agricultural Sciences*, *17*(3), 250–258.

Azevedo, J. A., Chapman, L., & Muller, C. L. (2016). Quantifying the daytime and night-time urban heat Island in Birmingham, UK: A comparison of satellite derived land surface temperature and high resolution air temperature observations. *Remote Sensing*, *8*(2),153. https://doi.org/10.3390/rs8020153

Azhdari, A., & Taghvaee, A. A. (2018). Analysis of the Effect of Land Cover Spatial Configuration and Physical Characteristics of Buildings on the Surface Urban Cool Island Phenomenon. *Journal of Environmental Studies*, *44*(1), 189–203. https://doi.org/10.22059/jes.2018.244458.1007528

Baldasano, J. M. (2020). COVID-19 lockdown effects on air quality by NO2 in the cities of Barcelona and Madrid (Spain). *Science of the Total Environment*, *741*(2), 140353. https://doi.org/10.1016/j.scitotenv.2020.140353

Barat, A., Kumar, S., Kumar, P., & Parth Sarthi, P. (2018). Characteristics of Surface Urban Heat Island (SUHI) over the Gangetic Plain of Bihar, India. *Asia-Pacific Journal of Atmospheric Sciences*, *54*(2), 205–214. https://doi.org/10.1007/s13143-018-0004-4

Barbulescu, A., & Nazzal, Y. (2020). Statistical analysis of dust storms in the United Arab Emirates. *Atmospheric Research*, *231*, 104669. https://doi.org/https://doi.org/10.1016/j.atmosres.2019.104669

Bathurst, R. G. C. (1972). *Carbonate sediments and their diagenesis* (1st ed.). Elsevier.

Benali, A., Carvalho, A. C., Nunes, J. P., Carvalhais, N., & Santos, A. (2012). Estimating air surface temperature in Portugal using MODIS LST data. *Remote Sensing of Environment*, *124*, 108–121. https://doi.org/10.1016/j.rse.2012.04.024

Benas, N., Chrysoulakis, N., & Cartalis, C. (2017). Trends of urban surface temperature and heat island characteristics in the Mediterranean. *Theoretical and Applied Climatology*, *130*(3–4), 807–816. https://doi.org/10.1007/s00704-016-1905-8

Bonafoni, S., Baldinelli, G., Verducci, P., & Presciutti, A. (2017). Remote sensing techniques for urban heating analysis: A case study of sustainable construction at district level. *Sustainability (Switzerland)*, *9*(8). https://doi.org/10.3390/su9081308

Brunner, P., Li, H. T., Kinzelbach, W., & Li, W. P. (2007). Generating soil electrical conductivity maps at regional level by integrating measurements on the ground and remote sensing data. *International Journal of Remote Sensing*, *28*(15), 3341–3361.

Bukhari, Q., & Jameel, Y. (2020). Will Coronavirus Pandemic Diminish by Summer? *SSRN Electronic Journal*, 1–15. https://doi.org/10.2139/ssrn.3556998

Carlson, T. N., & Ripley, D. A. (1997). On the relation between NDVI, fractional vegetation cover, and leaf area index. *Remote Sensing of Environment*, *62*(3), 241–252. https://doi.org/https://doi.org/10.1016/S0034-4257(97)00104-1

Chen, Q.-X., Huang, C.-L., Yuan, Y., & Tan, H.-P. (2020). Influence of COVID-19 Event on Air Quality and their Association in Mainland China. *Aerosol and Air Quality Research*, *20*(7), 1541–1551. https://doi.org/10.4209/aaqr.2020.05.0224

Chen, Y., Sun, H., & Li, J. (2016). Estimating daily maximum air temperature with MODIS data and a daytime temperature variation model in Beijing urban area. *Remote Sensing Letters*, *7*(9), 865–874. https://doi.org/10.1080/2150704X.2016.1193792

Cheng, L., Tao, J., Valks, P., Yu, C., Liu, S., Wang, Y., Xiong, X., Wang, Z., & Chen, L. (2019). NO2 retrieval from the environmental trace gases monitoring instrument (EMI): Preliminary results and intercomparison with OMI and TROPOMI. *Remote Sensing*, *11*(24). https://doi.org/10.3390/rs11243017

Cheval, S., Žák, M., Dumitrescu, A., & Květoň, V. (2014). Modis-Based Investigations on the Urban Heat Islands of Bucharest (Romania) and Prague (Czech Republic), 1-8. http://citeseerx.ist.psu.edu/viewdoc/download?doi=10.1.1.585.4029&rep=rep1&type=pdf

Chuvieco, E. (2009). *Fundamentals of satellite remote sensing*. CRC press.

Clinton, N., & Gong, P. (2013). MODIS detected surface urban heat islands and sinks: Global locations and controls. *Remote Sensing of Environment*, *134*, 294–304. https://doi.org/10.1016/j.rse.2013.03.008

Cohen, S. (2009). *T*he Role of Widespread Surface Solar Radiation Trends in Climate Change: Dimming and Brightening. In *climate change* (pp. 21-41). Elsevier. https://doi.org/https://doi.org/10.1016/B978-0-444-53301-2.00002-6

Collivignarelli, M. C., Abbà, A., Bertanza, G., Pedrazzani, R., Ricciardi, P., & Carnevale Miino, M. (2020). Lockdown for CoViD-2019 in Milan: What are the effects on air quality? *Science of The Total Environment*, *732*, 139280. https://doi.org/https://doi.org/10.1016/j.scitotenv.2020.139280

Conticini, E., Frediani, B., & Caro, D. (2020). Can atmospheric pollution be considered a co-factor in extremely high level of SARS-CoV-2 lethality in Northern Italy? *Environmental Pollution*, *261*, 114465. https://doi.org/https://doi.org/10.1016/j.envpol.2020.114465

Cui, Y., Xu, X., Dong, J., & Qin, Y. (2016). Influence of urbanization factors on surface urban heat island intensity: A comparison of countries at different developmental phases. *Sustainability (Switzerland)*, *8*(8). https://doi.org/10.3390/su8080706

Cui, Y. Y., & De Foy, B. (2012). Seasonal variations of the urban heat island at the surface and the near-surface and reductions due to urban vegetation in Mexico City. *Journal of Applied Meteorology and Climatology*, *51*(5), 855–868. https://doi.org/10.1175/JAMC-D-11-0104.1

Dantas, G., Siciliano, B., França, B. B., da Silva, C. M., & Arbilla, G. (2020). The impact of COVID-19 partial lockdown on the air quality of the city of Rio de Janeiro, Brazil. *Science of The Total Environment*, *729*, 139085. https://doi.org/https://doi.org/10.1016/j.scitotenv.2020.139085

Dash, P., Göttsche, F.-M., Olesen, F.-S., & Fischer, H. (2002). Land surface temperature and emissivity estimation from passive sensor data: Theory and practice-current trends. *International Journal of Remote Sensing*, *23*(13), 2563–2594.

Dehni, A., & Lounis, M. (2012). Remote sensing techniques for salt affected soil mapping: application to the Oran region of Algeria. *Procedia Engineering*, *33*, 188–198.

Deilami, K., Kamruzzaman, M., & Liu, Y. (2018). Urban heat island effect: A systematic review of spatio-temporal factors, data, methods, and mitigation measures. *International Journal of Applied Earth Observation and Geoinformation*, *67*, 30–42. https://doi.org/10.1016/j.jag.2017.12.009

Du, C., Ren, H., Qin, Q., Meng, J., & Zhao, S. (2015). A practical split-window algorithm for estimating land surface temperature from Landsat 8 data. *Remote Sensing*, *7*(1), 647–665.

Duan, S. B., Li, Z. L., Tang, B. H., Wu, H., Tang, R., Bi, Y., & Zhou, G. (2014). Estimation of diurnal cycle of land surface temperature at high temporal and spatial resolution from clear-sky MODIS data. *Remote Sensing*, *6*(4), 3247–3262. https://doi.org/10.3390/rs6043247

Duan, S. B., Li, Z. L., Wu, H., Leng, P., Gao, M., & Wang, C. (2018). Radiance-based validation of land surface temperature products derived from Collection 6 MODIS thermal infrared data. *International Journal of Applied Earth Observation and Geoinformation*, *70*(April), 84–92. https://doi.org/10.1016/j.jag.2018.04.006

El-Baz, F. (2010). Remote sensing: generating knowledge about groundwater. *Arab Enviroment*, 201–222.

El Kenawy, A. M., Hereher, M. E., & Robaa, S. M. (2019a). An assessment of the accuracy of MODIS land surface temperature over Egypt using ground-based measurements. *Remote Sensing*, *11*(20), 2369. https://doi.org/10.3390/rs11202369

El Kenawy, A. M., Lopez-Moreno, J. I., McCabe, M. F., Robaa, S. M., Domínguez-Castro, F., Peña-Gallardo, M., Trigo, R. M., Hereher, M. E., Al-Awadhi, T., & Vicente-Serrano, S. M. (2019b). Daily temperature extremes over Egypt: Spatial patterns, temporal trends, and driving forces. *Atmospheric Research*, *226*, 219–239. https://doi.org/10.1016/j.atmosres.2019.04.030

Eldeiry, A. A., & Garcia, L. A. (2010). Comparison of ordinary kriging, regression kriging, and cokriging techniques to estimate soil salinity using LANDSAT images. *Journal of Irrigation and Drainage Engineering*, *136*(6), 355–364.

Elhag, M. (2016). Evaluation of different soil salinity mapping using remote sensing techniques in arid ecosystems, Saudi Arabia. *Journal of Sensors*, *2016*, 7596175. https://doi.org/10.1155/2016/7596175

Elmes, A., Rogan, J., Williams, C., Ratick, S., Nowak, D., & Martin, D. (2017). Effects of urban tree canopy loss on land surface temperature magnitude and timing. *ISPRS Journal of Photogrammetry and Remote Sensing*, *128*, 338–353. https://doi.org/https://doi.org/10.1016/j.isprsjprs.2017.04.011

EPA. (2016). Heat Island Effect. *United States Environmental Protection Agency*. Retrieved April 14, 2020, from https://www.epa.gov/heat-islands

Ermida, S. L., Soares, P., Mantas, V., Göttsche, F.-M., & Trigo, I. F. (2020). Google Earth Engine Open-Source Code for Land Surface Temperature Estimation from the Landsat Series. In *Remote Sensing* (Vol. 12, Issue 9). https://doi.org/10.3390/rs12091471

Evans, G., Schmidt, V., Bush, P., & Nelson, H. (1969). Stratigraphy and Geologic History of The Sabkha, Abu Dhabi, Persian Gulf. *International Association of Sedimentologists*, *12*(1–2), 145–159. https://doi.org/10.1111/j.1365-3091.1969.tb00167.x

Fadhil, A. M. (2011). Drought mapping using Geoinformation technology for some sites in the Iraqi Kurdistan region. *International Journal of Digital Earth*, *4*(3), 239–257. https://doi.org/10.1080/17538947.2010.489971

Fallah Shamsi, S. R., Zare, S., & Abtahi, S. A. (2013). Soil salinity characteristics using moderate resolution imaging spectroradiometer (MODIS) images and statistical analysis. *Archives of Agronomy and Soil Science*, *59*(4), 471–489.

Fan, C., Li, Y., Guang, J., Li, Z., Elnashar, A., Allam, M., & de Leeuw, G. (2020). The impact of the control measures during the COVID-19 outbreak on air pollution in China. *Remote Sensing*, *12*(10). https://doi.org/10.3390/rs12101613

FAO. (2008). AQUASTAT Country Profile – United Arab Emirates. In *Food and Agriculture Organization of the United Nations (FAO)*. http://www.fao.org/3/ca0335en/CA0335EN.pdf

Farahat, A. (2016). Air pollution in the Arabian Peninsula (Saudi Arabia, the United Arab Emirates, Kuwait, Qatar, Bahrain, and Oman): causes, effects, and aerosol categorization. *Arabian Journal of Geosciences*, *9*(3), 196. https://doi.org/10.1007/s12517-015-2203-y

Farifteh, J., Farshad, A., & George, R. J. (2006). Assessing salt-affected soils using remote sensing, solute modelling, and geophysics. *Geoderma*, *130*(3–4), 191–206.

Feizizadeh, B., & Blaschke, T. (2013). Examining Urban Heat Island Relations to Land Use and Air Pollution: Multiple Endmember Spectral Mixture Analysis for Thermal Remote Sensing. *IEEE Journal of Selected Topics in Applied Earth Observations and Remote Sensing*, *6*(3), 1749–1756. https://doi.org/10.1109/JSTARS.2013.2263425

Fernandez-Buces, N., Siebe, C., Cram, S., & Palacio, J. L. (2006). Mapping soil salinity using a combined spectral response index for bare soil and vegetation: A case study in the former lake Texcoco, Mexico. *Journal of Arid Environments*, *65*(4), 644–667.

Filonchyk, M., Hurynovich, V., Yan, H., Gusev, A., & Shpilevskaya, N. (2020). Impact Assessment of COVID-19 on Variations of SO2, NO2, CO and AOD over East China. *Aerosol and Air Quality Research*, *20*(7), 1530–1540. https://doi.org/10.4209/aaqr.2020.05.0226

Firozjaei, M. K., Kiavarz, M., Alavipanah, S. K., Lakes, T., & Qureshi, S. (2018). Monitoring and forecasting heat island intensity through multi-temporal image analysis and cellular automata-Markov chain modelling: A case of Babol city, Iran. *Ecological Indicators*, *91*, 155–170. https://doi.org/10.1016/j.ecolind.2018.03.052

Frey, C. M., Rigo, G., & Parlow, E. (2005). Investigation of the Daily Urban Cooling Island (Uci) in Two Coastal Cities in an Arid Environment : Dubai and Abu Dhabi (U.A.E). *Remote Sensing and Spatial Information Sciences*, *36*, 1–5.

Frey, C. M., Rigo, G., & Parlow, E. (2007). Urban radiation balance of two coastal cities in a hot and dry environment. *International Journal of Remote Sensing*, *28*(12), 2695–2712. https://doi.org/10.1080/01431160600993389

Furby, S., Caccetta, P., & Wallace, J. (2010). Salinity monitoring in Western Australia using remotely sensed and other spatial data. *Journal of Environmental Quality*, *39*(1), 16–25.

Garcia, L., Eldeiry, A., & Elhaddad, A. (2005). Estimating soil salinity using remote sensing data. *Proceedings for the 2005 Central Plains Irrigation Conference, Sterling, Colorado, February 16-17*.

Gautam, S. (2020). The influence of COVID-19 on air quality in India: a boon or inutile. *Bulletin of Environmental Contamination and Toxicology*, 104, 724-726. https://doi.org/10.1007/s00128-020-02877-y

Georgiou, A. M., & Varnava, S. T. (2019). Evaluation of Modis-Derived Lst Products With Air Temperature Measurements in Cyprus. *Geoplanning: Journal of Geomatics and Planning*, *6*(1), 1. https://doi.org/10.14710/geoplanning.6.1.1-12

Ghassemi, F., Jakeman, A. J., & Nix, H. A. (1995). *Salinisation of land and water resources: human causes, extent, management and case studies.* (1st ed.). CAB International.

Ghoneim, E. (2008). Optimum groundwater locations in the northern United Arab Emirates. *International Journal of Remote Sensing*, *29*(20), 5879–5906. https://doi.org/10.1080/01431160801932517

Gleick, P. H. (1993). Water in crisis. Pacific Institute for Studies. In *Dev., Environment & Security*. Oxford University Press.

Goossens, R., & Van Ranst, E. (1998). The use of remote sensing to map gypsiferous soils in the Ismailia Province (Egypt). *Geoderma*, *87*(1–2), 47–56.

Goswami, A., Mohammad, P., & Sattar, A. (2016). A temporal study of Urban Heat Island (UHI) A Evaluation of Ahmedabad city , Gujarat. *International Conference on Climate Change Mitigation and Technologies for Adaptation*, *October 2018*, 63–68.

Griffin, D., Zhao, X., McLinden, C. A., Boersma, F., Bourassa, A., Dammers, E., Degenstein, D., Eskes, H., Fehr, L., Fioletov, V., Hayden, K., Kharol, S. K., Li, S., Makar, P., Martin, R. V., Mihele, C., Mittermeier, R. L., Krotkov, N., Sneep, M., … Wolde, M. (2019). High-Resolution Mapping of Nitrogen Dioxide With TROPOMI: First Results and Validation Over the Canadian Oil Sands. *Geophysical Research Letters*, *46*(2), 1049–1060. https://doi.org/10.1029/2018GL081095

Gupta, N., Mathew, A., & Khandelwal, S. (2020). Spatio-temporal impact assessment of land use / land cover (LU-LC) change on land surface temperatures over Jaipur city in India. *International Journal of Urban Sustainable Development*, *3138*. Retrieved June 13, 2020, from https://doi.org/10.1080/19463138.2020.1727908

Gutro, R. (2006). *There's a Change in Rain Around Desert Cities*. NASA/Goddard Space Flight Center. https://www.nasa.gov/centers/goddard/news/topstory/2006/arid_phoenix.html

Haashemi, S., Weng, Q., Darvishi, A., & Alavipanah, S. K. (2016). Seasonal variations of the surface urban heat Island in a semi-arid city. *Remote Sensing*, *8*(4), 352. https://doi.org/10.3390/rs8040352

Hadria, R., Benabdelouahab, T., Elmansouri, L., Gadouali, F., Ouatiki, H., Lebrini, Y., Boudhar, A., Salhi, A., & Lionboui, H. (2019). Derivation of air temperature of agricultural areas of Morocco from remotely land surface temperature based on the updated Köppen-Geiger climate classification. *Modeling Earth Systems and Environment*, *5*(4), 1883–1892. https://doi.org/10.1007/s40808-019-00645-4

Hardisky, M., Lemas, V., & Rm, S. (1983). The Influence of Soil Salinity, Growth Form, and Leaf Moisture on the Spectral Radiance of Spartina alterniflora Canopies. *Photogrammetric Engineering & Remote Sensing*, *49*(1), 77–83.

Hart, M. A., & Sailor, D. J. (2009). Quantifying the influence of land-use and surface characteristics on spatial variability in the urban heat island. *Theoretical and Applied Climatology*, *95*(3), 397–406. https://doi.org/10.1007/s00704-008-0017-5

Hashim, B. M., & Sultan, M. A. (2010). Using remote sensing data and GIS to evaluate air pollution and their relationship with land cover and land use in Baghdad City. *Iranian Journal of Earth Sciences*, *2*(1), 20–24.

Headley, J., Hayley, K., Gharibi, M., Forté, S. A., & Macdonald, J. (2007). Geophysical Assessment of Salt and Hydrocarbon Contaminated Soils. *Remediation Technologies Symposium. Environmental Services Association of Alberta*, 1–33.

Bentley, L. R., Headley, J., Hayley, K., Gharibi, M., Forté, S. A., & MacDonald, J. (2007). Geophysical assessment of salt and hydrocarbon contaminated soils. In *Remediation Technologies Symposium*. Environmental Services Association of Alberta.

Hengl, T., Heuvelink, G. B. M., Tadić, M. P., & Pebesma, E. J. (2012). Spatio-temporal prediction of daily temperatures using time-series of MODIS LST images. *Theoretical and Applied Climatology*, *107*(1–2), 265–277. https://doi.org/10.1007/s00704-011-0464-2

Hereher, M. E. (2017a). Effects of land use/cover change on regional land surface temperatures: severe warming from drying Toshka lakes, the Western Desert of Egypt. *Natural Hazards*, *88*(3), 1789–1803. https://doi.org/10.1007/s11069-017-2946-8

Hereher, M. E. (2017b). Retrieving spatial variations of land surface temperatures from satellite data–Cairo region, Egypt. *Geocarto International*, *32*(5), 556–568. https://doi.org/10.1080/10106049.2016.1161077

Hereher, M. E. (2019). Estimation of monthly surface air temperatures from MODIS LST time series data: application to the deserts in the Sultanate of Oman. *Environmental Monitoring and Assessment*, *191*(9). https://doi.org/10.1007/s10661-019-7771-y

Hereher, M. E., & El Kenawy, A. (2020). Extrapolation of daily air temperatures of Egypt from MODIS LST data. *Geocarto International*, 1–17. https://doi.org/10.1080/10106049.2020.1713229

Hooker, J., Duveiller, G., & Cescatti, A. (2018). Data descriptor: A global dataset of air temperature derived from satellite remote sensing and weather stations. *Scientific Data*, *5*, 1–11. https://doi.org/10.1038/sdata.2018.246

Hu, J., Peng, J., Zhou, Y., Xu, D., Zhao, R., Jiang, Q., Fu, T., Wang, F., & Shi, Z. (2019a). Quantitative estimation of soil salinity using UAV-borne hyperspectral and satellite multispectral images. *Remote Sensing*, *11*(7), 736. https://doi.org/10.3390/rs11070736

Hu, L., & Brunsell, N. A. (2013). The impact of temporal aggregation of land surface temperature data for surface urban heat island (SUHI) monitoring. *Remote Sensing of Environment*, *134*, 162–174. https://doi.org/10.1016/j.rse.2013.02.022

Hu, W., Shao, M. A., Wan, L., & Si, B. C. (2014). Spatial variability of soil electrical conductivity in a small watershed on the Loess Plateau of China. *Geoderma*, *230*, 212–220.

Hu, X., Zhao, Z., Zhang, L., Liu, Z., Li, S., & Zhang, X. (2019b). A high-temperature risk assessment model for maize based on MODIS LST. *Sustainability (Switzerland)*, *11*(23), 6601. https://doi.org/10.3390/su11236601

Hu, Y., Hou, M., Jia, G., Zhao, C., Zhen, X., & Xu, Y. (2019c). Comparison of surface and canopy urban heat islands within megacities of eastern China. *ISPRS Journal of Photogrammetry and Remote Sensing*, *156*, 160–168. https://doi.org/10.1016/j.isprsjprs.2019.08.012

Huang, R., Zhang, C., Huang, J., Zhu, D., Wang, L., & Liu, J. (2015). Mapping of daily mean air temperature in agricultural regions using daytime and nighttime land surface temperatures derived from TERRA and AQUA MODIS data. *Remote Sensing*, *7*(7), 8728–8756. https://doi.org/10.3390/rs70708728

Huang, Y., Yuan, M., & Lu, Y. (2019). Spatially varying relationships between surface urban heat islands and driving factors across cities in China. *Environment and Planning B: Urban Analytics and City Science*, *46*(2), 377–394. https://doi.org/10.1177/2399808317716935

Huete, A. (1988). Huete, AR A soil-adjusted vegetation index (SAVI). Remote Sensing of Environment. *Remote Sensing of Environment*, *25*, 295–309.

Huete, A. R., Liu, H. Q., Batchily, K. V, & Van Leeuwen, W. (1997). A comparison of vegetation indices over a global set of TM images for EOS-MODIS. *Remote Sensing of Environment*, *59*(3), 440–451.

Hulley, G. C., Ghent, D., Göttsche, F. M., Guillevic, P. C., Mildrexler, D. J., & Coll, C. (2019). Land Surface Temperature. In *Taking the Temperature of the Earth* (pp. 57-127). Elsevier. https://doi.org/10.1016/B978-0-12-814458-9.00003-4

Ibrahim, M. (2016). Modeling soil salinity and mapping using spectral remote sensing data in the arid and semi-arid region. *International Journal of Remote Sensing Applications*, *6*, 76–83.

Ibrahim, M., & Abu-Mallouh, H. (2018). Estimate Land Surface Temperature in Relation to Land Use Types and Geological Formations Using Spectral Remote Sensing Data in Northeast Jordan. *Open Journal of Geology*, *08*(02), 174–185. https://doi.org/10.4236/ojg.2018.82011

Ibrahim, M., Ghanem, F., Al-Salameen, A., & Al-Fawwaz, A. (2019). The Estimation of Soil Organic Matter Variation in Arid and Semi-Arid Lands Using Remote Sensing Data. *International Journal of Geosciences*, *10*(05), 576–588. https://doi.org/10.4236/ijg.2019.105033

Ibrahim, M., & Koch, B. (2015). Assessment and mapping of groundwater vulnerability using SAR concentrations and GIS: a case study in Al-Mafraq, Jordan. *Journal of Water Resource and Protection*, *7*(07), 588. doi: 10.4236/jwarp.2015.77047

Imhoff, M. L., Zhang, P., Wolfe, R. E., & Bounoua, L. (2010). Remote sensing of the urban heat island effect across biomes in the continental USA. *Remote Sensing of Environment*, *114*(3), 504–513. https://doi.org/10.1016/j.rse.2009.10.008

IPCC. (2017). *IPCC Expert Meeting on Mitigation, Sustainability and Climate Stabilization Scenarios*. Retrieved October 11, 2020, from https://www.ipcc.ch/site/assets/uploads/2018/02/IPCC_2017_EMR_Scenarios.pdf

Iqbal, F. (2011). Detection of salt affected soil in rice-wheat area using satellite image. *African Journal of Agricultural Research*, *6*(21), 4973–4982.

Isaifan, R. J. (2020). The dramatic impact of Coronavirus outbreak on air quality: Has it saved as much as it has killed so far? *Global Journal of Environmental Science and Management*, *6*(3), 275–288. https://doi.org/10.22034/gjesm.2020.03.01

Islam, M. S., Tusher, T. R., Roy, S., & Rahman, M. (2020). Impacts of nationwide lockdown due to COVID-19 outbreak on air quality in Bangladesh: a spatiotemporal analysis. *Air Quality, Atmosphere & Health*, 1–33. https://doi.org/10.1007/s11869-020-00940-5

Janatian, N., Sadeghi, M., Sanaeinejad, S. H., Bakhshian, E., Farid, A., Hasheminia, S. M., & Ghazanfari, S. (2017). A statistical framework for estimating air temperature using MODIS land surface temperature data. *International Journal of Climatology*, *37*(3), 1181–1194. https://doi.org/10.1002/joc.4766

Jensen, J. R. (2009). *Remote Sensing of the Environment: An Earth Resource Perspective,* (2nd edition). Pearson Education India.

Jones, P., Jedlovec, G., Suggs, R., & Haines, S. (2004). Using modis LST to estimate minimum air temperatures at night. *Conference on Satellite Meteorology and Oceanography*, *January 2004*, 457–462.

Kahya, C., Bektas Balcik, F., Burak Oztaner, Y., & Guney, B. (2016). Determining Land Surface Temperature Relations with Land Use-Land Cover and Air Pollution. *EGUGA*, EPSC2016-16489.

Kaplan, G., & Avdan, Z. (2020). COVID-19: Spaceborne Nitrogen Dioxide Over Turkey. Eskişehir Technical University Journal of Science and Technology A - Applied Sciences and Engineering, June. *21*(2), 251–255. https://doi.org/10.18038/estubtda.724450

Karagulian, F., Temimi, M., Ghebreyesus, D., Weston, M., Kondapalli, N. K., Valappil, V. K., Aldababesh, A., Lyapustin, A., Chaouch, N., Al Hammadi, F., & Al Abdooli, A. (2019). Analysis of a severe dust storm and its impact on air quality conditions using WRF-Chem modeling, satellite imagery, and ground observations. *Air Quality, Atmosphere and Health*, *12*(4), 453–470. https://doi.org/10.1007/s11869-019-00674-z

Kardinal Jusuf, S., Wong, N. H., Hagen, E., Anggoro, R., & Hong, Y. (2007). The influence of land use on the urban heat island in Singapore. *Habitat International*, *31*(2), 232–242. https://doi.org/10.1016/j.habitatint.2007.02.006

Karuppasamy, M. B., Seshachalam, S., Natesan, U., Ayyamperumal, R., Karuppannan, S., Gopalakrishnan, G., & Nazir, N. (2020). Air pollution improvement and mortality rate during COVID-19 pandemic in India: global intersectional study. *Air Quality, Atmosphere & Health*. *13*(11), 1375–1384. https://doi.org/10.1007/s11869-020-00892-w

Keeratikasikorn, C., & Bonafoni, S. (2018a). Satellite images and Gaussian parameterization for an extensive analysis of urban heat Islands in Thailand. *Remote Sensing*, *10*(5), 665. https://doi.org/10.3390/rs10050665

Keeratikasikorn, C., & Bonafoni, S. (2018b). Urban heat island analysis over the land use zoning plan of Bangkok by means of Landsat 8 imagery. *Remote Sensing*, *10*(3), 440. https://doi.org/10.3390/rs10030440

Kerimray, A., Baimatova, N., Ibragimova, O. P., Bukenov, B., Kenessov, B., Plotitsyn, P., & Karaca, F. (2020). Assessing air quality changes in large cities during COVID-19 lockdowns: The impacts of traffic-free urban conditions in Almaty, Kazakhstan. *Science of The Total Environment*, *730*, 139179. https://doi.org/https://doi.org/10.1016/j.scitotenv.2020.139179

Khan, N. M., Rastoskuev, V. V, Sato, Y., & Shiozawa, S. (2005). Assessment of hydrosaline land degradation by using a simple approach of remote sensing indicators. *Agricultural Water Management*, *77*(1–3), 96–109.

Khan, N. M., Rastoskuev, V. V, Shalina, E. V, & Sato, Y. (2001). Mapping Salt-affected Soils Using Remote Sensing Indicators-A Simple Approach With the Use of GIS IDRISI. *In: Proceedings of the 22nd Asian Conference on Remote Sensing Vol. 5,* pp.9.

Khandelwal, Sumit, Goyal, Rohit, Kaul, N., Singhal, & Vijai. (2011). Study of Land Surface Temperature Variations with Distance from Hot Spots for Urban Heat Island Analysis. *Geospatial World Forum, Theme Dimensions and Directions of Geospatial Industry*, 18–21. http://geospatialworldforum.org/2011/proceeding/pdf/Sumit KhandelwalFullPaper.pdf

Khorchani, M., Vicente-Serrano, S. M., Azorin-Molina, C., Garcia, M., Martin-Hernandez, N., Peña-Gallardo, M., El Kenawy, A., & Domínguez-Castro, F. (2018). Trends in LST over the peninsular Spain as derived from the AVHRR imagery data. *Global and Planetary Change*, *166*, 75–93. https://doi.org/10.1016/j.gloplacha.2018.04.006

Khuzestani, R. B., Schauer, J. J., Wei, Y., Zhang, L., Cai, T., Zhang, Y., & Zhang, Y. (2017). Quantification of the sources of long-range transport of PM2.5 pollution in the Ordos region, Inner Mongolia, China. *Environmental Pollution*, *229*, 1019–1031. https://doi.org/https://doi.org/10.1016/j.envpol.2017.07.093

Kissel, D., & Sonon, L. (2008). Soil test handbook for Georgia. Athens: University of Georgia Cooperative Extension. *College of Agricultural & Environmental Sciences. The University of Georgia. Athens, Georgia,* 30602–9105. http://aesl.ces.uga.edu/publications/soil/STHandbook.pdf

Kloog, I., Nordio, F., Coull, B. A., & Schwartz, J. (2014). Predicting spatiotemporal mean air temperature using MODIS satellite surface temperature measurements across the Northeastern USA. *Remote Sensing of Environment*, *150*, 132–139. https://doi.org/10.1016/j.rse.2014.04.024

Lazzarini, M., Marpu, P. R., & Ghedira, H. (2013). Temperature-land cover interactions: The inversion of urban heat island phenomenon in desert city areas. *Remote Sensing of Environment*, *130*, 136–152. https://doi.org/10.1016/j.rse.2012.11.007

Lhissou, R., El Harti, A., & Chokmani, K. (2014). Mapping soil salinity in irrigated land using optical remote sensing data. *Eurasian Journal of Soil Science*, *3*(2), 82.

Li, B., Liu, Z., Nan, Y., Li, S., & Yang, Y. (2018a). Comparative analysis of urban heat island intensities in Chinese, Russian, and DPRK regions across the transnational urban agglomeration of the Tumen River in Northeast Asia. *Sustainability (Switzerland)*, *10*(8), 14–16. https://doi.org/10.3390/su10082637

Li, H., Xu, X.-L., Dai, D.-W., Huang, Z.-Y., Ma, Z., & Guan, Y.-J. (2020a). Air pollution and temperature are associated with increased COVID-19 incidence: A time series study. *International Journal of Infectious Diseases*, *97*, 278–282. https://doi.org/10.1016/j.ijid.2020.05.076

Li, H., Zhou, Y., Li, X., Meng, L., Wang, X., Wu, S., & Sodoudi, S. (2018b). A new method to quantify surface urban heat island intensity. *Science of the Total Environment*, *624*, 262–272. https://doi.org/10.1016/j.scitotenv.2017.11.360

Li, Q., Guan, X., Wu, P., Wang, X., Zhou, L., Tong, Y., Ren, R., Leung, K. S. M., Lau, E. H. Y., & Wong, J. Y. (2020). Early transmission dynamics in Wuhan, China, of novel coronavirus–infected pneumonia. *New England Journal of Medicine*, *382*,1199-1207. doi: 10.1056/NEJMoa2001316

Li, X., Zhou, Y., Asrar, G. R., Imhoff, M., & Li, X. (2017). The surface urban heat island response to urban expansion: A panel analysis for the conterminous United States. *Science of the Total Environment*, *605–606*, 426–435. https://doi.org/10.1016/j.scitotenv.2017.06.229

Li, Z.-L., Tang, B.-H., Wu, H., Ren, H., Yan, G., Wan, Z., Trigo, I. F., & Sobrino, J. A. (2013). Satellite-derived land surface temperature: Current status and perspectives. *Remote Sensing of Environment*, *131*, 14–37. https://doi.org/https://doi.org/10.1016/j.rse.2012.12.008

Liang, S., Li, X., & Wang, J. B. T.-A. R. S. (Eds.). (2012). *Chapter 8 - Land-Surface Temperature and Thermal Infrared Emissivity* (pp. 235-271). Academic Press. https://doi.org/https://doi.org/10.1016/B978-0-12-385954-9.00008-3

Liang, S., Zhong, B., & Fang, H. (2006). Improved estimation of aerosol optical depth from MODIS imagery over land surfaces. *Remote Sensing of Environment*, *104*(4), 416–425. https://doi.org/https://doi.org/10.1016/j.rse.2006.05.016

Lillesand, T., Kiefer, R., & Chipman, J. (2004). *Remote Sensing and Image Interpretation* (5th edition). John Wiley & Sons.

Lin, P., Gou, Z., Lau, S. S. Y., & Qin, H. (2017). The impact of urban design descriptors on outdoor thermal environment: A literature review. *Energies*, *10*(12), 1–20. https://doi.org/10.3390/en10122151

Lin, X., Zhang, W., Huang, Y., Sun, W., Han, P., Yu, L., & Sun, F. (2016). Empirical estimation of near-surface air temperature in China from MODIS LST data by considering physiographic features. *Remote Sensing*, *8*(8), 1–15. https://doi.org/10.3390/rs8080629

Liu, H., Zhou, Q., Zhang, S., & Deng, X. (2019). Estimation of Summer Air Temperature over China Using Himawari-8 AHI and Numerical Weather Prediction Data. *Advances in Meteorology*, *2019*. https://doi.org/10.1155/2019/2385310

Liu, Y., & Key, J. R. (2003). Detection and Analysis of Clear-Sky, Low-Level Atmospheric Temperature Inversions with MODIS. *Journal of Atmospheric and Oceanic Technology*, *20*(12), 1727–1737. https://doi.org/10.1175/1520-0426(2003)020<1727:DAAOCL>2.0.CO;2

Lokier, S. W., Knaf, A., & Kimiagar, S. (2013). A quantitative analysis of Recent arid coastal sedimentary facies from the Arabian Gulf Coastline of Abu Dhabi, United Arab Emirates. *Marine Geology*, *346*, 141–152. https://doi.org/https://doi.org/10.1016/j.margeo.2013.09.006

Lorente, A., Boersma, K. F., Eskes, H. J., Veefkind, J. P., van Geffen, J. H. G. M., de Zeeuw, M. B., Denier van der Gon, H. A. C., Beirle, S., & Krol, M. C. (2019). Quantification of nitrogen oxides emissions from build-up of pollution over Paris with TROPOMI. *Scientific Reports*, *9*(1), 20033. https://doi.org/10.1038/s41598-019-56428-5

Lowe, S. A. (2016). An energy and mortality impact assessment of the urban heat island in the US. *Environmental Impact Assessment Review*, *56*, 139–144. https://doi.org/10.1016/j.eiar.2015.10.004

Lu, L., Zhang, T., Wang, T., & Zhou, X. (2018a). Evaluation of collection-6 MODIS land surface temperature product using multi-year ground measurements in an arid area of northwest China. *Remote Sensing*, *10*(11), 1852. https://doi.org/10.3390/rs10111852

Lu, N., Liang, S., Huang, G., Qin, J., Yao, L., Wang, D., & Yang, K. (2018b). Hierarchical Bayesian space-time estimation of monthly maximum and minimum surface air temperature. *Remote Sensing of Environment*, *211*(11), 48–58. https://doi.org/10.1016/j.rse.2018.04.006

Lyapustin, A., & Wang, Y. (2018). MCD19A2 MODIS/Terra+Aqua Land Aerosol Optical Depth Daily L2G Global 1km SIN Grid V006. *NASA EOSDIS Land Processes DAAC*. https://doi.org/10.5067/MODIS/MCD19A2.006

Lyapustin, A., Wang, Y., Korkin, S., & Huang, D. (2018). MODIS Collection 6 MAIAC algorithm. *Atmos. Meas. Tech.*, *11*(10), 5741–5765. https://doi.org/10.5194/amt-11-5741-2018

Majed, I., Barbara, K., & Pawan, D. (2020). Evaluate the Effect the Land Surface Temperature in the Arid and Semi-Arid Lands Using Potential Remote Sensing Data and GIS Techniques. *International Journal of Global Warming; Forthcoming Articles*, *Forthcoming articles, 22*(3). https://doi.org/0.1504/IJG.2020.10031655

Mao, K., Qin, Z., Shi, J., & Gong, P. (2005). A practical split-window algorithm for retrieving land-surface temperature from MODIS data. *International Journal of Remote Sensing*, *26*(15), 3181–3204.

Mathew, A., Khandelwal, S., & Kaul, N. (2017). Investigating spatial and seasonal variations of urban heat island effect over Jaipur city and its relationship with vegetation, urbanization and elevation parameters. *Sustainable Cities and Society*, *35*, 157–177. https://doi.org/10.1016/j.scs.2017.07.013

Mathew, A., Khandelwal, S., & Kaul, N. (2018). Investigating spatio-temporal surface urban heat island growth over Jaipur city using geospatial techniques. *Sustainable Cities and Society*, *40*, 484–500. https://doi.org/10.1016/j.scs.2018.04.018

Mehdipour, V., & Memarianfard, M. (2017). Application of support vector machine and gene expression programming on tropospheric ozone prognosticating for Tehran metropolitan. *Civ Eng J*, *3*(8), 557–567.

Mehrjardi, R. T., Mahmoodi, S. H., Taze, M., & Sahebjalal, E. (2008). Accuracy assessment of soil salinity map in Yazd-Ardakan Plain, Central Iran, based on Landsat ETM+ imagery. *Am.-Eurasian J. Agric. Environ. Sci*, *3*, 708–712.

Metternicht, G. (1998). Analysing the relationship between ground based reflectance and environmental indicators of salinity processes in the Cochabamba Valleys (Bolivia). *International Journal of Ecology and Environmental Sciences*, *24*(4), 359–370.

Metternicht, G. I., & Zinck, J. A. (2003). Remote sensing of soil salinity: potentials and constraints. *Remote Sensing of Environment*, *85*(1), 1–20.

Meyer, H., Katurji, M., Appelhans, T., Müller, M. U., Nauss, T., Roudier, P., & Zawar-Reza, P. (2016). Mapping daily air temperature for Antarctica Based on MODIS LST. *Remote Sensing*, *8*(9), 1–16. https://doi.org/10.3390/rs8090732

Meyer, H., Katurji, M., Detsch, F., Morgan, F., Nauss, T., Roudier, P., & Zawar-reza, P. (2019). AntAir: satellite-derived 1 km daily Antarctic air temperatures since 2003. *Earth Syst. Sci. Data Discuss.*, *2019*, 1–18. https://doi.org/10.5194/essd-2019-215

Miles, V., & Esau, I. (2017). Seasonal and spatial characteristics of Urban Heat Islands (UHIs) in northern West Siberian cities. *Remote Sensing*, *9*(10), 989 https://doi.org/10.3390/rs9100989

Millward, A. A., & Sabir, S. (2011). Benefits of a forested urban park: What is the value of Allan Gardens to the city of Toronto, Canada? *Landscape and Urban Planning*, *100*(3), 177–188. https://doi.org/https://doi.org/10.1016/j.landurbplan.2010.11.013

Misslin, R., Vaguet, Y., Vaguet, A., & Daudé, É. (2018). Estimating air temperature using MODIS surface temperature images for assessing Aedes aegypti thermal niche in Bangkok, Thailand. *Environmental Monitoring and Assessment*, *190*(9), 537. https://doi.org/10.1007/s10661-018-6875-0

Mohamed, A. A., Odindi, J., & Mutanga, O. (2017). Land surface temperature and emissivity estimation for Urban Heat Island assessment using medium- and low-resolution space-borne sensors: A review. *Geocarto International*, *32*(4), 455–470. https://doi.org/10.1080/10106049.2016.1155657

Mohammad, P., Goswami, A., & Bonafoni, S. (2019). The impact of the land cover dynamics on surface urban heat island variations in semi-arid cities: A case study in Ahmedabad City, India, using multi-sensor/source data. *Sensors (Switzerland)*, *19*(17). https://doi.org/10.3390/s19173701

Mohan, M., Kikegawa, Y., Gurjar, B. R., Bhati, S., Kandya, A., & Ogawa, K. (2012). Urban Heat Island Assessment for a Tropical Urban Airshed in India. *Atmospheric and Climate Sciences*, *02*(02), 127–138. https://doi.org/10.4236/acs.2012.22014

Moradi, M., Salahi, B., & Masoodian, S. A. (2018). On the relationship between MODIS Land Surface Temperature and topography in Iran. *Physical Geography, 39*(4), 354–367. https://doi.org/10.1080/02723646.2018.1426167

Mostovoy, G. V., King, R. L., Reddy, K. R., Kakani, V. G., & Filippova, M. G. (2006). Statistical estimation of daily maximum and minimum air temperatures from MODIS LST data over the State of Mississippi. *GIScience and Remote Sensing*, *43*(1), 78–110. https://doi.org/10.2747/1548-1603.43.1.78

Motesaddi, S., Hashempour, Y., & Nowrouz, P. (2017). Characterizing of air pollution in Tehran: comparison of two air quality indices. *Civil Engineering Journal*, *3*(9), 749–758.

Mougenot, B., Pouget, M., & Epema, G. F. (1993). Remote sensing of salt affected soils. *Remote Sensing Reviews*, *7*(3–4), 241–259.

Mukherjee, S., & Debnath, A. (2020). *Correlation between Land Surface Temperature and Urban Heat Island with COVID-19 in New Delhi, India*. Research Square. https://doi.org/10.21203/rs.3.rs-30416/v1

Mulenga, D., & Siziya, S. (2019). Indoor air pollution related respiratory ill health, a sequel of biomass use. *SciMedicine Journal*, *1*(1), 30–37.

Murad, A., & Aldahan, A. (2019). The impact of climate change on the future resources of the UAE. In climate change and the future of water. *The Emirates Center for Strategic Studies and Research*, 45–69.

Nakada, L. Y. K., & Urban, R. C. (2020). COVID-19 pandemic: Impacts on the air quality during the partial lockdown in São Paulo state, Brazil. *Science of The Total Environment*, *730*, 139087. https://doi.org/https://doi.org/10.1016/j.scitotenv.2020.139087

Nemati, M., Ebrahimi, B., & Nemati, F. (2020). Assessment of Iranian nurses' knowledge and anxiety toward COVID-19 during the current outbreak in Iran. *Archives of Clinical Infectious Diseases*, *15*(COVID-19). doi: 10.5812/archcid.102848.

Neves, G. L., Virgens Filho, J. S., Leite, M. L., & Santos, E. N. (2016). Trend of Air Temperature in the State of Paraná, Brazil (Tendência Da Temperatura Do Ar No Estado Do Paraná, Brasil). *Revista Brasileira de Climatologia*, *18*. https://doi.org/10.5380/abclima.v18i0.45639

Noi, P. T., Degener, J., & Kappas, M. (2017). Comparison of multiple linear regression, cubist regression, and random forest algorithms to estimate daily air surface temperature from dynamic combinations of MODIS LST data. *Remote Sensing*, *9*(5), 398. https://doi.org/10.3390/rs9050398

Noi, P. T., Kappas, M., & Degener, J. (2016). Estimating daily maximum and minimum land air surface temperature using MODIS land surface temperature data and ground truth data in Northern Vietnam. *Remote Sensing*, *8*(12), 1002. https://doi.org/10.3390/rs8121002

Olaguer, E. P. (2017). Greenhouse Gas Emissions and Climate Impacts. In *Environmental Science* (pp. 55-64). Elsevier. https://doi.org/10.1016/B978-0-12-801883-5.00006-1

Omer, T. M. A. (2011). Country Pasture/Forage Resource Profiles: IRAQ. (FAO).

Otgonbayar, M., Atzberger, C., Mattiuzzi, M., & Erdenedalai, A. (2019). Estimation of climatologies of average monthly air temperature over mongolia using MODIS land surface temperature (LST) time series and machine learning techniques. *Remote Sensing*, *11*(21), 1–24. https://doi.org/10.3390/rs11212588

Otmani, A., Benchrif, A., Tahri, M., Bounakhla, M., Chakir, E. M., El Bouch, M., & Krombi, M. (2020). Impact of Covid-19 lockdown on PM10, SO2 and NO2 concentrations in Salé City (Morocco). *Science of The Total Environment*, *735*, 139541. https://doi.org/10.1016/j.scitotenv.2020.139541

Pathakoti, M., Muppalla, A., Hazra, S., Dangeti, M., Shekhar, R., Jella, S., Mullapudi, S. S., Andugulapati, P., & Vijayasundaram, U. (2020). An assessment of the impact of a nation-wide lockdown on air pollution – a remote sensing perspective over India. *Atmos. Chem. Phys. Discuss.*, *2020*, 1–16. https://doi.org/10.5194/acp-2020-621

Paul, P., Al Tenaiji, A. K., & Braimah, N. (2016). A Review of the Water and Energy Sectors and the Use of a Nexus Approach in Abu Dhabi. *International Journal of Environmental Research and Public Health*, *13*(4), 364. https://doi.org/10.3390/ijerph13040364

Peel, M. C., Finlayson, B. L., & McMahon, T. A. (2007). Updated world map of the Köppen-Geiger climate classification. *Hydrol. Earth Syst. Sci.*, *11*, 1633–1644. https://doi.org/10.5194/hess-11-1633–2007

Peng, J., Ma, J., Liu, Q., Liu, Y., Hu, Y., Li, Y., & Yue, Y. (2018). Spatial-temporal change of land surface temperature across 285 cities in China: An urban-rural contrast perspective. *Science of the Total Environment*, *635*, 487–497. https://doi.org/10.1016/j.scitotenv.2018.04.105

Peng, S., Piao, S., Ciais, P., Friedlingstein, P., Ottle, C., Bréon, F. M., Nan, H., Zhou, L., & Myneni, R. B. (2012). Surface Urban Heat Island Across 419 Global Big Cities. *Environmental Science and Technology*, *46*(12), 6889–6890. https://doi.org/10.1021/es301811b

Pepin, N., Deng, H., Zhang, H., Zhang, F., Kang, S., & Yao, T. (2019). An Examination of Temperature Trends at High Elevations Across the Tibetan Plateau: The Use of MODIS LST to Understand Patterns of Elevation-Dependent Warming. *Journal of Geophysical Research: Atmospheres*, *124*(11), 5738–5756. https://doi.org/10.1029/2018JD029798

Phan, T. N., & Kappas, M. (2018). Application of MODIS land surface temperature data: a systematic literature review and analysis. *Journal of Applied Remote Sensing*, *12*(04), 041501. https://doi.org/10.1117/1.jrs.12.041501

Phan, T. N., Kappas, M., Nguyen, K. T., Tran, T. P., Tran, Q. V., & Emam, A. R. (2019). Evaluation of MODIS land surface temperature products for daily air surface temperature estimation in northwest Vietnam. *International Journal of Remote Sensing*, *40*(14), 5544–5562. https://doi.org/10.1080/01431161.2019.1580789

Qiao, Z., Wu, C., Zhao, D., Xu, X., Yang, J., Feng, L., Sun, Z., & Liu, L. (2019). Determining the boundary and probability of surface urban heat island footprint based on a logistic model. *Remote Sensing*, *11*(11), 1368. https://doi.org/10.3390/rs11111368

Raafat, H. (2006). Climate: In physical geography sector paper, *AGEDI initiative. UAE* (pp. 72-92). Environment Agency – Abu Dhabi.

Radhi, H., & Sharples, S. (2013). Quantifying the domestic electricity consumption for air-conditioning due to urban heat islands in hot arid regions. *Applied Energy*, *112*, 371–380. https://doi.org/10.1016/j.apenergy.2013.06.013

Raj, S., Paul, S. K., Chakraborty, A., & Kuttippurath, J. (2020). Anthropogenic forcing exacerbating the urban heat islands in India. *Journal of Environmental Management*, *257*, 110006. https://doi.org/10.1016/j.jenvman.2019.110006

Ranjan, A. K., Patra, A. K., & Gorai, A. K. (2020). Effect of lockdown due to SARS COVID-19 on aerosol optical depth (AOD) over urban and mining regions in India. *Science of The Total Environment*, *745*, 141024. https://doi.org/https://doi.org/10.1016/j.scitotenv.2020.141024

Rao, Y., Liang, S., Wang, D., Yu, Y., Song, Z., Zhou, Y., Shen, M., & Xu, B. (2019). Estimating daily average surface air temperature using satellite land surface temperature and top-of-atmosphere radiation products over the Tibetan Plateau. *Remote Sensing of Environment*, *234*, 111462. https://doi.org/10.1016/j.rse.2019.111462

Rasul, A., Balzter, H., & Smith, C. (2015). Spatial variation of the daytime Surface Urban Cool Island during the dry season in Erbil, Iraqi Kurdistan, from Landsat 8. *Urban Climate*, *14*(August 2016), 176–186. https://doi.org/10.1016/j.uclim.2015.09.001

Rasul, A., Balzter, H., & Smith, C. (2016). Diurnal and seasonal variation of surface Urban Cool and Heat Islands in the semi-arid city of Erbil, Iraq. *Climate*, *4*(3). https://doi.org/10.3390/cli4030042

Rasul, A., Balzter, H., & Smith, C. (2017a). Applying a normalized ratio scale technique to assess influences of urban expansion on land surface temperature of the semi-arid city of Erbil. *International Journal of Remote Sensing*, *38*(13), 3960–3980. https://doi.org/10.1080/01431161.2017.1312030

Rasul, A., Balzter, H., Smith, C., Remedios, J., Adamu, B., Sobrino, J., Srivanit, M., & Weng, Q. (2017b). A Review on Remote Sensing of Urban Heat and Cool Islands. *Land, 6*(2), 38. https://doi.org/10.3390/land6020038

Reisi, M., Ahmadi Nadoushan, M., & Aye, L. (2019). Remote sensing for urban heat and cool islands evaluation in semi-arid areas. *Global Journal of Environmental Science and Management*, *5*(3), 319–330. https://doi.org/10.22034/gjesm.2019.03.05

Rikimaru, A., Roy, P. S., & Miyatake, S. (2002). Tropical forest cover density mapping. *Tropical Ecology*, *43*, 39–47.

Rouse, J. W., Haas, R.H.; Schell, J. A., & Deering, D. W. (1974). Monitoring vegetation systems in the Great Plains with ERTS. In *Proceedings of the Third Earth Resources Technology Satellite- 1 Symposium*, *Vol.1, 10-14 December, 1973* (pp. 301–317). NASA Scientific and Technical Information Office Washington, DC.

Sanaeinejad, S. H., Astaraei, A., Mousavi, P. M., & Ghaemi, M. (2009). Selection of best band combination for soil salinity studies using ETM satellite images (A Case study: Nyshaboor region, Iran). *International Journal of Environmental and Ecological Engineering*. *3*(6), 179–181

Santamouris, M. (2014). Cooling the cities – A review of reflective and green roof mitigation technologies to fight heat island and improve comfort in urban environments. *Solar Energy*, *103*, 682–703. https://doi.org/https://doi.org/10.1016/j.solener.2012.07.003

Sattari, F., & Hashim, M. (2014). A brief review of land surface temperature retrieval methods from thermal satellite sensors. *Middle-East Journal of Scientific Research*, *22*(5), 757–768.

Schwarz, N., Lautenbach, S., & Seppelt, R. (2011). Exploring indicators for quantifying surface urban heat islands of European cities with MODIS land surface temperatures. *Remote Sensing of Environment*, *115*(12), 3175–3186. https://doi.org/10.1016/j.rse.2011.07.003

Sekmoudi, I., Khomsi, K., Faieq, S., & Idrissi, L. (2020). Covid-19 lockdown improves air quality in Morocco. *ArXiv Preprint ArXiv,* 2007.05417.

Serra, C., Lana, X., Martínez, M. D., Roca, J., Arellano, B., Biere, R., Moix, M., & Burgueño, A. (2020). Air temperature in Barcelona metropolitan region from MODIS satellite and GIS data. *Theoretical and Applied Climatology*, *139*(1–2), 473–492. https://doi.org/10.1007/s00704-019-02973-y

Shah, D. B., Pandya, M. R., Trivedi, H. J., & Jani, A. R. (2012). Estimation of minimum and maximum air temperature using MODIS data over Gujarat. *Journal of Agrometeorology*, *14*(2), 111–118. http://www.mosdac.gov.in

Shah, D. B., Pandya, M. R., Trivedi, H. J., & Jani, A. R. (2013). Estimating minimum and maximum air temperature using MODIS data over Indo-Gangetic Plain. *Journal of Earth System Science*, *122*(6), 1593–1605. https://doi.org/10.1007/s12040-013-0369-9

Sharma, S., Zhang, M., Anshika, Gao, J., Zhang, H., & Kota, S. H. (2020). Effect of restricted emissions during COVID-19 on air quality in India. *Science of The Total Environment*, *728*, 138878. https://doi.org/https://doi.org/10.1016/j.scitotenv.2020.138878

Shastri, H., Barik, B., Ghosh, S., Venkataraman, C., & Sadavarte, P. (2017). Flip flop of Day-night and Summer-Winter Surface Urban Heat Island Intensity in India. *Scientific Reports*, *7*, 1–8. https://doi.org/10.1038/srep40178

Sherafati, S., Saradjian, M. R., & Rabbani, A. (2018). Assessment of Surface Urban Heat Island in Three Cities Surrounded by Different Types of Land-Cover Using Satellite Images. *Journal of the Indian Society of Remote Sensing*, *46*(7), 1013–1022. https://doi.org/10.1007/s12524-017-0725-3

Sherif, M., Almulla, M., Shetty, A., & Chowdhury, R. K. (2014). Analysis of rainfall, PMP and drought in the United Arab Emirates. *International Journal of Climatology*, *34*(4), 1318–1328.

Shrestha, D., & Farshad, A. (2009). Mapping Salinity Hazard : An Integration Application of Remote Sensing and Modeling-Based Techniques. In G. M. A.J. Zinck (Ed.), *Remote sensing of soil salinization : impact on land management* (pp. 257-272). CRC Press.

Shrivastava, P., & Kumar, R. (2015). Soil salinity: a serious environmental issue and plant growth promoting bacteria as one of the tools for its alleviation. *Saudi Journal of Biological Sciences*, *22*(2), 123–131.

Singh, S., Bhardwaj, A., Singh, A., Sam, L., Shekhar, M., Martín-Torres, F. J., & Zorzano, M. P. (2019). Quantifying the congruence between air and land surface temperatures for various climatic and elevation zones of Western Himalaya. *Remote Sensing*, *11*(24), 2889. https://doi.org/10.3390/rs11242889

Sobrino, J. A., El Kharraz, J., & Li, Z.-L. (2003). Surface temperature and water vapour retrieval from MODIS data. *International Journal of Remote Sensing*, *24*(24), 5161–5182.

Song, L., Liu, S., Kustas, W. P., Nieto, H., Sun, L., Xu, Z., Skaggs, T. H., Yang, Y., Ma, M., Xu, T., Tang, X., & Li, Q. (2018a). Monitoring and validating spatially and temporally continuous daily evaporation and transpiration at river basin scale. *Remote Sensing of Environment*, *219*, 72–88. https://doi.org/https://doi.org/10.1016/j.rse.2018.10.002

Song, Z., Li, R., Qiu, R., Liu, S., Tan, C., Li, Q., Ge, W., Han, X., Tang, X., Shi, W., Song, L., Yu, W., Yang, H., & Ma, M. (2018b). Global land surface temperature influenced by vegetation cover and PM 2.5 from 2001 to 2016. *Remote Sensing*, *10*(12), 1–18. https://doi.org/10.3390/rs10122034

Steven, M. D., Malthus, T. J., Danson, F. M., Jaggard, K. W., & Andrieu, B. (1992). Monitoring responses of vegetation to stress. *Proceedings Annual Conference of the Remote Sensing Society, Dundee, 1992* . pp. 369-377

Stisen, S., Sandholt, I., Nørgaard, A., Fensholt, R., & Eklundh, L. (2007). Estimation of diurnal air temperature using MSG SEVIRI data in West Africa. *Remote Sensing of Environment*, *110*(2), 262–274. https://doi.org/10.1016/j.rse.2007.02.025

Streutker, D. R. (2003). Satellite-measured growth of the urban heat island of Houston, Texas. *Remote Sensing of Environment*, *85*(3), 282–289. https://doi.org/10.1016/S0034-4257(03)00007-5

Sun, H., Chen, Y., Gong, A., Zhao, X., Zhan, W., & Wang, M. (2014). Estimating mean air temperature using MODIS day and night land surface temperatures. *Theoretical and Applied Climatology*, *118*(1–2), 81–92. https://doi.org/10.1007/s00704-013-1033-7

Sun, R., & Chen, L. (2017). Effects of green space dynamics on urban heat islands: Mitigation and diversification. *Ecosystem Services*, *23*, 38–46. https://doi.org/https://doi.org/10.1016/j.ecoser.2016.11.011

Tam, B. Y., Gough, W. A., & Mohsin, T. (2015). The impact of urbanization and the urban heat island effect on day to day temperature variation. *Urban Climate*, *12*, 1–10. https://doi.org/10.1016/j.uclim.2014.12.004

Tan, M., & Li, X. (2015). Quantifying the effects of settlement size on urban heat islands in fairly uniform geographic areas. *Habitat International*, *49*, 100–106. https://doi.org/10.1016/j.habitatint.2015.05.013

Tobías, A., Carnerero, C., Reche, C., Massagué, J., Via, M., Minguillón, M. C., Alastuey, A., & Querol, X. (2020). Changes in air quality during the lockdown in Barcelona (Spain) one month into the SARS-CoV-2 epidemic. *Science of The Total Environment*, *726*, 138540. https://doi.org/https://doi.org/10.1016/j.scitotenv.2020.138540

Tomlinson, C. J., Chapman, L., Thornes, J. E., & Baker, C. (2011). Remote sensing land surface temperature for meteorology and climatology: a review. *Meteorological Applications*, *18*(3), 296–306. https://doi.org/10.1002/met.287

Tomlinson, C. J., Chapman, L., Thornes, J. E., Baker, C. J., & Prieto-Lopez, T. (2012). Comparing night-time satellite land surface temperature from MODIS and ground measured air temperature across a conurbation. *Remote Sensing Letters*, *3*(8), 657–666. https://doi.org/10.1080/01431161.2012.659354

Tran, H., Uchihama, D., Ochi, S., & Yasuoka, Y. (2006). Assessment with satellite data of the urban heat island effects in Asian mega cities. *International Journal of Applied Earth Observation and Geoinformation*, *8*(1), 34–48. https://doi.org/10.1016/j.jag.2005.05.003

UN DESA. (2019). *World Urbanization Prospects: The 2018 Revision*. UN. https://doi.org/10.18356/b9e995fe-en

United Nations. (2019). World Urbanization Prospects: The 2018 Revision (ST/ESA/SER.A/420). In *Department of Economic and Social Affairs Population Division* (Vol. 66).

Vancutsem, C., Ceccato, P., Dinku, T., & Connor, S. J. (2010). Evaluation of MODIS land surface temperature data to estimate air temperature in different ecosystems over Africa. *Remote Sensing of Environment*, *114*(2), 449–465. https://doi.org/10.1016/j.rse.2009.10.002

Veefkind, J. P., Aben, I., McMullan, K., Förster, H., de Vries, J., Otter, G., Claas, J., Eskes, H. J., de Haan, J. F., Kleipool, Q., van Weele, M., Hasekamp, O., Hoogeveen, R., Landgraf, J., Snel, R., Tol, P., Ingmann, P., Voors, R., Kruizinga, B., … Levelt, P. F. (2012). TROPOMI on the ESA Sentinel-5 Precursor: A GMES mission for global observations of the atmospheric composition for climate, air quality and ozone layer applications. *Remote Sensing of Environment*, *120*, 70–83. https://doi.org/https://doi.org/10.1016/j.rse.2011.09.027

Venter, Z. S., Aunan, K., Chowdhury, S., & Lelieveld, J. (2020). COVID-19 lockdowns cause global air pollution declines with implications for public health risk. *MedRxiv*, 2020.04.10.20060673. https://doi.org/10.1101/2020.04.10.20060673

Vogt, J. V., Viau, A. A., & Paquet, F. (1997). Mapping regional air temperature fields using satellite-derived surface skin temperatures. *International Journal of Climatology*, *17*(14), 1559–1579. https://doi.org/10.1002/(sici)1097-0088(19971130)17:14<1559::aid-joc211>3.3.co;2-x

Voogt, J. A., & Oke, T. R. (2003). Thermal remote sensing of urban climates. *Remote Sensing of Environment*, *86*(3), 370–384. https://doi.org/10.1016/S0034-4257(03)00079-8

Wan, Z. (2008). New refinements and validation of the MODIS Land-Surface Temperature/Emissivity products. *Remote Sensing of Environment*, *112*(1), 59–74. https://doi.org/10.1016/j.rse.2006.06.026

Wan, Z. (2013) *Collection-6 MODIS Land Surface Temperature Products Users' Guide*. ERI, University of California, Santa Barbara.

Wan, Z. (2014). New refinements and validation of the collection-6 MODIS land-surface temperature/emissivity product. *Remote Sensing of Environment*, *140*, 36–45. https://doi.org/10.1016/j.rse.2013.08.027

Wan, Z., & Dozier, J. (1996). A generalized split-window algorithm for retrieving land-surface temperature from space. *IEEE Transactions on Geoscience and Remote Sensing*, *34*(4), 892–905. https://doi.org/10.1109/36.508406

Wan, Z., Hook, S., & Hulley, G. (2015). *MYD11A2 MODIS/Aqua Land Surface Temperature/Emissivity 8-Day L3 Global 1km SIN Grid V006*. NASA EOSDIS Land Processes DAAC. 10.5067/MODIS/MYD11A2.006

Wan, Z., & Li, Z.-L. (1997). A physics-based algorithm for retrieving land-surface emissivity and temperature from EOS/MODIS data. *IEEE Transactions on Geoscience and Remote Sensing*, *35*(4), 980–996.

Wan, Z., Zhang, Y., Zhang, Q., & Li, Z. L. (2004). Quality assessment and validation of the MODIS global land surface temperature. *International Journal of Remote Sensing*, *25*(1), 261–274. https://doi.org/10.1080/0143116031000116417

Wan, Z., Zhang, Y., Zhang, Q., & Li, Z. liang. (2002). Validation of the land-surface temperature products retrieved from terra moderate resolution imaging spectroradiometer data. *Remote Sensing of Environment*, *83*(1–2), 163–180. https://doi.org/10.1016/S0034-4257(02)00093-7

Wang, C., Myint, S. W., Wang, Z., & Song, J. (2016). Spatio-temporal modeling of the urban heat island in the Phoenix metropolitan area: Land use change implications. *Remote Sensing*, *8*(3), 185. https://doi.org/10.3390/rs8030185

Wang, J., Zhou, W., & Wang, J. (2019a). Time-series analysis reveals intensified urban heat island effects but without significant urban warming. *Remote Sensing*, *11*(19), 2229. https://doi.org/10.3390/rs11192229

Wang, M., He, G., Zhang, Z., Wang, G., Wang, Z., Yin, R., Cui, S., Wu, Z., & Cao, X. (2019b). A radiance-based split-window algorithm for land surface temperature retrieval: Theory and application to MODIS data. *International Journal of Applied Earth Observation and Geoinformation*, *76*, 204–217. https://doi.org/10.1016/j.jag.2018.11.015

Wang, Q., & Su, M. (2020). A preliminary assessment of the impact of COVID-19 on environment – A case study of China. *Science of The Total Environment*, *728*, 138915. https://doi.org/https://doi.org/10.1016/j.scitotenv.2020.138915

Wang, W., Liang, S., & Meyers, T. (2008). Validating MODIS land surface temperature products using long-term nighttime ground measurements. *Remote Sensing of Environment*, *112*(3), 623–635. https://doi.org/10.1016/j.rse.2007.05.024

Waring, R. H., & Running, S. W. (2007). Spatial Scaling Methods for Landscape and Regional Ecosystem Analysis. In R. H. Waring & S. W. B. T.-F. E. (Third E. Running (Eds.), *Forest Ecosystems* (pp. 225–259). Academic Press. https://doi.org/10.1016/B978-012370605-8.50014-1

Wei, J., Huang, W., Li, Z., Xue, W., Peng, Y., Sun, L., & Cribb, M. (2019). Estimating 1-km-resolution PM2.5 concentrations across China using the space-time random forest approach. *Remote Sensing of Environment*, *231*, 111221. https://doi.org/10.1016/j.rse.2019.111221

Weng, Q. (2003). Fractal analysis of satellite-detected urban heat island effect. *Photogrammetric Engineering & Remote Sensing*, *69*(5), 555–566.

Weng, Q., Firozjaei, M. K., Kiavarz, M., Alavipanah, S. K., & Hamzeh, S. (2019). Normalizing land surface temperature for environmental parameters in mountainous and urban areas of a cold semi-arid climate. *Science of the Total Environment*, *650*, 515–529.

Weng, Q., & Yang, S. (2006). Urban air pollution patterns, land use, and thermal landscape: an examination of the linkage using GIS. *Environmental Monitoring and Assessment*, *117*(1–3), 463–489. https://doi.org/10.1007/s10661-006-0888-9

WHO. (2020a). *Air pollution*. World Health Organization. Retrieved October 26, 2020, from https://www.who.int/health-topics/air-pollution#tab=tab_1%0AAir

WHO. (2020b). *Coronavirus disease 2019 (COVID-19) Situation Report – 51*. Retrieved October 26, 2020, from https://www.who.int/docs/default-source/coronaviruse/situation-reports/20200311-sitrep-51-covid-19.pdf?sfvrsn=1ba62e57_10

WHO. (2020c). *WHO Coronavirus Disease (COVID-19) Dashboard*. Retrieved October 26, 2020, from https://covid19.who.int/

Wu, W., Al-Shafie, W. M., Mhaimeed, A. S., Ziadat, F., Nangia, V., & Payne, W. B. (2014a). Soil Salinity Mapping by Multiscale Remote Sensing in Mesopotamia, Iraq. *IEEE Journal of Selected Topics in Applied Earth Observations and Remote Sensing*, *7*(11), 4442–4452. https://doi.org/10.1109/JSTARS.2014.2360411

Wu, W., Mhaimeed, A. S., Al-Shafie, W. M., Ziadat, F., Dhehibi, B., Nangia, V., & De Pauw, E. (2014b). Mapping soil salinity changes using remote sensing in Central Iraq. *Geoderma Regional*, *2–3*, 21–31. https://doi.org/https://doi.org/10.1016/j.geodrs.2014.09.002

Wu, W., Zou, L., Shen, X., Lu, S., Su, N., & Kong, F. (2012). Thermal anomalies associated with faults: a case study of the Jinhua–Quzhou basin of Zhejiang Province, China. *International Journal of Remote Sensing*, *33*(6), 1850–1867. https://doi.org/10.1080/01431161.2011.602992

Wu, X., Nethery, R. C., Sabath, B. M., Braun, D., & Dominici, F. (2020). Exposure to air pollution and COVID-19 mortality in the United States: A nationwide cross-sectional study. *MedRxiv: The Preprint Server for Health Sciences*, 2020.04.05.20054502. https://doi.org/10.1101/2020.04.05.20054502

Wu, X., Wang, G., Yao, R., Wang, L., Yu, D., & Gui, X. (2019). Investigating surface urban heat islands in South America based on MODIS data from 2003-2016. *Remote Sensing*, *11*(10), 1212. https://doi.org/10.3390/rs11101212

Xu, K., Cui, K., Young, L.-H., Hsieh, Y.-K., Wang, Y.-F., Zhang, J., & Wan, S. (2020). Impact of the COVID-19 Event on Air Quality in Central China. *Aerosol and Air Quality Research*, *20*(5), 915–929. https://doi.org/10.4209/aaqr.2020.04.0150

Xu, Y., Knudby, A., & Ho, H. C. (2014). Estimating daily maximum air temperature from MODIS in British Columbia, Canada. *International Journal of Remote Sensing*, *35*(24), 8108–8121. https://doi.org/10.1080/01431161.2014.978957

Xu, Y., Qin, Z., & Shen, Y. (2012). Study on the estimation of near-surface air temperature from MODIS data by statistical methods. *International Journal of Remote Sensing*, *33*(24), 7629–7643. https://doi.org/10.1080/01431161.2012.701351

Yang, J., Gong, P., Zhou, J. X., Huang, H. B., & Wang, L. (2010). Detection of the urban heat island in Beijing using HJ-1B satellite imagery. *Science China Earth Sciences*, *53*(SUPPL. 1), 67–73. https://doi.org/10.1007/s11430-010-4131-8

Yang, Q., Huang, X., & Li, J. (2017a). Assessing the relationship between surface urban heat islands and landscape patterns across climatic zones in China. *Scientific Reports*, *7*(1), 1–11. https://doi.org/10.1038/s41598-017-09628-w

Yang, Y. Z., Cai, W. H., & Yang, J. (2017b). Evaluation of MODIS land surface temperature data to estimate near-surface air temperature in Northeast China. *Remote Sensing*, *9*(5), 1–19. https://doi.org/10.3390/rs9050410

Yang, Y., Zhang, M., Li, Q., Chen, B., Gao, Z., Ning, G., Liu, C., Li, Y., & Luo, M. (2020). Modulations of surface thermal environment and agricultural activity on intraseasonal variations of summer diurnal temperature range in the Yangtze River Delta of China. *Science of The Total Environment*, *736*, 139445. https://doi.org/https://doi.org/10.1016/j.scitotenv.2020.139445

Yao, R., Wang, L., Gui, X., Zheng, Y., Zhang, H., & Huang, X. (2017). Urbanization effects on vegetation and surface urban heat islands in China's Yangtze River Basin. *Remote Sensing*, *9*(6), 540. https://doi.org/10.3390/rs9060540

Yao, R., Wang, L., Huang, X., Chen, J., Li, J., & Niu, Z. (2018a). Less sensitive of urban surface to climate variability than rural in Northern China. *Science of the Total Environment*, *628–629*, 650–660. https://doi.org/10.1016/j.scitotenv.2018.02.087

Yao, R., Wang, L., Huang, X., Gong, W., & Xia, X. (2019). Greening in Rural Areas Increases the Surface Urban Heat Island Intensity. *Geophysical Research Letters*, *46*(4), 2204–2212. https://doi.org/10.1029/2018GL081816

Yao, R., Wang, L., Huang, X., Niu, Y., Chen, Y., & Niu, Z. (2018b). The influence of different data and method on estimating the surface urban heat island intensity. *Ecological Indicators*, *89*, 45–55. https://doi.org/10.1016/j.ecolind.2018.01.044

Yao, R., Wang, L., Wang, S., Wang, L., Wei, J., Li, J., & Yu, D. (2020). A detailed comparison of MYD11 and MYD21 land surface temperature products in mainland China. *International Journal of Digital Earth*, 1–17. https://doi.org/10.1080/17538947.2019.1711211

Youssef, A. M., Pradhan, B., Sabtan, A. A., & El-Harbi, H. M. (2012). Coupling of remote sensing data aided with field investigations for geological hazards assessment in Jazan area, Kingdom of Saudi Arabia. *Environmental Earth Sciences*, *65*(1), 119–130. https://doi.org/10.1007/s12665-011-1071-3

Yu, Z., Guo, X., Jørgensen, G., & Vejre, H. (2017). How can urban green spaces be planned for climate adaptation in subtropical cities? *Ecological Indicators*, *82*, 152–162. https://doi.org/https://doi.org/10.1016/j.ecolind.2017.07.002

Zeng, L., Wardlow, B. D., Tadesse, T., Shan, J., Hayes, M. J., Li, D., & Xiang, D. (2015). Estimation of daily air temperature based on MODIS land surface temperature products over the Corn Belt in the US. *Remote Sensing*, *7*(1), 951–970. https://doi.org/10.3390/rs70100951

Zewdu, S., Suryabhagavan, K. V, & Balakrishnan, M. (2017). Geo-spatial approach for soil salinity mapping in Sego Irrigation Farm, South Ethiopia. *Journal of the Saudi Society of Agricultural Sciences*, *16*(1), 16–24.

Zhang, F., Cai, X., & Thornes, J. E. (2014a). Birmingham's air and surface urban heat islands associated with lamb weather types and cloudless anticyclonic conditions. *Progress in Physical Geography*, *38*(4), 431–447. https://doi.org/10.1177/0309133314538725

Zhang, T.-T., Zeng, S.-L., Gao, Y., Ouyang, Z.-T., Li, B., Fang, C.-M., & Zhao, B. (2011a). Using hyperspectral vegetation indices as a proxy to monitor soil salinity. *Ecological Indicators*, *11*(6), 1552–1562.

Zhang, W., Huang, Y., Yu, Y., & Sun, W. (2011b). Empirical models for estimating daily maximum, minimum and mean air temperatures with MODIS land surface temperatures. *International Journal of Remote Sensing*, *32*(24), 9415–9440. https://doi.org/10.1080/01431161.2011.560622

Zhang, Y., Jiang, Z., Huang, H., Fang, Y., Mu, X., & Cheng, X. (2014b). Thermal anomalies detection before 2013 Songyuan earthquake using MODIS LST data. *2014 IEEE Geoscience and Remote Sensing Symposium*, 3009–3012. https://doi.org/10.1109/IGARSS.2014.6947110

Zhang, Z., Arshad, A., Zhang, C., Hussain, S., & Li, W. (2020). *Unprecedented Temporary Reduction in Global Air Pollution Associated with COVID-19 Forced Confinement: A Continental and City Scale Analysis*. In Remote Sensing (Vol. 12, Issue 15). https://doi.org/10.3390/rs12152420

Zhao, B., Mao, K., Cai, Y., Shi, J., Li, Z., Qin, Z., & Meng, X. (2019). A combined Terra and Aqua MODIS land surface temperature and meteorological station data product for China from 2003–2017. *Earth System Science Data*, *12*(4), 2555-2577. https://doi.org/10.5194/essd-2019-155

Zhao, L., Yang, Z.-L., & Hoar, T. J. (2016). Global Soil Moisture Estimation by Assimilating AMSR-E Brightness Temperatures in a Coupled CLM4–RTM–DART System. *Journal of Hydrometeorology*, *17*(9), 2431–2454. https://doi.org/10.1175/JHM-D-15-0218.1

Zhao, S., Qin, Q., Yang, Y., Xiong, Y., & Qiu, G. (2009). Comparison of two split-window methods for retrieving land surface temperature from MODIS data. *Journal of Earth System Science*, *118*(4), 345. https://doi.org/10.1007/s12040-009-0027-4

Zheng, X., Zhu, J., & Yan, Q. (2013). Monthly air temperatures over northern China estimated by integrating MODIS data with GIS techniques. *Journal of Applied Meteorology and Climatology*, *52*(9), 1987–2000. https://doi.org/10.1175/JAMC-D-12-0264.1

Zhou, B., Rybski, D., & Kropp, J. P. (2017a). The role of city size and urban form in the surface urban heat island. *Scientific Reports*, *7*(1), 1–9. https://doi.org/10.1038/s41598-017-04242-2

Zhou, D., Bonafoni, S., Zhang, L., & Wang, R. (2018). Remote sensing of the urban heat island effect in a highly populated urban agglomeration area in East China. *Science of the Total Environment*, *628–629*(219), 415–429. https://doi.org/10.1016/j.scitotenv.2018.02.074

Zhou, D., Xiao, J., Bonafoni, S., Berger, C., Deilami, K., Zhou, Y., Frolking, S., Yao, R., Qiao, Z., & Sobrino, J. A. (2019). Satellite remote sensing of surface urban heat islands: Progress, challenges, and perspectives. *Remote Sensing*, *11*(1), 48. https://doi.org/10.3390/rs11010048

Zhou, D., Zhang, L., Hao, L., Sun, G., Liu, Y., & Zhu, C. (2016a). Spatiotemporal trends of urban heat island effect along the urban development intensity gradient in China. *Science of the Total Environment*, *544*(219), 617–626. https://doi.org/10.1016/j.scitotenv.2015.11.168

Zhou, D., Zhang, L., Li, D., Huang, D., & Zhu, C. (2016b). Climate-vegetation control on the diurnal and seasonal variations of surface urban heat islands in China. *Environmental Research Letters*, *11*(7), 074009. https://doi.org/10.1088/1748-9326/11/7/074009

Zhou, D., Zhao, S., Liu, S., Zhang, L., & Zhu, C. (2014). Surface urban heat island in China's 32 major cities: Spatial patterns and drivers. *Remote Sensing of Environment*, *152*, 51–61. https://doi.org/10.1016/j.rse.2014.05.017

Zhou, D., Zhao, S., Zhang, L., Sun, G., & Liu, Y. (2015). The footprint of urban heat island effect in China. *Scientific Reports*, *5*(1), 1-11. https://doi.org/10.1038/srep11160

Zhou, J., Zhou, J., Chen, Y., Wang, J., Zhan, W., & Wang, J. (2011). Maximum Nighttime Urban Heat Island (UHI) Intensity Simulation by Integrating Remotely Sensed Data and Meteorological Observations. *IEEE Journal of Selected Topics in Applied Earth Observations and Remote Sensing*, *4*(1), 138–146. https://doi.org/10.1109/JSTARS.2010.2070871

Zhou, W., Peng, B., Shi, J., Wang, T., Dhital, Y. P., Yao, R., Yu, Y., Lei, Z., & Zhao, R. (2017b). Estimating high resolution daily air temperature based on remote sensing products and climate reanalysis datasets over glacierized basins: A case study in the Langtang Valley, Nepal. *Remote Sensing*, *9*(9), 959. https://doi.org/10.3390/rs9090959

Zhu, L., Huang, Q., Ren, Q., Yue, H., Jiao, C., & He, C. (2020a). Identifying urban haze islands and extracting their spatial features. *Ecological Indicators*, *115*, 106385. https://doi.org/10.1016/j.ecolind.2020.106385

Zhu, W., Lu, A., & Jia, S. (2013). Estimation of daily maximum and minimum air temperature using MODIS land surface temperature products. *Remote Sensing of Environment*, *130*, 62–73. https://doi.org/10.1016/j.rse.2012.10.034

Zhu, Y., Xie, J., Huang, F., & Cao, L. (2020b). Association between short-term exposure to air pollution and COVID-19 infection: Evidence from China. *Science of The Total Environment*, *727*, 138704. https://doi.org/https://doi.org/10.1016/j.scitotenv.2020.138704

List of Publications

Journal Publications

Alqasemi, A., Hereher, M., Al-Quraishi, A., Saibi, H., Aldahan, A., & Abuelgasim, A. (2020). Retrieval of monthly maximum and minimum air temperature using MODIS Aqua land surface temperature data over the United Arab Emirates (UAE). *Geocarto International*. https://doi.org/10.1080/10106049.2020.1837261 (Published)

Research Papers Presented at Conferences

Alqasemi, A. S. F., Saibi, H., Abuelgasim, A., & Aldahan, A. (2020). Thermal structure anomalies in eastern Abu Dhabi from remote sensing and geophysics. In Fifth International Conference on Engineering Geophysics, Al Ain, UAE, 21–24 October 2019 (pp. 147–150). https://doi.org/10.1190/iceg2019-038.1 (Published)

Alqasemi, A., Hereher, M., Kaplan, G., Al-Quraishi, A., Saibi, H.(2020). Impact of COVID-19 lockdown upon the air quality and surface urban heat island over the United Arab Emirates. *Science of the Total Environment*. https://authors.elsevier.com/tracking/article/details.do?aid=144330&jid=STOTEN&surname=Alqasemi (Accepted)